Doctoral Thesis

Chemical and Electrochemical Stability of Tailored Electrolyte Systems for High-energy Density Lithium-ion Batteries

Koeun Kim

Department of Energy Engineering
(Battery Science and Technology)

Graduate School of UNIST

2020

Chemical and Electrochemical Stability of Tailored Electrolyte Systems for High-energy Density Lithium-ion Batteries

Koeun Kim

Department of Energy Engineering
(Battery Science and Technology)

Graduate School of UNIST

Chemical and Electrochemical Stability of Tailored Electrolyte Systems for High-energy Density Lithium-ion Batteries

A thesis/dissertation
submitted to the Graduate School of UNIST
in partial fulfillment of the
requirements for the degree of
Doctor of Philosophy of Science

Koeun Kim

12/10/2019
Approved by

_____

Advisor
Nam-Soon Choi

Chemical and Electrochemical Stability of Tailored Electrolyte Systems for High-energy Density Lithium-ion Batteries

Koeun Kim

This certifies that the thesis/dissertation of Koeun Kim is approved.

12/10/2019

signature

_____

Advisor: Nam-Soon Choi

signature

_____

Kyeong-Min Jeong

signature

_____

Hyun-Kon Song

signature

_____

Sung You Hong

signature

_____

Seok Ju Kang

Abstract

As the requirement of the green generation advances beyond eco-friendly, Li-ion batteries (LIBs) are becoming more important as sustainable energy storage devices for electric vehicles and energy storage systems because of their potential to achieve high energy densities and long lifespans. Ni-rich layered oxides ($LiNi_xCo_yMn_zO_2$, $x > 0.6$) have been considered one of the promising cathode materials due to its high reversible capacity ~200mAh g^{-1}. However, Ni-rich cathode manifests its structural degradation, low thermal stability and parasitic reactions of electrolytes with Ni^{4+} which induces the oxidative decomposition of electrolyte due to its high reactivity. Silicon (Si) is the most exciting anode material because of the high theoretical capacity of 3579 mAh g^{-1} for $Li_{15}Si_4$ surpassing that of the carbonaceous anodes (372 mAh g^{-1} for LiC_6). However, severe volume changes and vulnerable interfaces of silicon during cycling impede its practical uses because the newly exposed active surface of silicon to electrolyte induces perpetual electrolyte decomposition. Thus, the electrolyte-electrode interface should be controlled by constructing interfacial layers on both electrodes for stabilizing highly reactive electrodes. In addition, the degradation mechanism of conventional electrolytes composed of lithium hexafluorophosphate ($LiPF_6$) and carbonate solvent mixture receives attention for ensuring the best performance of high-energy-density LIBs. Ion-paired $LiPF_6$ is prone to decompose into LiF and PF_5, strong Lewis acids, and promotes the further hydrolysis of $LiPF_6$ reacting with a trace of water in batteries producing reactive species such as HF. HF can destroy the electrolyte-electrode interfacial layer, leach the transition metal dissolution from cathodes and leads to a decomposition of the solvent. Therefore, the scavenging highly reactive species in electrolytes should be significantly considered in developing the electrolyte systems.

Herein, the underlying mechanisms of electrolytes and electrolyte-electrode interface will be clearly enlightened through electrochemical method and characterizations; (i) analyzing change of physical and chemical structures of electrolyte using nuclear magnetic resonance (NMR) spectroscopy and electrospray-ionization mass spectrometry (ESI-MS) (ii) investigating chemical structure and morphologies of the electrode-electrolyte interface using time-of-flight secondary ion mass spectrometry (TOF-SIMS), X-ray photoelectron spectroscopy (XPS) and field-emission scanning electron microscopy (FE-SEM) and (iii) analyzing structural changes of electrodes using high-resolution transmission electron microscopy (HR-TEM), scanning transmission electron microscopy (STEM) and X-ray diffraction (XRD) spectroscopy. Understanding of electrolyte-electrode degradation mechanism through systematic analysis of electrolyte-electrode interface will contribute to the development of chemically and electrochemically stable electrolyte systems for high-performance LIBs.

Contents

List of Figures

(k) graphite and (l) Si alloy with FEC-based electrolyte.

Figure 2.8 SEM images of Si-C anodes retrieved from LCO-NCM/Si-C full cells with (a) EC-based electrolyte and (b) FEC-based electrolyte after storage for 20 days at 45 °C. EDS patterns were obtained at the selected zone of the Si alloy particles.

Figure 2.9 ICP-MS results showing the amounts of the transition metal (Co, Mn, Ni) in Si-C anodes retrieved from LCO-NCM/Si-C full cells after storage for 20 days at 45 °C.

Figure 2.10 Photographs of the solvent mixtures: (a) FEC, (c) FEC/DEC (3/7, w/w), and (e) DEC without salt, and (b) FEC, (d) FEC/DEC (3/7, w/w), and (f) DEC with 1.5 M $LiPF_6$ salt before and after storage for 3 days at 60 °C. (g) Indicator chart for the pH scale.

Figure 2.11 Photographs of 1.5 M $LiPF_6$ in EC (a) before and (b) after storage for 3 days at 60 °C. Photographs of 1.5 M $LiPF_6$, 1.5 M lithium bis(trifluoromethane)sulfonimide ($LiN(SO_2CF_3)_2$) and 0.5 M lithium trifluoromethane sulfonate ($LiSO_3CF_3$) salt dissolved in FEC (c) before and (d) after storage for 3 days at 60 °C. Indicator chart for the pH scale is presented in Figure 2.10g.

Figure 2.12 (a) Photographs of 0.06 M tris(pentafluorophenyl)borane (TPFPB) in FEC stored at room temperature. (b) ^{13}C NMR spectrum of 0.06 M TPFPB in FEC after 24 h at room temperature. (c) Schematic diagram of the interaction between FEC and TPFPB.

Figure 3.1 (a) Charge-discharge curves and (b) dQ/dV plots of NCM/graphite full cells with baseline, 1% ETFB-containing, and 1% VC-containing electrolytes measured at a C/10 rate and 25 °C during precycling. (c) Chemical structures and HOMO-LUMO energy values of carbonate solvents (EC, EMC, and DEC) and additives (ETFB and VC). (d) dQ/dV plots of NCM/graphite full cells with EC-free electrolytes (EMC/DEC/1.15 M $LiPF_6$ with and without 1% ETFB) measured at C/10 rate and 25 °C during precycling. d-ETFB denotes byproducts generated by ETFB reduction.

Figure 3.2 Discharge capacity and Coulombic efficiency of NCM/graphite full cells during 300 cycles at a C/2 rate and (a) 25 °C or (b) 45 °C. Nyquist plots of NCM/graphite full cells after 300 cycles at (c) 25 °C and (d) 45 °C. The inset shows an enlargement of the (c) plot.

Figure 3.3 (a) Potentiostatic profiles of Li/NCM half cells with baseline and 1% ETFB-containing electrolytes measured at a constant voltage of 4.4 V vs. Li/Li^+ for 2 h. (b) ICP results showing the amounts of transition metals (Ni, Co, and Mn) dissolved from fully delithiated NCM cathodes covered by a baseline or ETFB electrolyte-derived interfacial layer after storage at 60 °C for 5 days.

Figure 3.4 (a) Li_2CO_3 and LiOH contents of NCM and $LiCoO_2$ cathode powders. (b) Possible formation mechanisms of HF and NiF_2 triggered by the reaction of LiOH with PF_5 generated by $LiPF_6$ decomposition. ^{19}F NMR spectra (564 MHz, deuterated solvent, THF-D_8) of baseline electrolyte without (c) and (e) and with (d) and (f) 1% LiOH, before and after storage at 60 °C for 3 days. (g) Hydrolysis reactions of $LiPF_6$ promoted by LiOH.

Figure 3.5 Cross-sectional SEM images of NCM cathodes retrieved from NCM/graphite full cells with (a) baseline and (b) 1% ETFB-containing electrolytes after 300 cycles at 25 °C, and (c) baseline

Figure 4.6 Concentrations of decomposition products in $LiPF_6$-based electrolytes obtained from kinetic ^{19}F NMR measurements of baseline, 0.5% ON, and 0.5% TMS-ON electrolytes after 40 h at 45 °C: (a) POF_3, (b) $PO_2F_2^-$, (c) HF and (d) TMSF. F 1s XPS spectra of graphite anodes retrieved from NCM/graphite full cells with (e) baseline and (f) 0.5% TMS-ON electrolytes after 3 cycles at 25℃ (charge and discharge rate: 0.2C). (g) Schematic illustration of the reaction mechanism of TMS-ON in the bulk electrolyte and the modified SEI structure induced at the graphite anode by TMS-ON.

Figure 4.7 ICP-OES results for electrolytes retrieved from NCM/graphite full cells after aging (at 45 °C for 1 h and at 25 °C for 20 h).

Figure 4.8 (a) HOMO and LUMO energy levels of EC, DEC, EMC, VC, TMS-ON, ON, and TMSF interacting with a Li^+ ion. Electrochemical performance of NCM/graphite full cells: Cycle performance of NCM/graphite full cells with baseline and 0.5% TMS-ON electrolytes at (b) 25℃ and (c) 45℃ (charge and discharge rate: 0.5C) and voltage profiles of NCM/graphite full cells with (d) baseline and (e) 0.5% TMS-ON electrolyte at 45 °C for the 10^{th}, 100^{th}, 200^{th}, 300^{th}, and 400^{th} cycles. (f) Nyquist plots of NCM/graphite full cells after 400 cycles at 45℃.

Figure 4.9 ^1H NMR spectra of baseline and 0.5% TMS-ON electrolytes retrieved from NCM/graphite full cells (a) before precycling (after aging at 45 °C for 1 h and 25 °C for 20 h) and (b) after 400 cycles at 45℃.

Figure 4.10 XPS spectra of NCM cathodes retrieved from NCM/graphite full cells with baseline and 0.5% TMS-ON electrolytes after 3 cycles at 25 °C (charge and discharge rates: 0.2C): C 1s spectra of NCM cathodes with (a) baseline and (b) 0.5% TMS-ON electrolytes; F 1s spectra of NCM cathodes with (c) baseline and (d) 0.5% TMS-ON electrolyte; and (e) N 1s spectra of NCM cathodes with baseline and 0.5% TMS-ON electrolytes. (f) Transition-metal dissolution from a delithiated NCM cathode with a VC- or ON-derived CEI following storage in the baseline electrolyte at 45 °C for 7 days. (g) Possible oxidative radical polymerization mechanisms of VC and ON initiated by the radical cation produced by oxidation of VC.

Figure 4.11 TOF-SIMS analysis of NCM cathodes retrieved from NCM/graphite full cells with baseline and 0.5% TMS-ON electrolytes after 400 cycles at 45 °C (charge and discharge rates: 0.5C). (a) TOF-SIMS spectra for CN^-, $^7LiF_2^-$, PO_2^-, and PO_3^- integrated over 300 s. 3D visualization and depth profiles of the CEIs on the NCM cathodes cycled with (b) and (d) the baseline electrolyte and (c) and (e) the 0.5% TMS-ON electrolyte with Cs^+ sputtering.

Figure 4.12 F 1s XPS spectra of graphite anodes retrieved from NCM/graphite full cells with baseline and 0.5% TMS-ON-containing electrolytes after 400 cycles at 45 °C (charge and discharge rates: 0.5C).

Figure 4.13. Microstructure and nanostructure of the NCM cathodes retrieved from NCM/graphite full cells after 400 cycles at 45 °C (charge and discharge rates: 0.5C). TEM and FFT images of NCM cathodes cycled with (a) baseline and (b) 0.5% TMS-ON electrolytes. Magnified STEM images of the

surfaces of NCM cathodes cycled with (c) baseline and (d) 0.5% TMS-ON electrolytes. Series of EELS spectra for the O K-edge from the surface to the inner bulk of NCM particles cycled with (e) baseline and (f) 0.5% TMS-ON electrolytes (every 1 nm). Cross-sectional SEM images of NCM cathodes cycled with (g) and (h) baseline and (i) and (j) 0.5% TMS-ON electrolytes.

Figure 4.14 Series of EELS spectra for the NCM cathodes retrieved from NCM/graphite full cells after 400 cycles at 45 °C (charge and discharge rates: 0.5C). Ni L-edge spectra from the surface to the inner bulk of NCM particles cycled with (a) baseline and (b) 0.5% TMS-ON-containing electrolytes (every 1 nm).

Figure 4.15 EDS mapping of an NCM cathode retrieved from an NCM/graphite full cell cycled with the (a) baseline electrolyte and (b) 0.5% TMS-ON electrolyte for 400 cycles at 45 °C (charge and discharge rates: 0.5C).

List of Tables

I. Introduction

1.1 Lithium-ion batteries

Lithium-ion batteries (LIBs) are perceived as suitable power sources for a variety of mobile electronic devices and a solution to the demand for ecofriendly electric vehicles (EVs) and large-scale energy storage systems (ESSs) because of their high energy density and long cycle life.[1-5] However, the growing demand for large-scale rechargeable batteries requires the development of electrode materials with high energy-storage capabilities, exceeding those of conventional graphite and $LiCoO_2$, and good safety characteristic. To improve the energy density of LIBs, electrode materials with high reversible capacities: cathode materials that operate at high voltages and anode materials with low working potentials close to 0 V vs. Li/Li^+ have been developed. Therefore, the Ni-rich cathode and Si-containing anode are regarded as promising electrodes capable of realizing high-energy-density LIBs as showed in Figure 1.1.

The Ni-rich cathodes ($LiNi_xCo_yMn_zO_2$, x+y+z=1, x>0.6) have attracted attention due to its high capacity (> 180mAh g^{-1}), high operating voltages (~3.8 V) and low cost.[6-8] However, the Ni-rich cathodes still have some critical issues interrupting their practical uses[9-10] such as (i) residual lithium compounds, (ii) mechanical cracking, (iii) superoxide radical ($O_2^{\bullet-}$) and gas evolution and (iv) cation mixing and electrolyte decomposition (Figure 1.2).

(i) Residual lithium compounds

The higher the content of Ni in the Ni-rich cathodes, the higher the portion of Ni^{3+} which undergoes self-reduced to Ni^{2+} due to the instability of Ni trivalent state. Ni^{2+} ions is prone to occupy the Li^+ ion sites due to the radius of Ni^{2+} (0.69 Å) is close to that of Li^+ (0.72 Å). This result prevents Li^+ ions from diffusing into the Ni-rich cathodes, leaving them on the surface.[11-12] These residual Li^+ ions can easily react with H_2O, CO_2 and O_2 to form a LiOH, Li_2CO_3 and Li_2O, which are called residual lithium compounds.[13-14] These compounds may cause undesirable side reactions which promote the decomposition of $LiPF_6$-based electrolyte.

(ii) Mechanical cracking

The active material of Ni-rich cathode has a structure in which nano-sized primary particles are aggregated in different directions to form micro-sized secondary particles in a spherical shape. These polycrystalline structured Ni-rich particles undergo repeated anisotropic expansion and contraction during charge and discharge process, which diminishes the mechanical integrity between Ni-rich particles and finally induces the intergranular cracking in primary particle.[15-16]

(iii) Superoxide radical ($O_2^{\bullet-}$) and gas evolution

Reactive oxygen species and oxygen gas are released from Ni-rich cathode to maintain charge neutrality resulting from reduction of oxidation index of transition metals.[17-19] Superoxide radicals ($O_2^{\cdot-}$) may be formed at the cathode surface and it can attack the methylene species (CH_2) of ethylene

carbonate (EC) via a SN_2 pathway producing unwanted products such as CO_2, CO and H_2O.[20]

(iv) Electrolyte decomposition and cation mixing

The highly reactive Ni^{4+} is formed on the surface of the Ni-rich cathodes in the charged state and may induce unwanted oxidative decomposition of electrolyte. As oxidative decomposition of the electrolyte is induced, the Ni^{4+} at the surface of Ni-rich cathodes is reduced to Ni^{3+} and Ni^{2+}, and generated Ni^{2+} ions, which has similar size with Li^+ ions, aggravate the cation mixing at the surface Ni-rich cathodes. Cation mixing deteriorates the electrochemical performance of Ni-rich cathodes by converting an electrochemically active layered structure into an electrochemically inactive rock-salt structure.

Silicon (Si) has been spotlighted as a high- capacity anode materials because Si has high theoretical capacity of 3579 mAh g^{-1} for $Li_{15}Si_4$ compared to pure graphite, which has theoretical capacity of 360 mAh g^{-1}.[21-22] However, the main obstacle to the application of pure Si as an anode materials is a significant volume change during the charge and discharge process. Severe volume change in Si particle induces pulverization of Si particles and exposes active Si surface to electrolyte. It causes a continuous decomposition of electrolyte, generating thick and unstable solid electrolyte interface (SEI) at Si surface, which leads to depletion of electrolyte in the LIBs, increase of battery resistance and deterioration of the electrochemical performance of batteries.[23-24]

The abovementioned problems can be relieved by stabilization of electrolyte-electrode interface at both electrodes, which guarantees the realization of high-performance batteries, therefore, the suitable electrolyte systems should be developed reducing unwanted side reaction between electrode and electrolyte interface and improving the chemical stability and electrochemical performance of high-energy density LIBs.

	GEN2 (2016~) >300km	GEN3 (2021~) ~500km	GEN3.5 (2025~) >500km
Cell energy density	450~550Wh/L (200~250Wh/kg)	650~750Wh/L (250~300Wh/kg)	>750Wh/L (300Wh/kg)
Cathode	NCM622 (170~175mAh/g)	High Ni NCM, NCA (200~210mAh/g) (Ni 80~88%, Co 5~10%)	High Ni NCM, NCA (215~220mAh/g) (Ni > 90%, Co <5%)
Anode	Graphite (350~360mAh/g)	Graphite + Si (400~450mAh/g)	Graphite + Si (> 500mAh/g)
Separator	Ceramic coated separator		
electrolyte	High performance: long cycle life, high power, low&high temperature performance, stability Safety: Non-flammable electrolyte, gel polymer or solid electrolyte		

SNE reasearch, LG chem, IBK Securities

Figure 1.1 Development trend of a next generation of LIBs for high energy density.

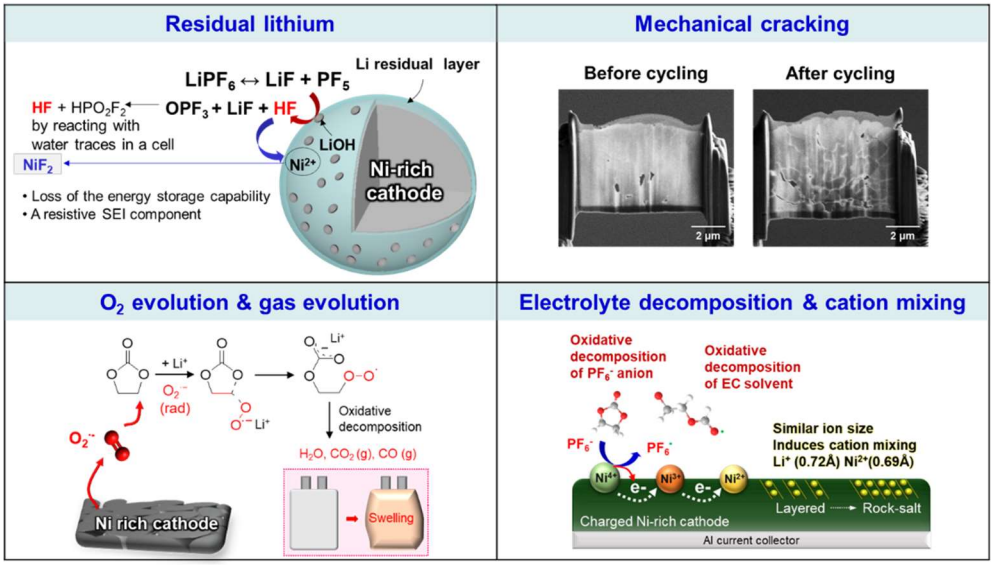

Figure 1.2 Critical issues of Ni-rich cathode: residual lithium, mechanical cracking, gas evolution, electrolyte decomposition and cation mixing.

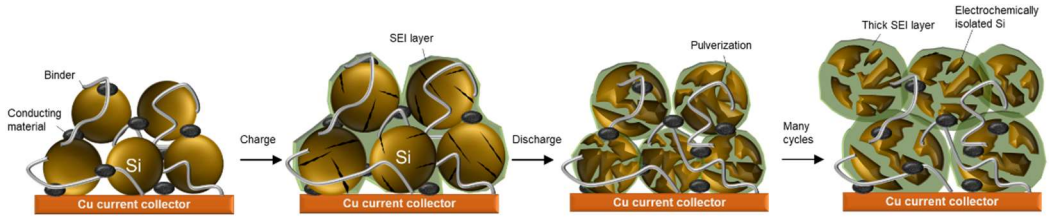

Figure 1.3 Degradation mechanism of Si-containing anode during cycling.

1.2 $LiPF_6$-based electrolytes

Lithium hexafluorophosphate ($LiPF_6$)-based electrolytes, commonly used in conventional LIBs, exhibits high ionic conductivity (> 5 mS cm^{-1}), reasonably good oxidation stability up to 4.35V vs. Li/Li^+ and compatibility toward Al current collectors.[25-27] Low concentration of $LiPF_6$ can be completely dissociated into solvated Li^+ and PF_6^- in solvents, however, the conventional electrolyte for LIBs is composed of more than 1M $LiPF_6$ and a carbonate-based solvents. Relatively high $LiPF_6$ concentration generates ion-paired $LiPF_6$ through re-association of PF_6^- and Li^+ due to the depending on the solvating power of the solvents toward Li^+.[28-30] The ion-paired $LiPF_6$ is responsible for the negative characteristics of $LiPF_6$ salt such as low thermal stability and high sensitivity toward a trace of water, producing uncontrollable reactive compounds such as Brønsted acidic HF and Lewis acid phosphorus pentafluoride (PF_5).[31-33] The ion-paired $LiPF_6$ undergoes auto-catalytic decomposition accelerated at high temperature. (Equation 1.1)

$$LiPF_6\,(s) \rightarrow LiF\,(s) + PF_5\,(g) \quad (1.1)$$

Small-sized Li^+ ion favorably associating with PF_6^- anion is prone to form LiF and PF_5 due to its larger the ratio of charge-to-radius compared to other alkali metal ions (M^+) such as Na^+, K^+, Rb^+ and Cs^+. Wang et al. reported that the Li^+-F^- bond length (1.8913 Å) is the shortest among the M^+-PF_6^- ion pair via computational method using density functional theory (B3LYP/6-311G(2df)).[34] Morover, the hydrolysis reaction of $LiPF_6$ is a critical issue threatening high-performance of LIBs. Figure 1.4a exhibits that hydrolysis reaction of ion-paired $LiPF_6$ accompanying the HF and various phosphoric acid derivatives such as $H(PO_2F_2)$, $H_2(PO_3F)$, and $H_3(PO_4)$.

Generation of acid compounds in $LiPF_6$ induces the decomposition of electrolyte solvent, the destruction of interfacial layers on electrodes and transition metal (TM) dissolution from the cathode as showed in Figure 1.4b.[35-39] Notably, the physical and chemical stability of SEI that should fulfill the protection of electrodes upon repeated cycling in harsh conditions such as high voltages and elevated temperatures. However, HF damages and changes the SEI structures as below.[40-41] (Equation 1.2-6)

$$Li_2CO_3\,(s) + 2HF\,(g) \rightarrow 2LiF\,(s) + H_2O\,(l) + CO_2\,(g) \quad (1.2)$$

$$LiOH\,(s) + HF\,(g) \rightarrow LiF\,(s) + H_2O\,(l) \quad (1.3)$$

$$Li_2O\,(s) + 2HF\,(g) \rightarrow 2LiF\,(s) + H_2O\,(l) \quad (1.4)$$

$$LiOR\,(s) + HF\,(g) \rightarrow LiF\,(s) + ROH\,(l) \quad (1.5)$$

$$LiOCO_2R\,(s) + HF\,(g) \rightarrow LiF\,(s) + ROH\,(l) + CO_2\,(g) \quad (1.6)$$

In addition, the high acidity due to HF generation in $LiPF_6$-based electrolyte leaches the TM ions from cathode materials. TM dissolution may cause the capacity decay and power fading of LIBs with deterioration of cathode structure as well as the instability of anode interface as cycle progresses.[42-43]These problematic behaviors of acids produced by $LiPF_6$ imperil the long-term cycling and storage

performance of LIBs and the above issues can be mitigated by the use of additives that scavenge acidic species such as HF or inhibit the hydrolysis of $LiPF_6$.

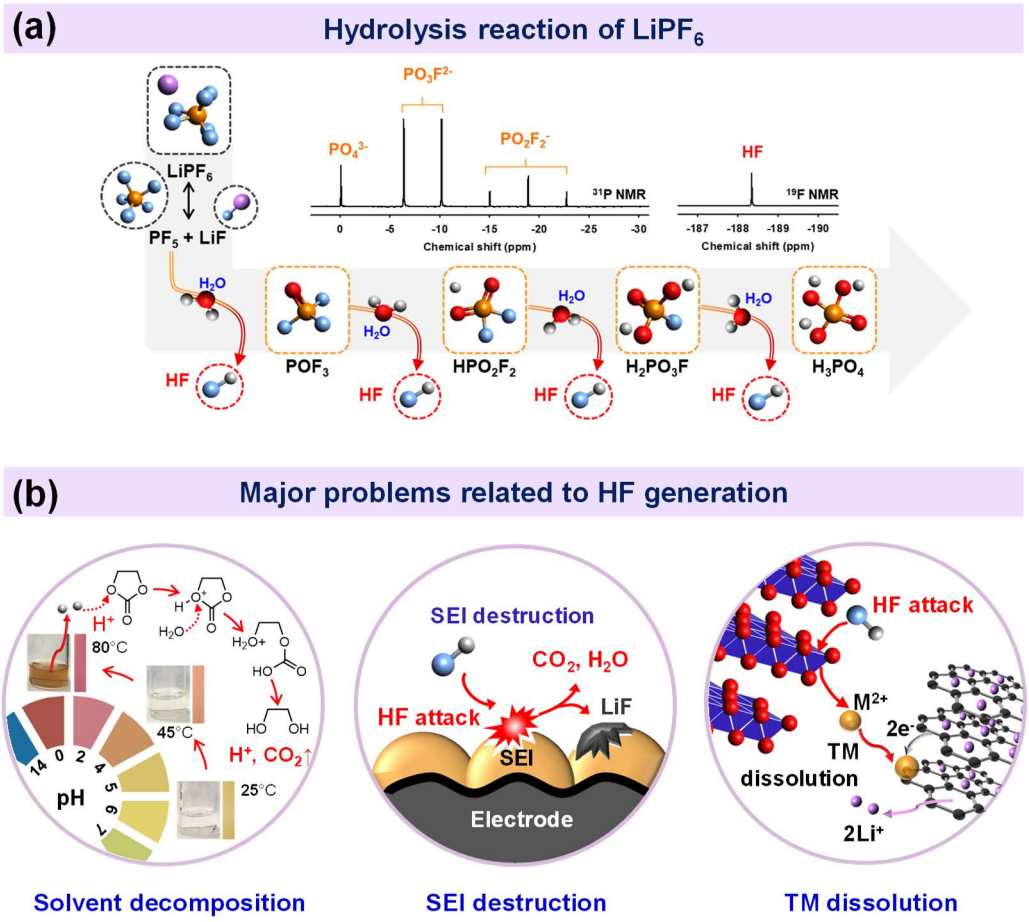

Figure 1.4 (a) Hydrolysis reaction of $LiPF_6$ producing HF and phosphoric acids. (b) Schematic illustration for major problems related to HF generation: solvent decomposition, SEI destruction, and transition metal dissolution.

1.3 Functional electrolyte systems

Many researchers have perceived that generating a protective film at both electrodes is effective strategy to stabilize the electrolyte-electrode interface.[44-46] In-situ formation of SEI by adopting adequate additives can expand the electrochemical stability window of the conventional electrolyte, thus the additional electrolyte decomposition is suppressed at both electrodes. (Figure 1.5) The possibility of SEI forming additive can be predictable by comparing molecular orbital energy levels such as the highest occupied molecular orbital (HOMO) and the lowest occupied molecular orbital (LUMO) energy using theoretical calculation because it is ideal that a SEI is preferentially formed by an additive before the electrolyte oxidative or reductive decomposed. Desirable SEI layer is electrochemically and chemically inert, facilitates the Li^+ diffusion and accommodates the volume changes of electrode materials even at high temperatures.

Moreover, the next electrolyte systems should contain the scavenging highly reactive and causative species in $LiPF_6$-based electrolyte, which is a great importance for realization of maximum performance of high-energy-density LIBs.[47-48] Notably, the stabilization of $LiPF_6$-based electrolyte is a key solution to reduce generation of acidic compounds related to decomposition of $LiPF_6$ because the HF threatens the stability of electrolyte, electrode and electrolyte-electrode interfaces. Figure 1.6 represents the three different type of strategies: (i) Anion receptor, (ii) Lewis base and (iii) HF scavenger. Ion-paired $LiPF_6$ in the electrolyte decomposed in to LiF and PF_5. The produced PF_5 causes parasitic reaction such as PF_5-promoted solvent decomposition and the generation of HF as key species undesired side reactions. To prevent the formation of PF_5 in the electrolyte, complete dissociation of $LiPF_6$ salt is required. Anion receptor with electron deficient atom can contribute to the salt dissociation through the favorable complexation with PF_6^- anion and block the route the formation of PF_5 ($LiPF_6 \rightarrow LiF+PF_5$).[49-51] Lewis base additives with P, O, and N atoms bearing lone pair electrons capture Lewis acid PF_5 by Lewis acid-based interaction and prohibit the hydrolysis of PF_5 producing HF and phosphoric acids.[52-54] In addition, the Brønsted acid HF scavenging mechanism in the electrolytes mainly comes from favorable complexation with additives which have base sites possessing electron donation ability. Representative functional moieties scavenging HF include nitrogen and phosphite core, amino-silane (N-Si) and silyl ether.[55-60]

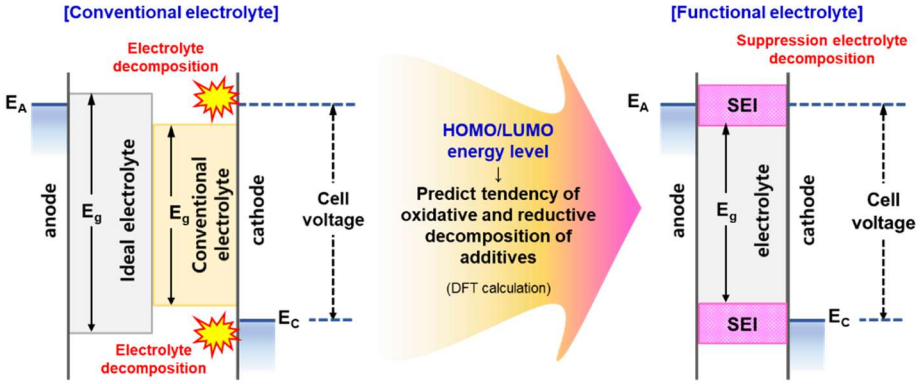

Figure 1.5 Comparing electrochemical stability of conventional electrolyte and functional electrolyte with sacrificial film forming additive.

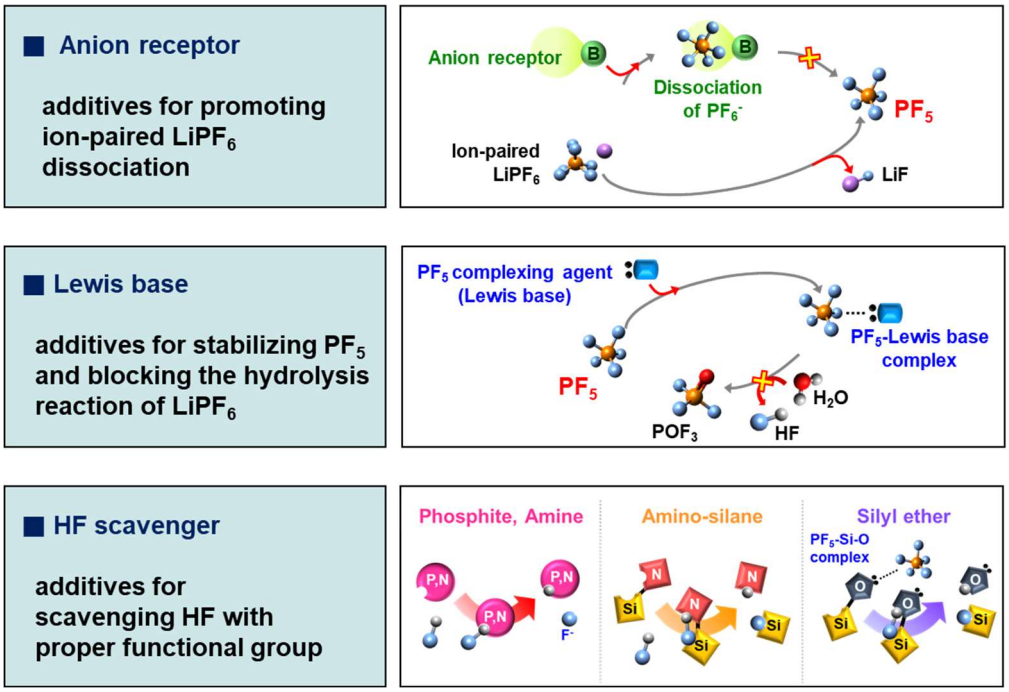

Figure 1.6 Strategies for stabilizing $LiPF_6$-based electrolyte with functional additives: Anion receptor, Lewis base and HF scavenger.

II. Understanding the thermal instability of fluoroethylene carbonate in $LiPF_6$-based electrolytes for lithium ion batteries

2.1 Introduction

Deterioration of the electrode–electrolyte interfaces causes unsatisfactory cycling performance of batteries. To stabilize the electrode–electrolyte interface, various approaches, such as surface-coating of the electrode materials and the use of electrolyte additives, have been proposed. Using reducible and oxidizable compounds for the formation of an artificial solid electrolyte interphase (SEI) is one of the most effective strategies to improve the interfacial stability of electrodes.[61] Si is considered a promising anode material for next-generation LIBs because of its high theoretical capacity of 4212 mAh g^{-1} for $Li_{22}Si_5$.[62] Si anode materials cannot maintain their original structure because of the colossal volume changes that occur during cycling. Such large volume changes cause cracking of the Si particles to generate new active surface sites that may result in further irreversible electrolyte decomposition. Perpetual electrolyte decomposition at the Si anode depletes the electrolyte and degrades the anode. To improve the electrochemical performances of Si anodes, fluoroethylene carbonate (FEC) has been used as a highly effective reducible additive. It has been reported that FEC as an additive effectively modifies the nature of the SEI layer on the anode and improves the electrochemical performances of anodes such as graphite [63-65] and Si.[66-73] Previously, our group reported that Si thin-film/Li half cells with 3 wt.% FEC featured a substantially higher discharge capacity retention (88.5% after 80 cycles) than the FEC-free electrolyte (67.9% after 80 cycles).[68] It should be noted that the optimum content of FEC as a promising reducible additive to improve the electrochemical performances of anodes in LIBs is dependent on the anode materials.[66,69] Despite the beneficial effects of FEC on the anodes, the decomposition mechanisms of FEC are still under investigation. FEC can decompose to vinylene carbonate (VC), which could produce the poly(VC) component of the SEI layer, and HF.[63,74,78] In addition to this reaction, polyacetylene and LiF can be produced as the SEI components by the electrochemical reduction of FEC on a Si electrode.[70] FEC can also be electrochemically reduced at the anode via opening of the five-membered ring leading to the formation of lithium poly(vinyl carbonate) ($(CH_2\text{-}CHOCO_2Li)_n$), LiF, and partially fluorinated dimers.[72] Gustafsson et al. demonstrated that the two most likely decomposition routes for FEC are defluorination and ring opening to form LiF and other organic species such as -$CHF\text{-}OCO_2$-type compounds.[67] However, there have been reports of detrimental effects of the FEC-derived SEI on the electrochemical properties of Li/graphite half cells and spinel-type $Li_{1.1}Mn_{1.9}O_4$/graphite full cells.[75-76] The capacity loss of the FEC-containing cell during storage at 60 °C was severe compared to those of VC-containing and additive-free cells. Recently, Lu et al. reported that the FEC additive did not prevent capacity fading of $LiMn_2O_4$ (LMO) cathode half cells at elevated temperatures.[77] They

suggested that the HF formed via defluorination of FEC at elevated temperatures leads to increased Mn dissolution and the formation of a thick SEI layer on the LMO cathode.

Herein, we demonstrate the thermal instability of FEC as a co-solvent in high-energy-density lithium-ion batteries based on pitch-coated silicon alloy-graphite (Si-C) anode coupled with $LiCoO_2$ (LCO)-$LiNi_{0.5}Co_{0.2}Mn_{0.3}O_2$ (NCM) cathode delivering high capacity of ~180 mAh g^{-1}. The differences in the surface chemistry of the Si-C anodes cycled in ethylene carbonate (EC)-based and FEC-based electrolyte are examined using ex situ X-ray photoelectron spectroscopy (XPS) measurements. The impact of FEC on the self-discharge of the Si-C anode in a full cell coupled with an LCO-NCM cathode during storage at 45 °C is discussed. Furthermore, we propose possible mechanisms that account for the thermal instability of the FEC solvent in presence of $LiPF_6$, leading to the inferior electrochemical performance of full cells at elevated temperatures.[78]

2.2 Experimental method

Preparation of the electrolyte and electrode

Two liquid electrolytes were tested: 1.5 M Lithium hexafluorophosphate ($LiPF_6$) in EC/diethyl carbonate (DEC) (3/7, w/w, EC-based electrolyte) and 1.5 M $LiPF_6$ in FEC/DEC (3/7, w/w, FEC-based electrolyte). All solvents and the $LiPF_6$ salt (Soulbrain Co., Ltd) were used as received. The water content of electrolytes was determined by Karl Fischer titration (C30, Mettler Toledo). The water content of EC-based electrolyte and FEC-based electrolyte was 12.5 and 10.0 ppm, respectively. To perform *ab initio* calculations of the reductive stability, optimized geometries of FEC and EC were obtained using Gaussian 09. Molecule optimization was carried out by applying density functional theory (DFT) with the B3LYP/6-311+G basic set. The anode was composed of 97 wt.% Si-C as the active material and 2 wt.% styrene-butadiene rubber/1 wt.% sodium carboxymethyl cellulose as the binder. Pitch-coated Si alloy (22.5 wt.%) was blended with 77.5 wt.% graphite to fabricate the Si-C anodes. The specific capacity and active material mass loading of the anode were 3.02 mAh cm^{-2} and 5.60 mg cm^{-2}, respectively. The cathode was composed of 97.8 wt.% LCO-NCM as the active material, 1.0 wt.% Super-P as the conducting agent, and 1.2 wt.% poly(vinylene fluoride) as the binder. The blend ratio of LCO and NCM in the cathode was 8/2, w/w. The specific capacity of the LCO-NCM cathode and loading of the active cathode material were 2.47 mAh cm^{-2} and 13.3 mg cm^{-2}, respectively.

Electrochemical measurements

LCO-NCM/Si-C full cells (2032 coin-type) were assembled with a microporous polyethylene film (SK Innovation Co., Ltd.) as a separator in an argon-filled glove box (O_2 and H_2O <0.1 ppm). Its thickness and porosity were 20 μm and 38 %, respectively. LCO-NCM/Si-C full cells were galvanostatically precycled at a constant current of 9.25 mA g^{-1} (corresponding to C/20) between 2.5 and 4.2 V at 30 °C using a computer-controlled battery testing equipment (WonATech WBCS 3000). The constant voltage condition was applied to the end of the charge of precycling until the current was below C/100. Thereafter, the full cells were cycled at a constant current of 37 mA g^{-1} (corresponding to C/5) between 2.5 and 4.2 V at 30 °C for the standard cycle. The constant voltage condition was applied to the end of the charge of the standard cycle until the current was below C/50. After the standard cycle, the full cells were cycled at a constant current of 185 mA g^{-1} (corresponding to 1 C) between 2.5 and 4.2 V at 60 °C. The constant voltage condition was applied to the end of the charge at every cycle until the current was below C/25. To investigate the storage performance at an elevated temperature, the LCO-NCM/Li and Si-C/Li half cells and the LCO-NCM/Si-C full cells were stored for 20 days at 45 °C in a fully charged state, and then their capacity retention was measured at 30 °C. The capacity retention was calculated on the basis of the discharge capacity before storage.

Material characterization

After the 2nd cycle, the cells were carefully opened in a glove box to retrieve the Si-C anodes. The anodes were then rinsed in dimethyl carbonate to remove any residual $LiPF_6$-based electrolyte, and the resulting samples were dried at room temperature. These dried anodes were analyzed using ex situ X-ray photoelectron spectroscopy (XPS, K-Alpha, Thermo Fisher) with Al K_α ($h\nu$ = 1486.6 eV) radiation under ultrahigh vacuum with a 0.10 eV step and 50 eV pass energy. All XPS spectra were calibrated to the C–C bonding energy at 285 eV. To avoid any possible contamination, the samples for the ex situ XPS measurements were prepared in a glove box and sealed in an aluminum pouch under vacuum before use. The surface morphologies of the Si-C anodes were determined by field emission scanning electron microscopy (FE-SEM, Nova NanoSEM, FEI), and energy dispersive spectrometry (EDS) was performed to identify the atomic composition of the surfaces of the Si-C anodes. All Si-C samples were retrieved from LCO-NCM/Si-C full cells that had been stored for 20 days at 45 °C with EC- or FEC-based electrolyte. The SEM and EDS samples were carefully prepared in a glove box to avoid any possible contamination. The samples were sealed in an aluminum pouch under vacuum prior to analysis. To investigate the transition metal dissolution behavior of fully delithiated LCO-NCM cathodes in the EC- and FEC-based electrolytes, cathodes charged up to 4.3 V in the EC-based electrolyte were soaked in FEC solvent. The electrolytes, which were under argon in a polyethylene bottle that was sealed in an aluminum pouch, were stored in a convection oven at 60 °C for 24 h. The amounts of metal ions (i.e., Ni, Co, and Mn) in the electrolytes that had contact with the fully delithiated cathodes at 60 °C were measured via inductively coupled plasma mass spectrometry (ICP-MS, ELAN DRC-II, Perkin Elmer). The amounts of metal ions deposited on the Si-C anodes retrieved from LCO-NCM/Si-C full cells that had been stored for 20 days at 45 °C were determined by means of ICP-MS. To examine the thermal stability of FEC at an elevated temperature, typical experiments were performed. Solvent mixtures of FEC and DEC at 10:0, 3:7, and 0:10 weight ratios with and without 1.5 M $LiPF_6$ were prepared under argon in polyethylene bottles that were sealed in aluminum pouches; these mixtures were then stored in a convection oven for three days at 60 °C. To elucidate the effect of the $LiPF_6$ salt on the thermal stability of FEC, the characteristics of FEC with 1.5 M lithium bis(trifluoromethane)sulfonimide ($LiN(SO_2CF_3)_2$, 99.95% Aldrich) or 0.5 M lithium trifluoromethane sulfonate ($LiSO_3CF_3$, 99.995% Aldrich) were compared with those of FEC with 1.5 M $LiPF_6$ before and after storage for three days at 60 °C. $LiSO_3CF_3$ (0.5 M) was dissolved in FEC because of its limited solubility. The chemical stability of FEC was investigated in the presence of 0.06 M tris(pentafluorophenyl) borane (TPFPB, 97% Tokyo Chemical Industry Co., Ltd.), which can act as a Lewis acid. FEC with 0.06 M TPFPB was stored for 24 h at room temperature. The color changes and acidities of the samples before and after storage were monitored by photographs and pH paper (Toyo Roshi Kaisha, Ltd), respectively. The samples were analyzed using ^{13}C nuclear magnetic

resonance (NMR) spectroscopy (600 MHz-VNMRS 600, Agilent) to identify the changes in the molecular structures of the electrolytes before and after storage. All samples were prepared in the THF-d_8 solvent with a 1:1 volume ratio.

2.3 Results and discussion

Figure 2.1a shows the voltage profiles of the $LiCoO_2$ (LCO)-$LiNi_{0.5}Co_{0.2}Mn_{0.3}O_2$ (NCM) cathode coupled with a pitch-coated silicon alloy-graphite (Si-C) anode during the precycle. To realize high-energy-density lithium-ion batteries, LCO with limited capacity was blended with NCM having the advantage of high capacity. A full cell with FEC/DEC (3/7, w/w)/1.5 M $LiPF_6$ (FEC-based electrolyte) exhibited a higher charge plateau and lower discharge plateau than a full cell with EC/DEC (3/7, w/w)/1.5 M $LiPF_6$ (EC-based electrolyte); this indicates voltage loss caused by internal cell resistance and polarization. This voltage loss in the FEC-based electrolyte reduced the initial Coulombic efficiency (ICE) of the full cells from 83.8 % to 81.9 %. In addition, the FEC-based electrolyte delivered slightly reduced discharge capacity of 173.8 mAh g^{-1}, compared to the EC-based electrolyte (179.0 mAh g^{-1}). To elucidate the effect of the FEC-based electrolyte on the ICEs of the full cells, the differential capacity (dQ/dV) was plotted, as presented in Figure 2.1b. Both full cells show two pronounced reduction peaks: A reduction potential, which was induced by EC decomposition, appeared at 3.1 V for the full cell with the EC-based electrolyte, while the FEC-based electrolyte underwent electrochemical reductive decomposition at a relatively low potential of 2.8 V. This discrepancy is caused by a more facile electrochemical reduction of the FEC molecules due to the relatively low lowest unoccupied molecular orbital (LUMO) energy (−0.8531 eV), which results in a higher reduction tendency than in the case of EC (LUMO energy = −0.4014 eV) at the Si-C anode in a full cell.[79-81] Therefore, it is likely that FEC modifies the interfacial structure of the anode, and the voltage loss of the full cells can be ascribed to the FEC-derived SEI layer.

Figure 2.1c and d show the discharge capacity retentions and Coulombic efficiencies, respectively, of LCO-NCM/Si-C full cells with EC- and FEC-based electrolytes at a rate of 1 C and 60 °C. Similar Coulombic efficiencies of greater than 98.6% were observed for both electrolytes over 50 cycles. However, full cells with the FEC-based electrolyte showed a slightly lower discharge capacity retention of 80.8% than those with the EC-based electrolyte (84.4%) at the 50th cycle. Although FEC is very effective in stabilizing the anode–electrolyte interface, it may not be suitable for applications in high-temperature batteries.

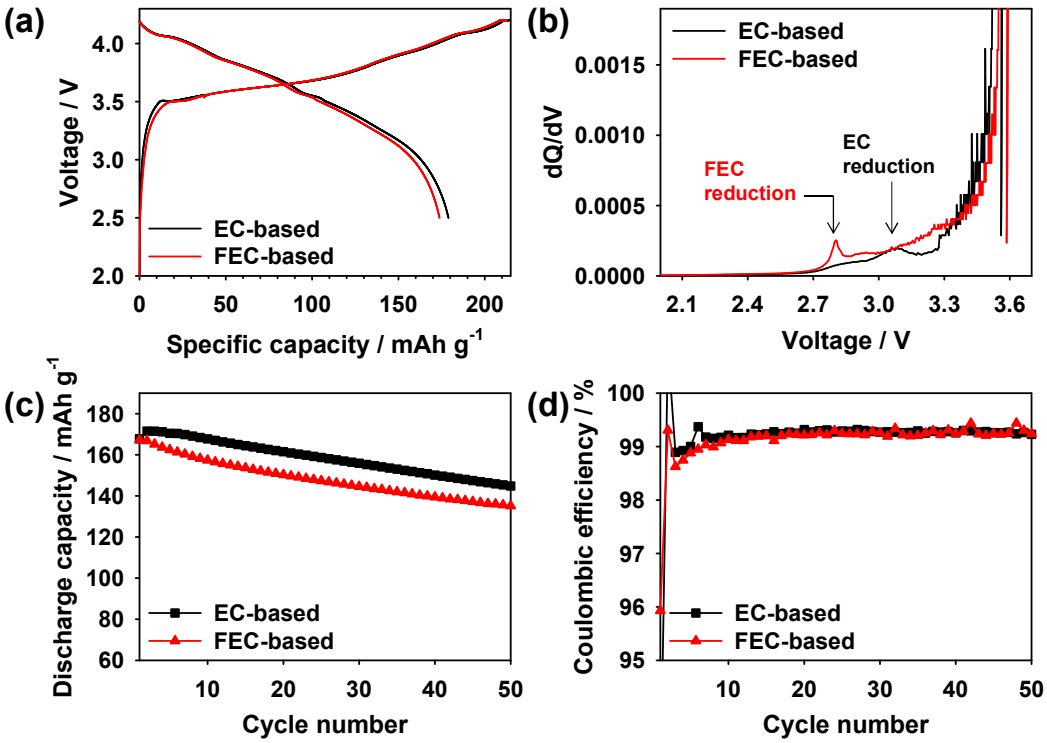

Figure 2.1 Electrochemical performances of LCO-NCM/Si-C full cells: (a) Voltage profiles and (b) dQ/dV plots at a rate of C/20 and 30 °C in the precycle. (c) Discharge capacity and (d) Coulombic efficiency at a rate of 1 C and 60 °C.

Presence of the FEC-derived SEI layer on the anode was confirmed by the ex situ XPS results provided in Figure 2.2. The F 1s, C 1s, and P 2p XPS spectra were obtained for the anodes retrieved from full cells cycled for two cycles in EC- and FEC-based electrolytes. The F 1s XPS spectrum for the Si-C anode cycled in FEC-based electrolyte shows three types of fluorine (Figure 2.2b): Fluorine bonded to phosphorous (P–F; 687.5 eV), fluorine bonded to carbon (C–F; 686.2 eV), and lithium fluoride (LiF; 685.0 eV). A noticeable feature is the appearance of the peak assigned to the C–F bond at 686.2 eV that is not observed in the corresponding spectrum of the EC-based electrolyte. The C–F peak can be produced by FEC decomposition (FEC (l) + Li^+ + e^- → CH_2=CHF (s) + Li_2CO_3 (s), CH_2=CHF → C−F-containing polymeric species).[70] Comparison of the C 1s spectra for the Si-C anode surface cycled in the EC- or FEC-based electrolyte (Figure 2.2c and d) provides further evidence for the presence of the C–F moieties on the anode surface: Clearly, a more pronounced peak appeared at 288.0 eV in the spectrum of the anode cycled in the FEC-based electrolyte; this is probably because, upon FEC decomposition, the FEC-based electrolyte generated organic species that contain C–F groups on the anode, which contributed to the increment in the ester (-CO_2-) peak intensity at 288 eV. Importantly, the LiF peak intensity at 685.0 eV was significantly higher for the FEC-based electrolyte than for the EC-based electrolyte, as shown in Figure 2.2b. This result suggests that FEC produces LiF as the main component of the SEI on the Si–C anode. LiF formation via reductive decomposition of FEC can be explained by two possible mechanisms: (1) LiF formation through a reaction of Li with HF that is generated upon defluorination of FEC (FEC (l) → VC (l) + HF (g))[82] and (2) LiF formation via the reaction of HF with SEI components such as Li_2CO_3 (Li_2CO_3 (s) + 2HF (g) → 2LiF (s) + H_2O (l) + CO_2 (g)↑).[83] Additional differences between the FEC- and EC-derived SEIs are apparent in the P 2p XPS results shown in Figure 2.2e and f. In the case of the FEC-based electrolyte, more pronounced peaks corresponding to phosphate (P–O) species appeared at 134.7 and 133.8 eV. Compounds with phosphate moieties ($3ROCO_2Li$ (s) + OPF_3 (g) → $O=P(RO)_3$ (s) + 3LiF (s) + $3CO_2$ (g), R = alkyl group) could be generated by a reaction between lithium alkyl carbonates and phosphoryl fluoride.[84-85] Phosphoryl fluoride (OPF_3), which is responsible for the formation of the phosphate species, is produced by hydrolysis of the $LiPF_6$ salt, as follows:[86]

$$LiPF_6\ (s) \leftrightarrow LiF\ (s) + PF_5\ (g) \quad (2.1)$$

$$PF_5\ (g) + H_2O\ (l) \rightarrow POF_3\ (g) + 2\ HF\ (g) \quad (2.2)$$

FEC, which has a relatively low dielectric constant of 78.4 at 40 °C compared to that of EC (90.5 at 40 °C), may impair the dissociation of $LiPF_6$ in the electrolyte and expedite the forward reaction presented in Equation (2.1) producing reactive PF_5 Lewis acid.[87-88] The resulting PF_5 may react with trace water to form POF_3, as presented in Equation (2.2). Tasaki et al. suggested that POF_3 can be produced by the reaction of $LiPF_6$ or PF_5 with Li_2CO_3, which is one of the representative SEI

components derived by the decomposition of carbonate-based electrolytes, as shown in Equation (2.3) and (2.4).[86]

$$Li_2CO_3\ (s) + LiPF_6\ (s) \rightarrow 3LiF\ (s) + POF_3\ (g) + CO_2\ (g) \quad (2.3)$$

$$Li_2CO_3\ (s) + PF_5\ (g) \rightarrow 2LiF\ (s) + POF_3\ (g) + CO_2\ (g) \quad (2.4)$$

From these mechanisms, it is apparent that the FEC-based electrolyte promotes unwanted decomposition of the $LiPF_6$ salt and forms the SEI with a relatively large fraction of phosphate species on the Si–C anode surface.

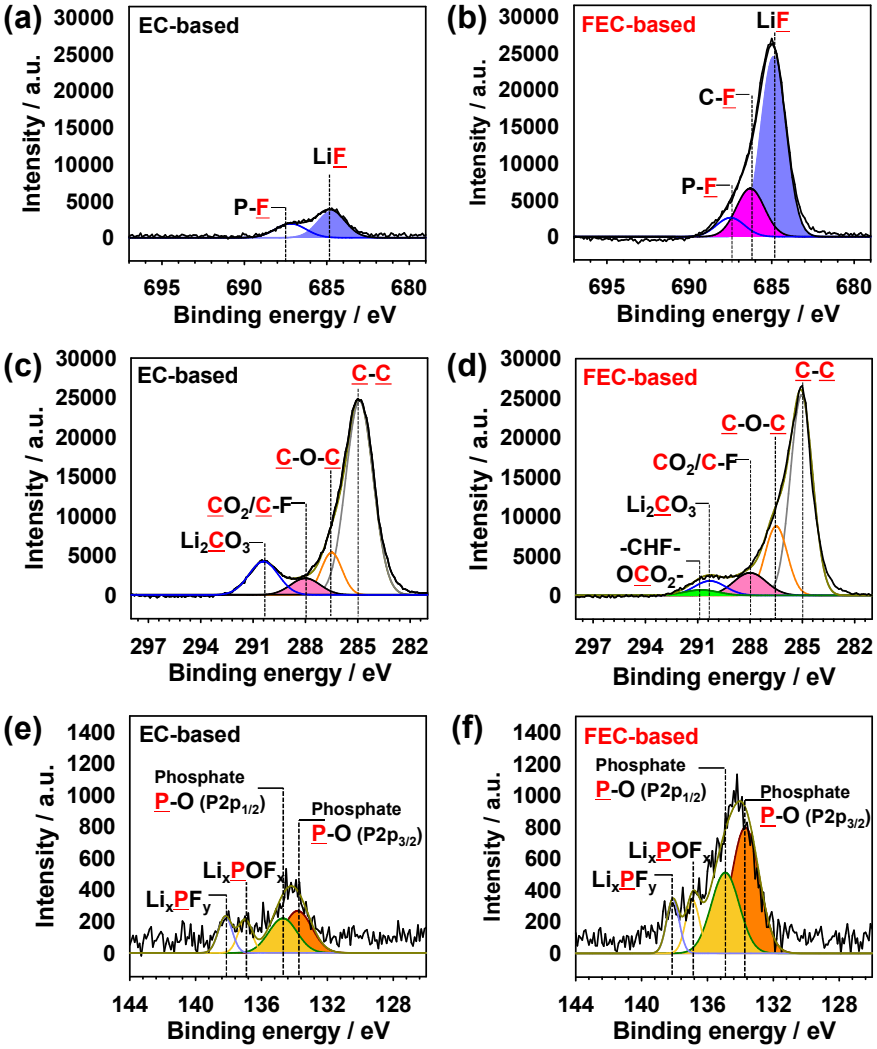

Figure 2.2 XPS spectra of Si-C electrodes from LCO-NCM/Si-C full cells after two cycles: (a) and (b) F 1s spectra, (c) and (d) C 1s spectra, and (e) and (f) P 2p spectra.

To elucidate the effect of the FEC-based electrolyte on the cycling performance of LCO-NCM/Si-C full cells at elevated temperatures, the high-temperature storage performances of LCO-NCM/Si-C full cells, LCO-NCM/Li half cells, and Si-C/Li half cells were examined at 45 °C. As shown in Figure 2.3a and b, the LCO-NCM/Li and Si-C/Li half cells with FEC-based electrolyte exhibited superior discharge capacity retentions than those with the EC-based electrolyte after storage at 45 °C for 20 days. However, the full cell with the FEC-based electrolyte had a slightly reduced discharge capacity of 147.4 mAh g^{-1} and inferior discharge capacity retention of 82.9 %, as shown in Figure 2.3b and d. This indicates that the FEC-based electrolyte does not effectively restrain the self-discharge of LCO-NCM/Si-C full cells. The detrimental effect of the FEC-based electrolyte on the high-temperature storage performance of fully charged full cells can be explained by the dissolution of metal ions from the delithiated cathode. The transition metal (i.e., Mn, Ni, and Co) ions that dissolve from the cathode can move toward a lithiated Si-C anode when the full cell is stored at 45 °C; consequently, metal deposition occurs on the anode surface. Deposition of metal ions leads to the removal of electrons from the fully lithiated Si-C anode in a full cell; this electron consumption via metal reduction results in the extraction of Li ions from the anode, which causes an increase in the anode potential and capacity loss of the LCO-NCM/Si-C full cell with the limited Li^+ source.

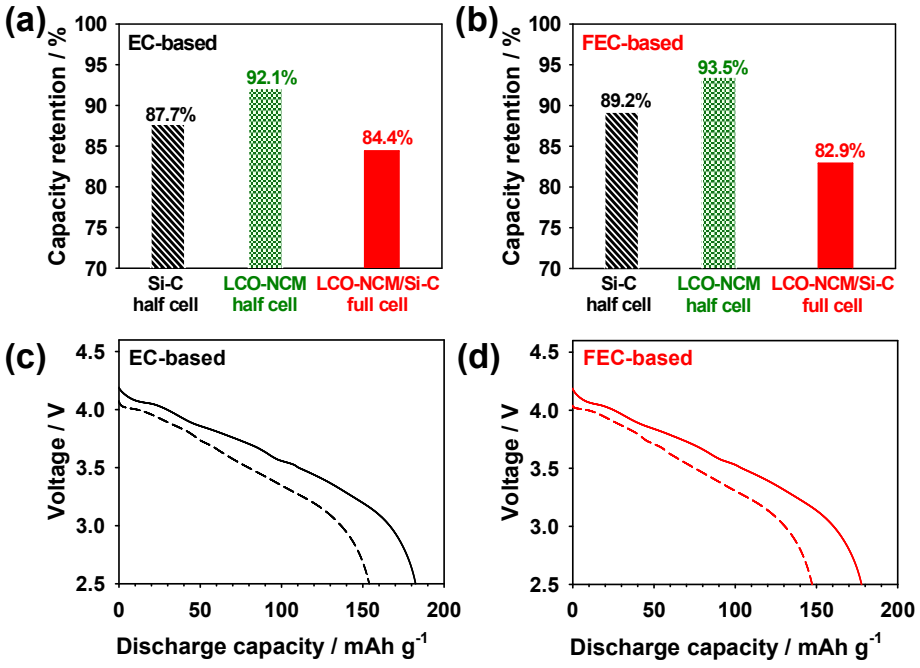

Figure 2.3 Capacity retention of cells stored for 20 days at 45 °C in a fully charged state: (a) EC-based electrolyte and (b) FEC-based electrolyte. Discharge capacity curve of the cells before (solid line) and after storage (dashed line): (c) EC-based electrolyte and (d) FEC-based electrolyte.

To clarify the effect of FEC on the dissolution behavior of transition metal (i.e., Ni, Co, and Mn) ions dissolved from fully delithiated LCO-NCM cathodes, the cathodes were analyzed by ICP-MS after storage in the EC- and FEC-based electrolytes for 24 h at 60 °C. Fully delithiated LCO-NCM cathodes were prepared by charging the cathode to 4.3 V in the EC-based electrolyte to generate the same surface chemistry as that of the cathode. As is clearly evident in Figure 2.4, the FEC-based electrolyte resulted in much more significant transition metal dissolution into the electrolyte than the EC-based electrolyte. A possible mechanism for the dissolution of transition metals from the cathode at elevated temperatures is demonstrated in Figure 2.5. Destruction of the SEI structure on the cathode may result in additional exposure of the cathode surface to the electrolyte, which promotes metal ion dissolution upon attack by HF. Since the cathodes used for the ICP measurements of the electrolytes have the same SEI structure, the stability of the SEI layer at 60 °C is thought to be significantly affected by the electrolyte composition. For instance, Li_2CO_3 in the SEI can be transformed to LiF by a reaction between Li_2CO_3 and HF in the electrolyte (Li_2CO_3 (s) + 2HF (l) → 2LiF (s) + H_2O (l) + CO_2 (g)↑), as illustrated in Figure 2.5a. The relatively significant transition metal dissolution into the FEC-based electrolyte may be ascribed to more severe SEI destruction caused by the attack of HF generated by FEC decomposition at 60 °C. Interestingly, when a fully delithiated LCO-NCM cathode was stored in FEC without the $LiPF_6$ salt, transition-metal dissolution was negligible. Therefore, it is likely that the decomposition of FEC to form HF at elevated temperatures is promoted by the presence of $LiPF_6$. This investigation revealed that FEC is readily defluorinated in $LiPF_6$-containing electrolytes at 60 °C to produce a large amount of HF or various acid compounds in the electrolyte. As illustrated in Figure 2.5b, transition metal ions that dissolved from the delithiated LCO-NCM cathode can move toward the Si-C anode in a full cell and then deposit on the anode, resulting in self-discharge of the lithiated anode.

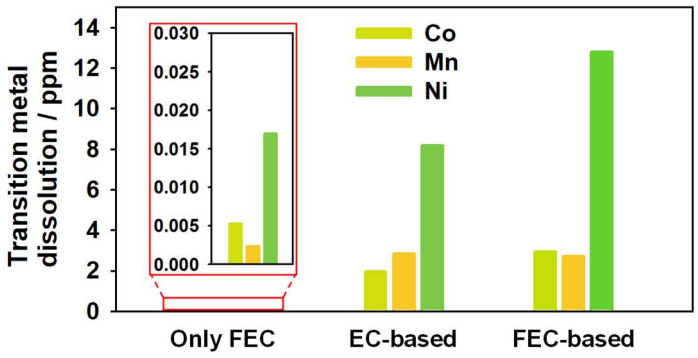

Figure 2.4 ICP-MS results showing the amounts of transition metals (Co, Mn, and Ni) in the FEC solvent, EC- and FEC-based electrolyte after storage with a fully delithiated LCO-NCM cathode with an EC-derived SEI layer for 24 h at 60 °C.

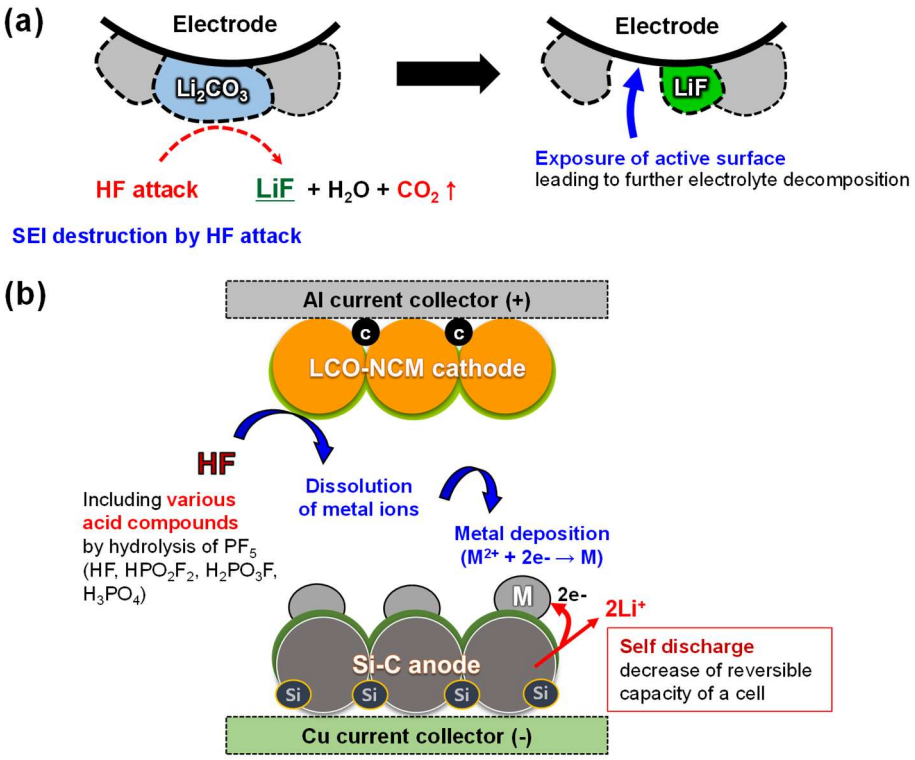

Figure 2.5 Schematic diagram of the possible problems related to HF and various acid compounds generated by decomposition of FEC: (a) Breakdown of the SEI layer upon HF attack and changes of the SEI composition and (b) transition metal dissolution from the LCO-NCM cathode and subsequent deposition on the Si-C anode, which induces the self-discharge of full cells.

Possible mechanisms of FEC decomposition in presence of $LiPF_6$ are proposed, as shown in Figure 2.6a. Lewis acid or HF promoted dehydrofluorination may afford olefin motif via E1 pathway.[89-91] This elimination-type formation of VC from FEC was also proposed by several research groups.[77,82] In addition, various polymer species with partially fluorinated structure and olefin motif can be also produced by the PF_5-catalyzed ring-opening reactions of FEC, as presented in Figure 2.6b.[92] It is thought that these FEC decomposition reactions stimulate the decomposition of PF_6^- anions as a non-coordinated conjugate base and lead to the formation of various acid compounds causing the increase of the acidity of FEC-based electrolyte.

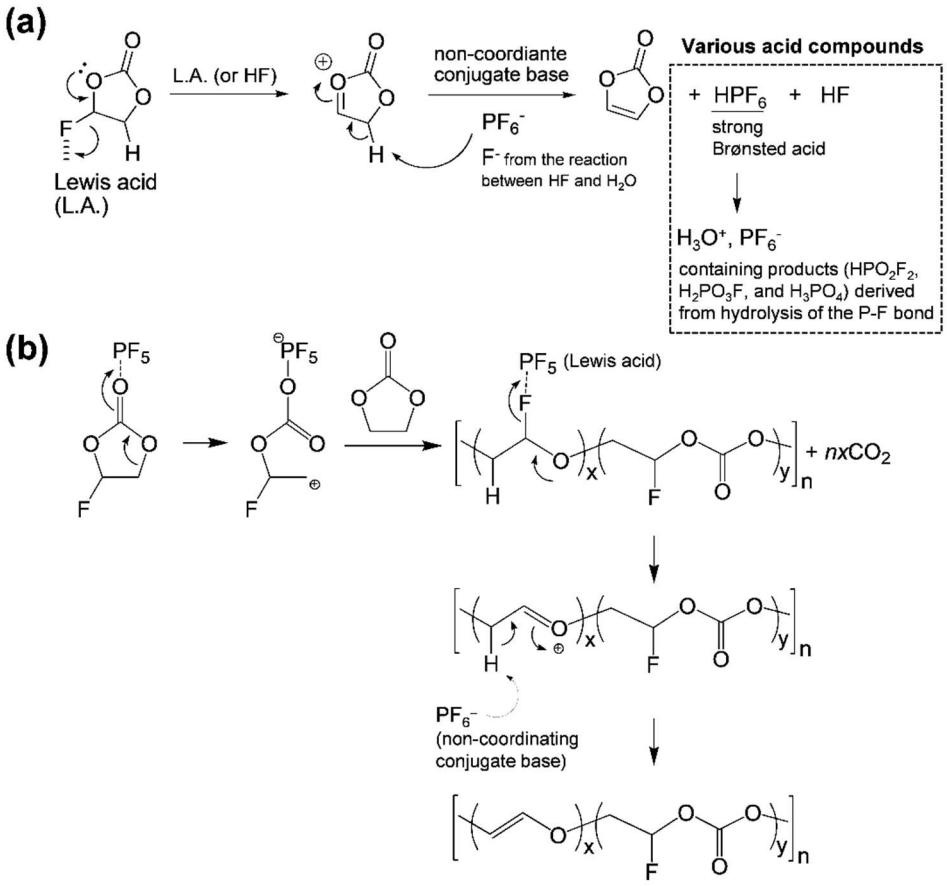

Figure 2.6 Possible mechanisms for (a) dehydrofluorination of FEC by Lewis acid (PF_5) or HF and (b) ring-opening reaction of FEC and the formation of polymer species with olefin motif.

Deposition of the transition metal ions on the anode was confirmed by the EDS spectra of the Si-C anodes retrieved from full cells after storage in the EC- or FEC-based electrolyte for 20 days at 45 °C. Interestingly, the metal ions preferentially deposited on the Si alloy particles instead of the graphite in the Si-C anode for both electrolytes (Figure 2.7i-l); this is probably because the SEI formed on the Si alloy particles is not thermally robust enough to preserve its original structure at 45 °C. Moreover, the relative fraction of Ni and Co signals on the Si alloy particles of the anode stored in the FEC-based electrolyte was slightly higher than that of the anode stored in the EC-based electrolyte, as shown in Figure 2.7f, h, j and l. A comparison of EDS patterns at the selected zone of the Si alloy particles after storage at 45 °C for 20 days more clearly shows that deposition of the transition metal (i.e., Mn) occurs on the Si alloy particles with the FEC-based electrolyte unlike the EC-based electrolyte (Figure 2.8). To further confirm more severe deposition of the transition metal ions on the Si-C anodes with the FEC-based electrolyte, the amounts of metal ions deposited on the Si-C anodes retrieved from LCO-NCM/Si-C full cells after storage for 20 days at 45 °C were measured by the ICP-MS measurements. As shown in Figure 2.9, the amounts of transition metal (Mn and Ni) ions in the Si-C anode with the FEC-based electrolyte was much higher compared to EC-based electrolyte. From these results, we speculate that transition metal ions are more severely dissolved from the delithiated LCO-NCM cathode in the FEC-based electrolyte.

This is consistent with the ICP results shown in Figure 2.4. Generation of HF and acid compounds from FEC decomposition catalyzed by PF_5 Lewis acid can cause SEI destruction on the electrodes and undesirable metal ion dissolution from the cathode in a full cell, as depicted in Figure 2.5b. HF and acid compounds may be produced through the defluorination of FEC promoted by PF_5 Lewis acid in the FEC-based electrolyte (Figure 2.6a). In particular, the ions that result from dissolution of transition metals promoted by HF may deposit on the anode in a full cell and lead to self-discharge of the lithiated anode resulting in decreased reversible capacity of a full cell (Figure 2.5b). Accordingly, the full cell with the FEC-based electrolyte exhibited inferior storage performance at 45 °C than that with the EC-based electrolyte, as shown in Figure 2.3.

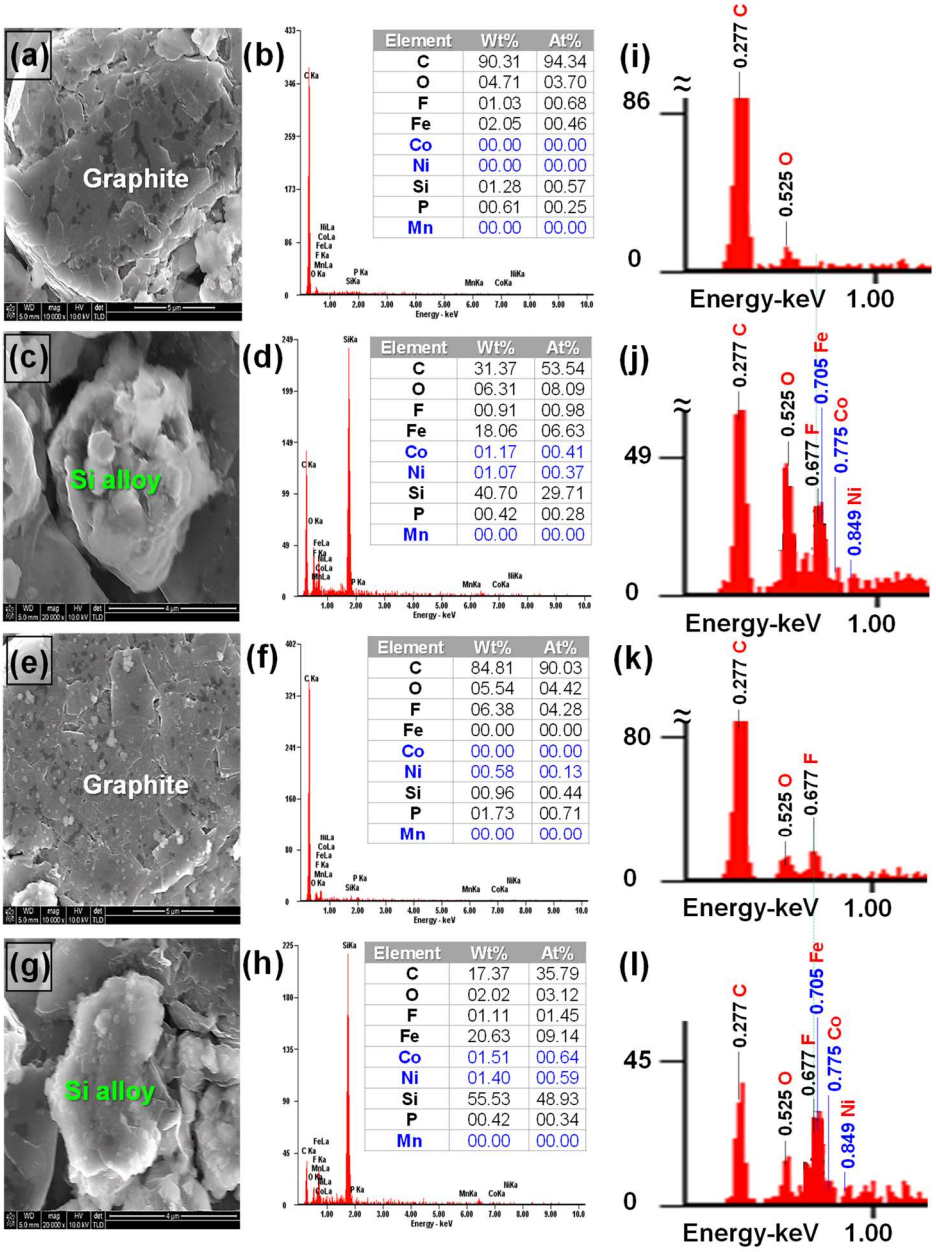

Figure 2.7 SEM images of Si-C anodes after storage for 20 days at 45 °C: (a) Graphite and (b) Si alloy with EC-based electrolyte and (c) graphite and (d) Si alloy with FEC-based electrolyte. EDS patterns of Si-C anodes after storage for 20 days at 45 °C: (e) graphite and (f) Si alloy with EC-based electrolyte and (g) graphite and (h) Si alloy with FEC-based electrolyte. Enlarged EDS patterns of Si-C anodes after storage for 20 days at 45 °C: (i) graphite and (j) Si alloy with EC-based electrolyte and (k) graphite and (l) Si alloy with FEC-based electrolyte.

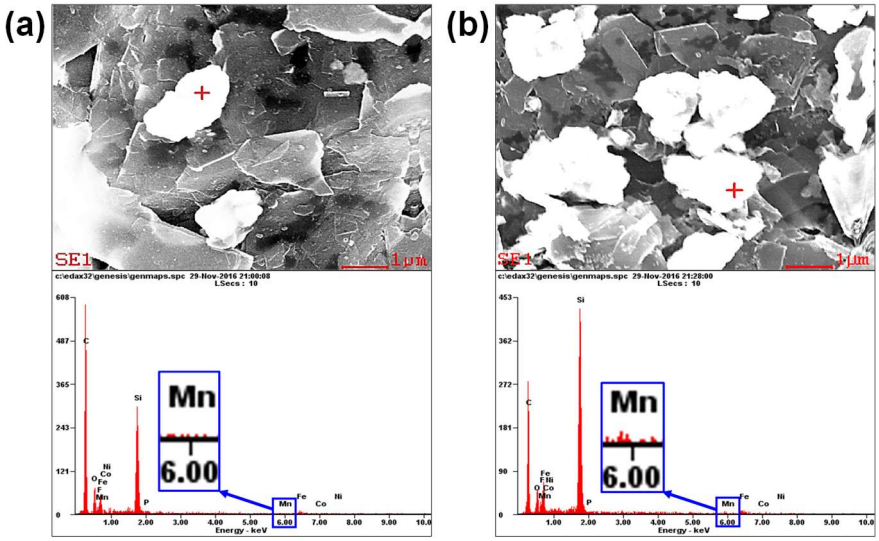

Figure 2.8 SEM images of Si-C anodes retrieved from LCO-NCM/Si-C full cells with (a) EC-based electrolyte and (b) FEC-based electrolyte after storage for 20 days at 45 °C. EDS patterns were obtained at the selected zone of the Si alloy particles.

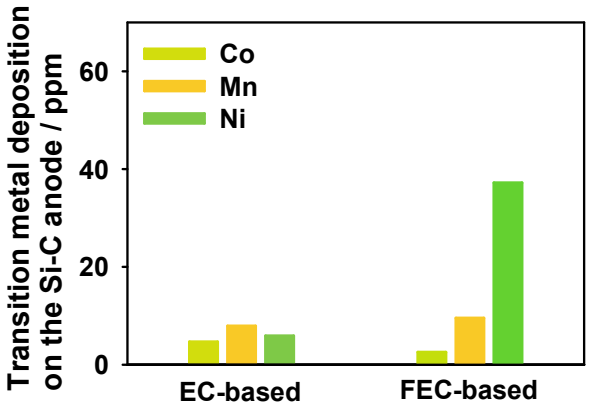

Figure 2.9 ICP-MS results showing the amounts of the transition metal (Co, Mn, Ni) in Si-C anodes retrieved from LCO-NCM/Si-C full cells after storage for 20 days at 45 °C.

Further evidence for the thermal instability of FEC in the presence of $LiPF_6$ is given in Figure 2.10. FEC, a mixed solvent of FEC/DEC (3/7, w/w), and DEC with and without 1.5 M $LiPF_6$ were stored at 60 °C for 3 days. The appearances of these three solvents without $LiPF_6$ before and after storage at 60 °C for three days were similar. There were no discernible color changes of the pH papers for FEC, the mixed solvent of FEC/DEC (3/7, w/w), and DEC without $LiPF_6$, as shown in Figure 2.10a, c, and e. Importantly, FEC and FEC/DEC with 1.5 M $LiPF_6$ exhibited substantial changes in their appearance after storage at 60 °C, as shown in Figure 2.10b and d: Their colors changed from colorless to black. In addition, the pH papers dipped in FEC with 1.5 M $LiPF_6$ became red, which indicates a strong acid; this is probably because many acidic compounds are produced in FEC with 1.5 M $LiPF_6$. In contrast, DEC with 1.5 M $LiPF_6$ did not exhibit a color change after storage at 60 °C, as presented in Figure 2.10f. The pH paper dipped in DEC with 1.5 M $LiPF_6$ changed from light orange to light red; this is mostly due to the various acid compounds generated by the $LiPF_6$ hydrolysis reactions containing Equation (2.2), as follows:

$$POF_3\,(g) + H_2O\,(l) \rightarrow PO_2F_2^-\,(l) + H^+\,(l) + HF\,(g) \quad (2.5)$$

$$PO_2F_2^-\,(l) + H^+\,(l) + H_2O\,(l) \rightarrow PO_3F^{2-}\,(l) + 2H^+\,(l) + HF\,(g) \quad (2.6)$$

$$PO_3F^{2-}\,(l) + 2H^+\,(l) + H_2O\,(l) \rightarrow PO_4^{3-}\,(l) + 3H^+\,(l) + HF\,(g) \quad (2.7)$$

This result indicates that FEC interacts with the $LiPF_6$ salt at the elevated temperature and PF_5, as a strong Lewis acid ($LiPF_6\,(s) \leftrightarrow LiF\,(s) + PF_5\,(g)$), initiates the FEC decomposition, which leads to the formation of HF and various acid compounds, as depicted in Figure 2.6a. Unlike FEC with 1.5 M $LiPF_6$, the discernible color change of EC with 1.5 M $LiPF_6$ after storage for 3 days at 60°C was not observed, as shown in Figure 2.11b. The pH paper dipped in EC with 1.5 M $LiPF_6$ stored for 3 days at 60 °C became light red. The Lucht group demonstrated that 1M $LiPF_6$ in pure EC treated under N_2 reacts very slowly at high temperatures and presence of protic impurities such as H_2O and ROH accelerates thermal decomposition of $LiPF_6$-based electrolyte.[93] Since the water content of EC-1.5 M $LiPF_6$ is 7.4 ppm, the small amount of POF_3 causing the EC decomposition may be formed. Because of this, it is though that the significant thermal decomposition of EC-1.5 M $LiPF_6$ does not occur. From the results of Figure 2.10b and 11b, it can be thought that the darkening of color of FEC with 1.5 M $LiPF_6$ is closely linked to the defluorination of FEC and the acceleration of PF_6^- anion decomposition induced by the FEC decomposition.

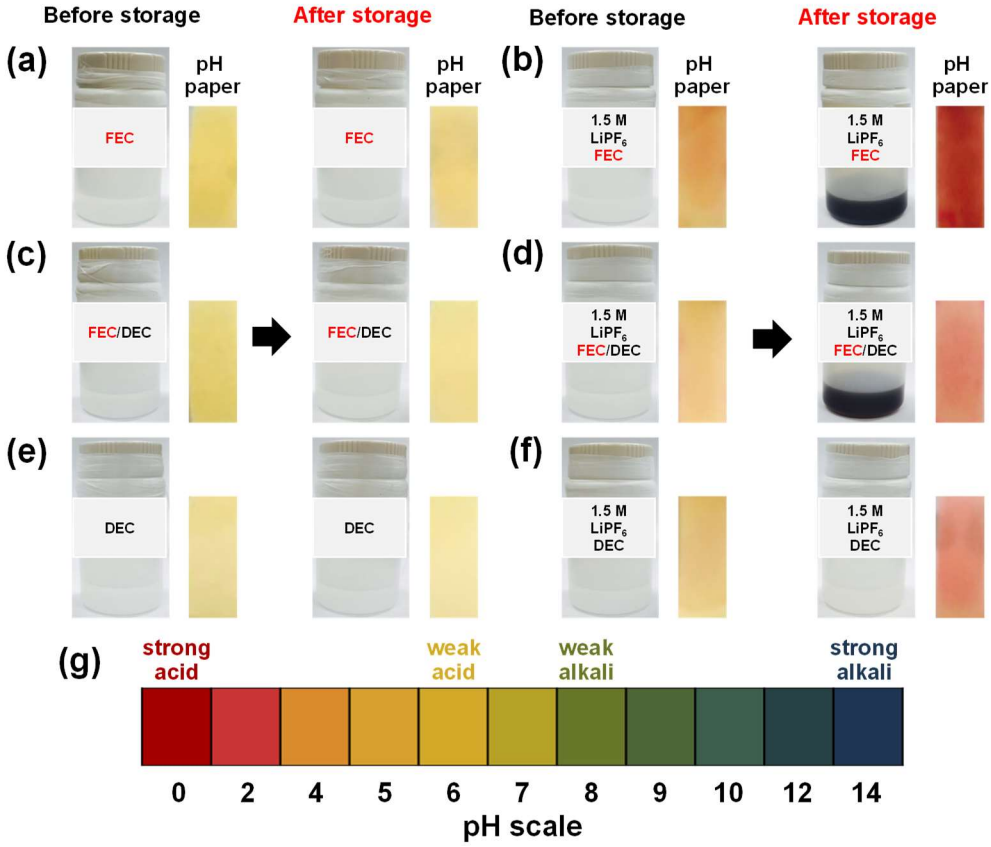

Figure 2.10 Photographs of the solvent mixtures: (a) FEC, (c) FEC/DEC (3/7, w/w), and (e) DEC without salt, and (b) FEC, (d) FEC/DEC (3/7, w/w), and (f) DEC with 1.5 M $LiPF_6$ salt before and after storage for 3 days at 60 °C. (g) Indicator chart for the pH scale.

A comparison of the thermal stability of FEC with different lithium salts (i.e., $LiPF_6$, $LiN(SO_2CF_3)_2$, and $LiSO_3CF_3$) at 60 °C clearly shows that FEC readily undergoes severe thermal decomposition in the presence of the $LiPF_6$ salt and the darkening of color of FEC with 1.5 M $LiPF_6$ appears (Figure 2.11c and d); therefore, $LiN(SO_2CF_3)_2$ and $LiSO_3CF_3$ salts could be used as alternatives to avoid the thermal decomposition of FEC at 60 °C because they do not produce the compounds that act as Lewis acids.

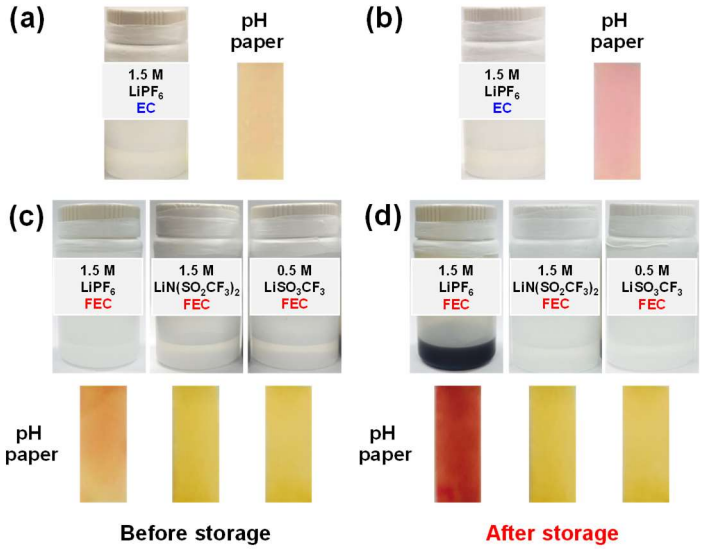

Figure 2.11 Photographs of 1.5 M $LiPF_6$ in EC (a) before and (b) after storage for 3 days at 60 °C. Photographs of 1.5 M $LiPF_6$, 1.5 M lithium bis(trifluoromethane)sulfonimide ($LiN(SO_2CF_3)_2$) and 0.5 M lithium trifluoromethane sulfonate ($LiSO_3CF_3$) salt dissolved in FEC (c) before and (d) after storage for 3 days at 60 °C. Indicator chart for the pH scale is presented in Figure 2.10g.

To elucidate the effect of Lewis acids, such as the PF_5 formed in $LiPF_6$-based electrolyte, on the defluorination of FEC, a model experiment was conducted. Tris(pentafluorophenyl)borate (TPFPB), which is known as a strong Lewis acid, was introduced to FEC without the $LiPF_6$ salt. In the presence of 0.06 M TPFPB, FEC became brown and changed the color of pH paper to reddish after storage for only 24 h at room temperature, as shown in Figure 2.12a. This is because TPFPB, as a strong Lewis acid, vigorously interacts with the FEC molecules to extract HF and promotes FEC decomposition. The decomposition product of 0.06 M TPFPB in FEC after storage for 24 h at room temperature was confirmed using ^{13}C NMR spectroscopy. The peak assigned to the C=C double bond of the VC molecule appeared at 135.3 ppm in Figure 2.12b. A possible mechanism for HF generation from FEC by the TPFPB Lewis acid is illustrated in Figure 2.12c: The electron-deficient boron atoms of TPFPB can interact with the fluorine atoms of the FEC molecules; the resulting strong ion-dipole interaction causes FEC decomposition to form VC, H^+, and a TPFPB-F complex. Therefore, it is clear that Lewis acid promotes dehydrofluorination of FEC and may form olefin motif via E1 pathway, as shown in Figure 2.6a.

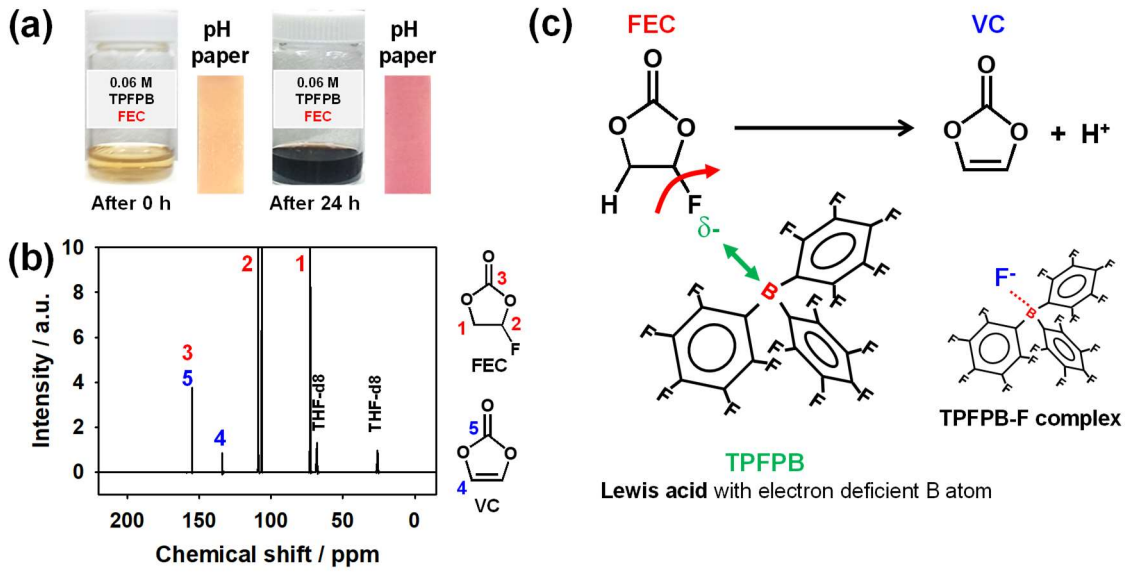

Figure 2.12 (a) Photographs of 0.06 M tris(pentafluorophenyl)borane (TPFPB) in FEC stored at room temperature. (b) ^{13}C NMR spectrum of 0.06 M TPFPB in FEC after 24 h at room temperature. (c) Schematic diagram of the interaction between FEC and TPFPB.

2.4 Conclusion

Our investigation revealed that Lewis acids, such as PF_5, in $LiPF_6$-based electrolytes caused the defluorination of FEC, which was used as a co-solvent, and consequently, excess HF formed in the cell. The defluorination of FEC by PF_5 Lewis acid and the decomposition of PF_6^- anions induced by the FEC decomposition can be accelerated at elevated temperatures. The undesirable formation of HF and acid compounds that occurs upon defluorination of FEC promoted transition metal ion dissolution from the LCO-NCM cathode at elevated temperatures; this transition metal dissolution results in a self-discharge of the Si-C anode in a full cell coupled with an LCO-NCM cathode. As a result, we have observed inferior cycling properties and storage performance of LCO-NCM/Si-C full cells with the FEC-based electrolyte at elevated temperatures. We believe that the results of this study and associated analysis will contribute to the design of electrolyte additives allowing the use of FEC in $LiPF_6$-based electrolytes and the development of new compounds replacing FEC for lithium ion batteries.

III. Dual-function ethyl 4,4,4-trifluorobutyrate additive for high performance Ni-rich cathodes and stable graphite anodes

3.1 Introduction

Potential candidates of cathode materials for high energy-density LIB include Ni-rich layered oxides ($LiNi_xCo_yMn_zO_2$, $x > 0.6$), which can deliver a reversible capacity of ~200 mAh g^{-1}.[94-95] However, the Ni-rich cathodes suffer from structural degradation,[96-99] low thermal stability,[100-102] and parasitic reactions of electrolytes promoted by highly reactive Ni^{4+} ions generated at the end of the charge process.[103-109] The Ni^{4+} species formed in the charged state of the Ni-rich cathode may reduce the lower valence states of Ni such as Ni^{3+} and Ni^{2+} by accepting electrons from the electrolyte near the cathode surface. Moreover, the Ni^{2+} ions created by the reduction of Ni^{4+} at the cathode surface may lead to cation mixing, a major challenge in Ni-rich cathodes.[97-99] As cation mixing between Ni^{2+} (0.69 Å) and Li^+ (0.72 Å) ions takes place owing to their similar size, the surface of layered Ni-rich cathode materials undergoes a reconstruction from the $R\bar{3}m$ to a spinel ($Fd\bar{3}m$) phase, and eventually to the rock salt ($Fm\bar{3}m$) phase. The Ni^{2+} ions located in the lithium layer of the Ni-rich cathode severely inhibit lithium ion diffusion and lead to poor rate capability of the cathode. Another critical issue affecting Ni-rich cathodes is intergranular cracking induced by internal stress in the secondary particles during charge and discharge processes.[96] Intergranular cracking between primary particle aggregates in the secondary particles results in the exposure of fresh cathode particle surfaces to the electrolyte and repeated irreversible side reactions in the electrolyte upon repeated cycling. The undesirable electrolyte decomposition in the inner regions of the cathode leads to the accumulation of non-conductive solid byproducts in the secondary cathode particles, blocks the electronic conduction paths, and significantly reduces the energy storage ability of the cathode. Therefore, the protection of the surface of Ni-rich cathodes is a key requirement to inhibit their structural deterioration and improve their electrochemical properties. The formation of a cathode electrolyte interphase (CEI) via electrolyte additives is considered a cost-effective and reliable way to achieve the protection of the cathode, because the stable CEI layer uniformly distributed over the entire cathode surface prevents its direct contact with the electrolyte and allows homogeneous electrochemical reactions over the cathode surface. Uniform lithium insertion/deinsertion on the surface of primary cathode particles tightly aggregated in spherical secondary particles circumvents the structural issues associated with intergranular cracking induced by anisotropic volume changes. Moreover, the fully developed CEI effectively prevents further oxidative decomposition of the electrolyte, limits the reduction of Ni^{3+} and Ni^{4+} ions to Ni^{2+} by blocking the supply of electrons generated from decomposition of the electrolyte and/or metastable solid byproducts in the CEI, and is expected to minimize cation mixing between Li^+ and Ni^{2+} at the cathode surface. The residual Li species on the Ni-rich cathode surface are detrimental to the interfacial stability of the cathode, because their direct reaction with $LiPF_6$ to form HF may

promote dissolution of transition metal ions and impair the CEI structure on the electrode.[110-111] In this respect, many efforts have been devoted to stabilizing the interface between the Ni-rich cathode and the electrolyte, using electrolyte additives for in situ fabrication of a thin and stable artificial CEI layer on the cathode. Yu et al. reported the formation of a protective film on a $LiNi_{0.7}Co_{0.2}Mn_{0.1}O_2$ cathode through a divinyl sulfone additive composed of sulfone groups (-SO_2-, the main component of the protective film) and vinyl (-C=C-) moieties, whose π-electron functionalities contribute to the formation of a cross-linked protective layer and stabilize the sulfone-based SEI intermediate, improving the cycling performance of a Li/$LiNi_{0.7}Co_{0.2}Mn_{0.1}O_2$ half-cell at high temperatures.[105] It was also demonstrated that thermal polymerization of an epicyanohydrin additive in the SEI covering the surface of a $LiNi_{0.6}Co_{0.2}Mn_{0.2}O_2$ cathode mitigated its capacity loss at 60 °C.[106] In addition, a *p*-toluenesulfonyl isocyanate additive produced a CEI containing -S=O and -NCO functional groups, protecting the $LiNi_{0.5}Co_{0.2}Mn_{0.3}O_2$ cathode under high voltages of 4.5 V vs. Li/Li^+ and thus preventing the deterioration of the cathode structure, resulting in improved cycling performance.[107] The authors demonstrated that the S=O functional group can delocalize the electrons of the nitrogen core serving as a weak basic site to reduce the reactivity of the PF_5 Lewis acid, and the NCO groups can be polymerized into a protective film on the $LiNi_{0.5}Co_{0.2}Mn_{0.3}O_2$ cathode. In addition, 1-propylphosphonic acid cyclic anhydride was found to be an efficient additive to improve the capacity retention of a $LiNi_{0.5}Co_{0.2}Mn_{0.3}O_2$ cathode coupled with a graphite anode and reduce the structural degradation of the cathode.[108] However, a fundamental understanding of the effect of the additives on the interfacial structure and structural stability of Ni-rich cathodes has not yet been achieved.

Herein, we demonstrate that minimal amounts (1 wt.%) of ethyl 4,4,4-trifluorobutyrate (ETFB) used as an electrolyte additive enable the fabrication of high-performance batteries composed of a Ni-rich layered cathode ($LiNi_{0.7}Co_{0.15}Mn_{0.15}O_2$, NCM) and a graphite anode, at practical mass loading levels (25.6 mg cm^{-2} for the NCM cathode and 13.6 mg cm^{-2} for the graphite anode). Our investigation reveals that ETFB forms a stable CEI, resolving critical issues such as poor mechanical integrity, structural instability, and electrochemical degradation of the NCM cathodes, and ensures the structural stability of the interface formed at the graphite anode. Electrochemical tests confirm that the solid electrolyte interface (SEI)-forming ability of ETFB in a full cell exceeds that of vinylene carbonate (VC), widely used as a standard additive for batteries with a graphite anode. Scanning electron microscopy (SEM) measurements clearly show that the ETFB-induced CEI significantly reduces mechanical fractures in NCM secondary particles, associated with severe intergranular cracking. The favorable effects of ETFB on the surface chemistry of the NCM cathode and graphite anode were investigated through ex situ X-ray photoelectron spectroscopy (XPS) measurements. We also propose possible mechanisms by which ETFB, serving as a bifunctional additive, promotes the formation of the CEI on NCM cathode and the SEI on graphite anode in a full cell.[112]

3.2 Experimental method

Electrolyte and electrodes

The baseline electrolyte was composed of 1.15 M lithium hexafluorophosphate ($LiPF_6$) dissolved in a solvent mixture of ethylene carbonate (EC), ethyl methyl carbonate (EMC), and diethyl carbonate (DEC) in a 2:5:3 volume ratio. Electrolytes containing 1 wt.% ETFB (≥ 98%, Sigma-Aldrich) or 1 wt.% VC (Soulbrain Co., Ltd.) were prepared by adding the corresponding additive to the baseline electrolyte. All solvents and $LiPF_6$ salt were purchased from Soulbrain Co., Ltd. The mixed solvents (EC/EMC/DEC (2/5/3, v/v/v)) were treated with calcium hydride (CaH_2, 95%, Sigma-Aldrich) to minimize the water content, before dissolving $LiPF_6$ in their mixture to prepare the electrolytes. The water content of the electrolytes was confirmed to be less than 10 ppm by Karl-Fischer titration (Mettler Toledo, C30). The Ni-rich NCM cathode was prepared by coating a slurry composed of 94 wt.% active material, 3 wt.% Super C, and 3 wt.% poly(vinylidene fluoride) (PVDF 6020) dissolved in anhydrous *N*-methyl-2-pyrrolidinone (NMP, 99.5%, Aldrich) on aluminum foil, followed by drying in a convection oven at 80 °C for 30 min. After drying, the electrode was pressed to a thickness of approximately 15 μm. The thickness, areal capacity, and loading density of the cathode of the half cells were 15 μm, 0.8 mAh cm^{-2}, and 4.2 mg cm^{-2}, respectively, whereas those of the full cells were 80 μm, 4.86 mAh cm^{-2}, and 25.6 mg cm^{-2}, respectively. The anode consisted of 97.5 wt.% graphite as active material and 2.5 wt.% binder (1.5 wt.% styrene-butadiene rubber + 1 wt.% sodium carboxymethyl cellulose) dissolved in distilled water. The thickness, areal capacity, and loading density of the graphite anode were 83 μm, 4.90 mAh cm^{-2}, and 13.6 mg cm^{-2}, respectively. To remove adsorbed water, the electrodes were dried in a vacuum oven at 110 °C for 12 h before cell assembly.

Electrochemical measurements

Electrochemical tests were performed using 2032 coin-type full cells assembled with a microporous polyethylene film (SK innovation Co., Ltd) separator with thickness and porosity of 20 μm and 38%, respectively, in an argon-filled glove box (O_2 and H_2O < 1 ppm). NCM/graphite full cells were galvanostatically precycled at a rate of C/10 between 3.0 and 4.35 V at 25 °C, using a computer-controlled battery testing equipment (WonATech, WBCS 3000). Constant voltage conditions were applied at the end of the precycle charging until the current was below C/50. Standard cycling was conducted on the full cells after precycling at a rate of C/5 between 3.0 and 4.35 V. Constant voltage conditions were applied at the end of the standard cycle charging until the current was below C/25. For the evaluation of the cycling performance, the full cells were cycled at a rate of C/2 at 25 or 45 °C. Constant voltage conditions were applied after every cycle at the end of charging process, until the current was less than C/25. To examine the effect of the ETFB additive on the high-temperature storage performance, the full cells were charged up to 4.35 V after precycling at a rate of C/10 and a

temperature of 25 °C, and then stored for 20 days at 60 °C. Electrochemical floating tests were performed for 2 h on Li/NCM half cells with baseline and 1% ETFB-added electrolytes, at a constant voltage of 4.4 V vs. Li/Li^+.

Characterization

To recover the electrodes for ex situ analysis, the NCM/graphite full cells were carefully disassembled in a glove box after each electrochemical measurement. The retrieved electrodes were rinsed in DMC to remove the residual electrolyte and then dried at room temperature in a glove box. The surface and cross-sectional morphologies of the NCM cathodes were inspected by field emission scanning electron microscopy (FE-SEM, FEI, Nova NanoSEM). The cross-section of the NCM cathodes was prepared by an ion-milling system (Hitachi High-Technologies Co., IM4000) equipped with an Ar ion beam. The surface chemistry of the electrodes was investigated by ex situ XPS (ThermoFisher, K-Alpha) with Al K_α ($h\nu$ = 1486.6 eV) radiation under ultrahigh vacuum. Before use, all samples were prepared in an argon-filled glove box, sealed with an aluminum pouch bag under vacuum, and then rapidly transferred into the vacuum chamber of the XPS instrument to minimize any possible contamination. The impedances of NCM/graphite full cells after cycling were measured by AC impedance analysis, using an IVIUM frequency response analyzer over a frequency range from 0.01 Hz to 1 MHz. The fitting of impedance spectra was conducted by using ZVIEW. Inductively coupled plasma (ICP, Varian, 700-ES) analysis was used to measure the amount of transition metal ions (Co, Mn, and Ni) in electrolytes kept in contact with delithiated NCM cathodes at 60 °C for 5 days. To investigate the reactivity of $LiPF_6$ with LiOH, ^{19}F nuclear magnetic resonance spectroscopy (NMR, Agilent, VNMRS 600) was conducted on the baseline electrolyte with and without 1% LiOH, before and after storing at 60 °C for 3 days. The crystal structure of lithiated graphite anodes recovered from NCM/graphite full cells after storage at 60 °C was determined using XRD (Rigaku, D/MAX2500V/PC) with monochromatic Cu K_α radiation. The residual amounts of lithium compounds (LiOH and Li_2CO_3) were measured with a potentiometric titrator (Metrohm, 888 Titrando).

3.3 Results and discussion

Figure 3.1a presents the charge-discharge profiles of NCM/graphite full cells during precycling at 25 °C. The full cells with electrolytes containing 1% ETFB and 1% VC delivered slightly lower discharge capacities of 194 and 196 mAh g^{-1}, respectively, compared to those with the baseline electrolyte, whose discharge capacity was 198 mAh g^{-1}. In addition, their initial Coulombic efficiency (ICE) values (87.4% for ETFB- and 88.0% for VC-containing cells) were lower than that of cells with the baseline electrolyte (88.8%). The reduced ICE indicates that the ETFB and VC additives consume the limited number of Li ions and electrons present in a cell to form the SEI and CEI layer at the electrode-electrolyte interface. To understand the role of VC and ETFB, we compared the dQ/dV (differential capacity) plots of the full cells, showing the reductive decomposition voltages of the electrolytes (Figure 3.1b). VC, which is considered a standard additive for SEI formation on the graphite anode, started undergoing electrochemical reduction at the lowest voltage (onset of 2.86 V and peak potential of 2.93 V) by accepting electrons at the graphite anode, and a further reduction peak appeared at around 3.02 V. The high reduction tendency of VC is mostly due to the low energy of its lowest unoccupied molecular orbital (LUMO) level (Figure 3.1c). This result suggests that VC predominantly builds up the SEI at the graphite. ETFB, possessing a lower LUMO energy level than the EC, EMC, and DEC solvents, acted as an electron acceptor at the graphite during precycle charging and showed two peaks at different voltages (2.95 and 3.04 V) compared to the peaks associated with EC reduction. The reductive decomposition of ETFB started at a low voltage of 2.95 V, forming reactive radicals that initiated the EC reduction, and a reduction voltage indicating co-decomposition of ETFB and EC appeared at 3.04 V. Clearer evidence that the ETFB reduction occurred at around 3 V is provided by the dQ/dV plot of NCM/graphite full cells precycled in EC-free electrolytes (EMC/DEC/1.15 M $LiPF_6$ with and without 1% ETFB, Figure 3.1d). EMC/DEC-based electrolytes without the reducing EC solvent showed a reduction voltage of 3.40 V, higher than that of EC-containing electrolytes. This is due to the relatively high LUMO energy levels of EMC and DEC compared to EC. The introduction of ETFB in the EC-free electrolytes led to the appearance of an additional reduction peak at 3.02 V with an onset voltage of 2.95 V, and the reduction peak of the EMC/DEC-based electrolyte was shifted to low voltages. This result suggests that the reactive species generated from ETFB decomposition promote the reduction of the EMC/DEC-based electrolyte. The dQ/dV results confirm that ETFB undergoes reductive decomposition at the graphite anode during the initial charge process and its reactive intermediate species combine with EC molecules to produce the SEI on the anode.

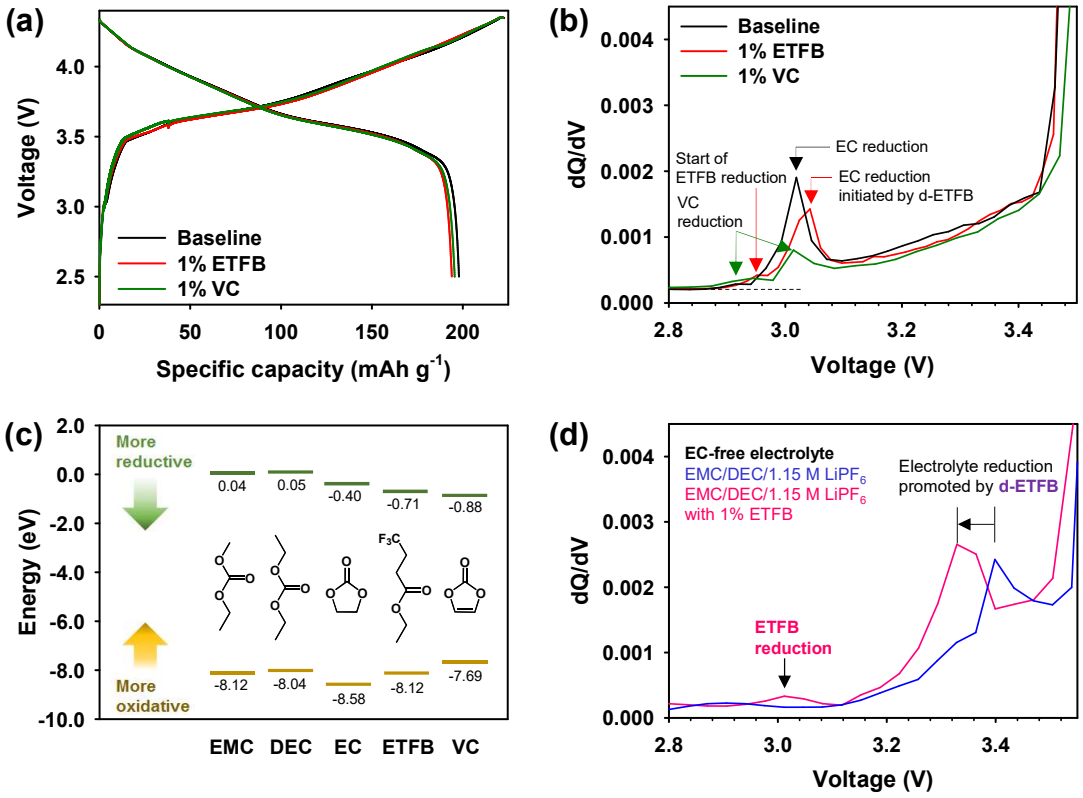

Figure 3.1 (a) Charge-discharge curves and (b) dQ/dV plots of NCM/graphite full cells with baseline, 1% ETFB-containing, and 1% VC-containing electrolytes measured at a C/10 rate and 25 °C during precycling. (c) Chemical structures and HOMO-LUMO energy values of carbonate solvents (EC, EMC, and DEC) and additives (ETFB and VC). (d) dQ/dV plots of NCM/graphite full cells with EC-free electrolytes (EMC/DEC/1.15 M $LiPF_6$ with and without 1% ETFB) measured at C/10 rate and 25 °C during precycling. d-ETFB denotes byproducts generated by ETFB reduction.

Figure 3.2a and b show a comparison of the cycling performance of NCM/graphite full cells containing baseline, 1% ETFB, and 1% VC electrolytes at a current density of 95 mA g^{-1} (corresponding to a C/2 rate) and temperatures of 25 and 45 °C. Although the baseline electrolyte delivered a high discharge capacity of 181 mA g^{-1} in the first cycle, the capacity continuously decreased in the subsequent cycles at 25 °C compared to that of the cells with 1% ETFB- and 1% VC-added electrolytes. At the higher temperature of 45 °C, a more severe capacity degradation was observed for the baseline electrolyte, which delivered a very low capacity of 50 mAh g^{-1} (Figure 3.2b). Since the EC-derived SEI lacks the ability to preserve the electrochemical performance of graphite anodes, the use of an electrolyte additive capable to form an electrochemically stable SEI is vital. In fact, VC, the standard additive for graphite anodes, improved the discharge capacity retention of the full cells from 69.3% (baseline electrolyte) to 77.1% after 300 cycles at 25 °C. Full cells with 1% VC-added electrolyte delivered a capacity of 133 mAh g^{-1} and exhibited a significantly improved capacity retention of 70.1%, compared to the baseline electrolyte (26.5%) at 45 °C. Surprisingly, a superior cycling stability was achieved for full cells with the 1% ETFB-added electrolyte, which delivered a high capacity of 153 mAh g^{-1} with good discharge capacity retention of 83.4% over 300 cycles at 25 °C. This result reveals that ETFB is a more suitable additive for NCM/graphite full cells compared with VC. A more striking contrast among baseline, 1% VC, and 1% ETFB emerges from Figure 3.2b, which compares the cycling stability of NCM/graphite full cells at 45 °C. The 1% ETFB-containing cells delivered a discharge capacity of 167 mAh g^{-1} and exhibited a superior discharge capacity retention of 84.8% after 300 cycles, compared to that of baseline (26.5%) and 1% VC (70.1%) electrolyte-containing cells. This finding suggests that ETFB represents an effective additive for suppressing the irreversible electrolyte decomposition consuming Li ions and electrons at both electrodes, thus minimizing the capacity loss of the electrodes during repeated cycling at 25 and 45 °C. Upon application of a charge voltage cut-off of 4.35 V in the full cell, the voltage of the NCM cathode reached up to ~4.4 V vs. Li/Li^+ in the fully charged state. This high voltage, beyond the upper voltage limit of $LiPF_6$-based electrolytes (around 4.3 V vs. Li/Li^+), may lead to unwanted electrolyte decomposition at the NCM cathode. Although the VC additive is very effective in stabilizing the anode-electrolyte interface, its compatibility with NCM cathodes charged up to ~4.4 V vs. Li/Li^+ may not be satisfactory.

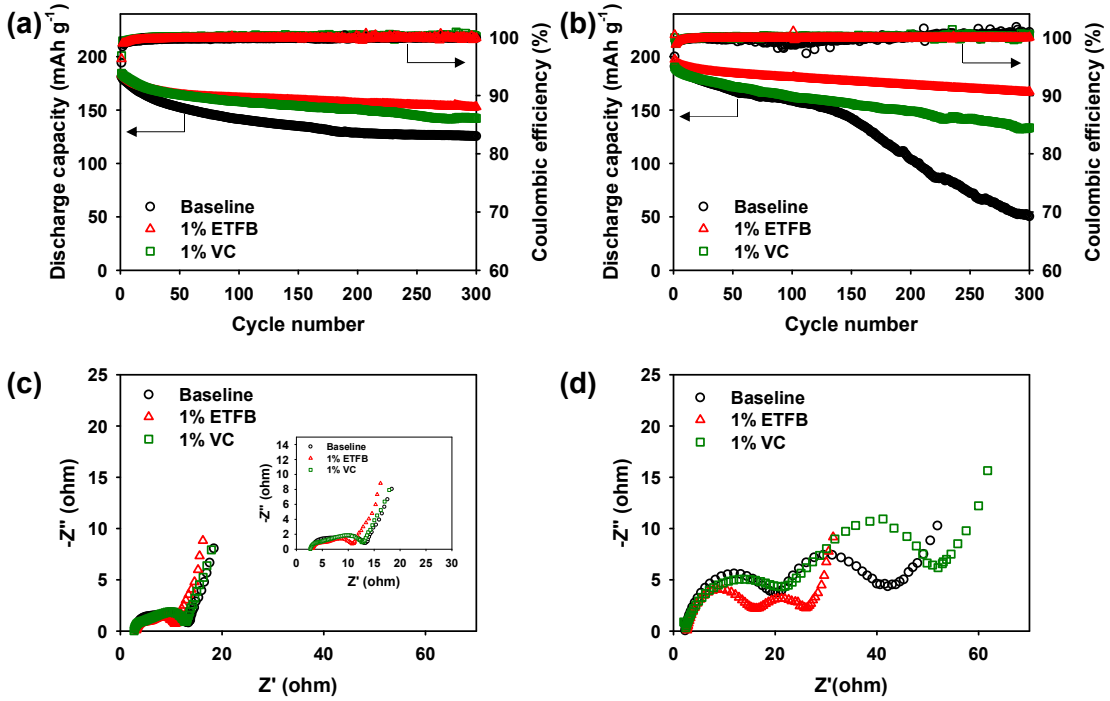

Figure 3.2 Discharge capacity and Coulombic efficiency of NCM/graphite full cells during 300 cycles at a C/2 rate and (a) 25 °C or (b) 45 °C. Nyquist plots of NCM/graphite full cells after 300 cycles at (c) 25 °C and (d) 45 °C. The inset shows an enlargement of the (c) plot.

The effect of the electrolytes on the electrode-electrolyte interface was investigated by comparing the resistance of the NCM/graphite full cells after 300 cycles at 25 and 45 °C (Figure 3.2c and d). The interfacial resistance (R_f+R_{ct}), including the resistance of the interfacial layer (sum of CEI and SEI, R_f) and the charge transfer resistance (R_{ct}) of the full cell with the 1% ETFB-added electrolyte was lower than those of cells with baseline and 1% VC-added electrolytes, as showed in Table 3.1. This result shows that ETFB promotes the formation of a low-resistance interfacial layer between electrode and electrolyte and the ETFB-derived CEI and SEI preserves the performances of the NCM/graphite full cell. Compared to the VC-containing cell, the full cell cycled in the baseline electrolyte at 45 °C showed a relatively low interfacial resistance. This may be ascribed to thermal instability of the baseline electrolyte-derived interfacial layer. The fragile and non-uniform baseline electrolyte-derived interfacial layer is thought to be partially detached from the electrode surface and dissolved into the electrolyte during repeated cycling at 45 °C. The loss of the resistive baseline electrolyte-derived film on the electrode surface may reduce the interfacial resistance of the full cells.

Table 3.1 Impedance parameters obtained from the simulation of NCM/graphite full cells after 300 cycles at 25 and 45 °C. The equivalent circuit, which was used to fit the impedance data, is given below. R_e: electrolyte resistance, R_f: sum of SEI and CEI resistance, R_{ct}: charge transfer resistance and R_{total}: ohmic resistance of NCM/graphite full cell

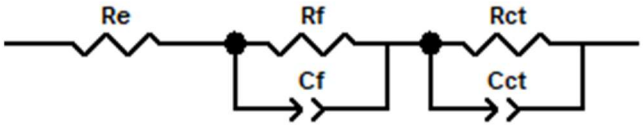

		R_e (Ω)	R_f (Ω)	R_{ct} (Ω)	Interfacial resistance (R_f+R_{ct}, Ω)	R_{Total} (Ω)
After 300 cycles at 25 °C	**Baseline**	3.0	3.7	6.3	10.0	13.0
	1% ETFB	3.1	2.0	5.4	7.4	10.5
	1% VC	2.5	1.12	10.0	11.1	13.6
After 300 cycles at 45 °C	**Baseline**	2.2	17.8	21.2	39.0	41.2
	1% ETFB	2.5	13.2	9.6	22.8	25.3
	1% VC	2.1	20.7	27.2	47.9	50.0

The undesired decomposition of the electrolyte components in high-voltage cathodes results in the formation of a resistive surface layer that hampers the electrochemical reaction kinetics and leads to the interfacial instability of the cathode. In this regard, measuring the anodic currents generated by the oxidative decomposition of the electrolyte allows determining the role of the electrolyte additives on the electrochemical properties of high-voltage cathodes. To assess the compatibility of electrolytes with and without 1% ETFB toward NCM cathodes charged up to 4.4 V vs. Li/Li^+, we carried out an electrochemical floating test for measuring the leakage current of Li/NCM half cells at a constant voltage, as shown in Figure 3.3a. Clearly, the addition of 1% ETFB resulted in reduced leakage currents at 4.4 V relative to the baseline electrolyte. Owing to the slightly higher HOMO level of ETFB relative to the EC solvent, ETFB underwent electrochemical oxidation prior to the decomposition of the EC-based electrolyte at the cathode during the initial charging process, and the ETFB-derived surface layer formed on the NCM cathode effectively blocked the electrochemical decomposition of the electrolyte generating anodic currents. It can be expected that the enhanced anodic stability of the electrolyte upon 1% ETFB addition has a marked effect on the interfacial stability of the NCM cathode upon repeated cycling and on the cycling performance of full cells based on NCM cathodes at 25 and 45 °C. Further evidence of the positive impact of the ETFB additive on the interfacial stability of the NCM cathode materials is provided in Figure 3.3b. To investigate the effect of the surface characteristics of the NCM cathodes on the dissolution of metal ions, NCM cathodes recovered from Li/NCM half cells charged up to 4.4 V in the electrolyte with and without 1% ETFB were soaked in 1.15 M $LiPF_6$ dissolved in EC/EMC/DEC and then stored at 60 °C for 5 days. The amounts of Co, Mn, and Ni metal ions in the electrolyte set in contact with the NCM cathode charged in the baseline electrolyte were 20.6, 9.7, and 129.0 ppm, respectively (Figure 3.3b). The significant dissolution of transition metal ions from the NCM cathode in a fully charged state may be explained by the mechanisms discussed in the following. Although the baseline electrolyte forms the CEI on the NCM cathode, the formed CEI layer does not maintain full surface coverage on the cathode particles at 60 °C, resulting in the exposure of the cathode surface to the electrolyte. Therefore, the electrolyte makes direct contact with the NCM cathode containing strongly oxidizing Ni^{4+} species, leading to unwanted electrolyte decomposition with loss of electrons that can in turn reduce the transition metal ions. For instance, Ni^{4+} ions in the layered structure of the fully charged NCM cathode may be reduced to Ni^{2+} by accepting electrons produced from the oxidative decomposition of the electrolyte, and the generated Ni^{2+} ions at the NCM cathode tend to combine with HF to form the resistive NiF_2 compound and dissolve into the electrolyte. It should be noted that HF is inevitably produced in $LiPF_6$-based electrolytes, because the $LiPF_6$ ion pair readily undergoes hydrolysis reactions accompanied with HF formation in the presence of water traces within the cell. In contrast, the dissolution of Co, Mn, and Ni metal ions from the NCM cathode charged in the

electrolyte with 1% ETFB was considerably lower. This finding reveals that ETFB alters the surface chemistry of the NCM cathode during the initial charging process, and the ETFB-derived CEI layer covering the NCM cathode particles has sufficient thermal stability to limit electrolyte oxidation and prevent HF-induced dissolution of metal ions from the NCM cathode during storage at 60 °C.

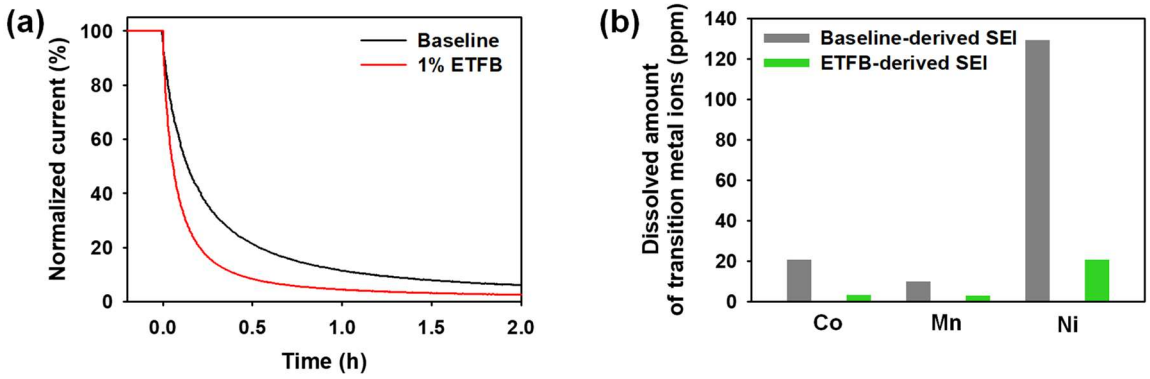

Figure 3.3 (a) Potentiostatic profiles of Li/NCM half cells with baseline and 1% ETFB-containing electrolytes measured at a constant voltage of 4.4 V vs. Li/Li^+ for 2 h. (b) ICP results showing the amounts of transition metals (Ni, Co, and Mn) dissolved from fully delithiated NCM cathodes covered by a baseline or ETFB electrolyte-derived interfacial layer after storage at 60 °C for 5 days.

Importantly, the Ni-rich cathodes suffer from the increased pH value of the cathode materials in water to around 11–12 caused by the Li-based residues (LiOH and Li_2CO_3 formed by the reaction of Li_2O with moisture and CO_2 in air), which also lead to issues such as the formation of composite gels in the NMP solvent. The NCM cathode used in this study exhibited larger amounts of Li_2CO_3 (3600 ppm) and LiOH (3000 ppm) compared to $LiCoO_2$, which is the cathode typically used in commercial Li-ion batteries (Figure 3.4a). In particular, LiOH molecules physically anchored on the NCM cathode surface may trigger the hydrolysis of $LiPF_6$ producing HF, as depicted in Figure 3.4b. The key feature in this process is the reaction between PF_5 produced from $LiPF_6$ decomposition and LiOH, to form HF in the vicinity of primary NCM cathode particles, which promotes the dissolution of transition metal ions from the cathode. The highly reactive OPF_3 species may undergo further hydrolysis with water traces in the cell to form additional HF and acidic compounds (HPO_2F_2). The NiF_2 formed by the reaction between HF and Ni^{2+} leads to a reduction in the number of energy storage sites and a corresponding capacity loss of the cathode. The reactivity of $LiPF_6$ with LiOH was explored by measuring the ^{19}F NMR spectra of the electrolytes with and without LiOH after storage at 60 °C for 3 days. The ^{19}F NMR spectra of the electrolytes before storage show two pronounced doublet peaks at -71.8/-73.1 ppm, corresponding to the PF_6^- anion, and -82.1/-83.7 ppm, attributed to the $PO_2F_2^-$ anion (Figure 3.4c-f). The appearance of the $PO_2F_2^-$ peak indicates that the hydrolysis reaction of $LiPF_6$ shown in Figure 3.4g occurs at room temperature. The baseline electrolyte without LiOH underwent mild hydrolysis to generate $PO_2F_2^-$ and did not produce PO_3F^{2-}, even after storage at 60 °C for 3 days. Surprisingly, a doublet peak near -75 ppm, which can be attributed to PO_3F^{2-}, appeared when 1% LiOH was present in the baseline electrolyte. In addition, the ^{19}F NMR spectrum of the baseline electrolyte with 1% LiOH (Figure 3.4e and f) exhibited the characteristic resonance of HF at -192.3 ppm. This result reveals the occurrence of a parasitic reaction between LiOH and $LiPF_6$, generating HF, HPO_2F_2, and H_2PO_3F, as shown in Figure 3.4g. Therefore, it is clear that the undesirable and uncontrollable transformations of the NCM particles promoted by LiOH are suppressed by the ETFB-derived protective surface film, which prevents the direct contact between electrolyte and lithium residues on the cathode surface, so that the dissolution of transition metal ions is effectively reduced.

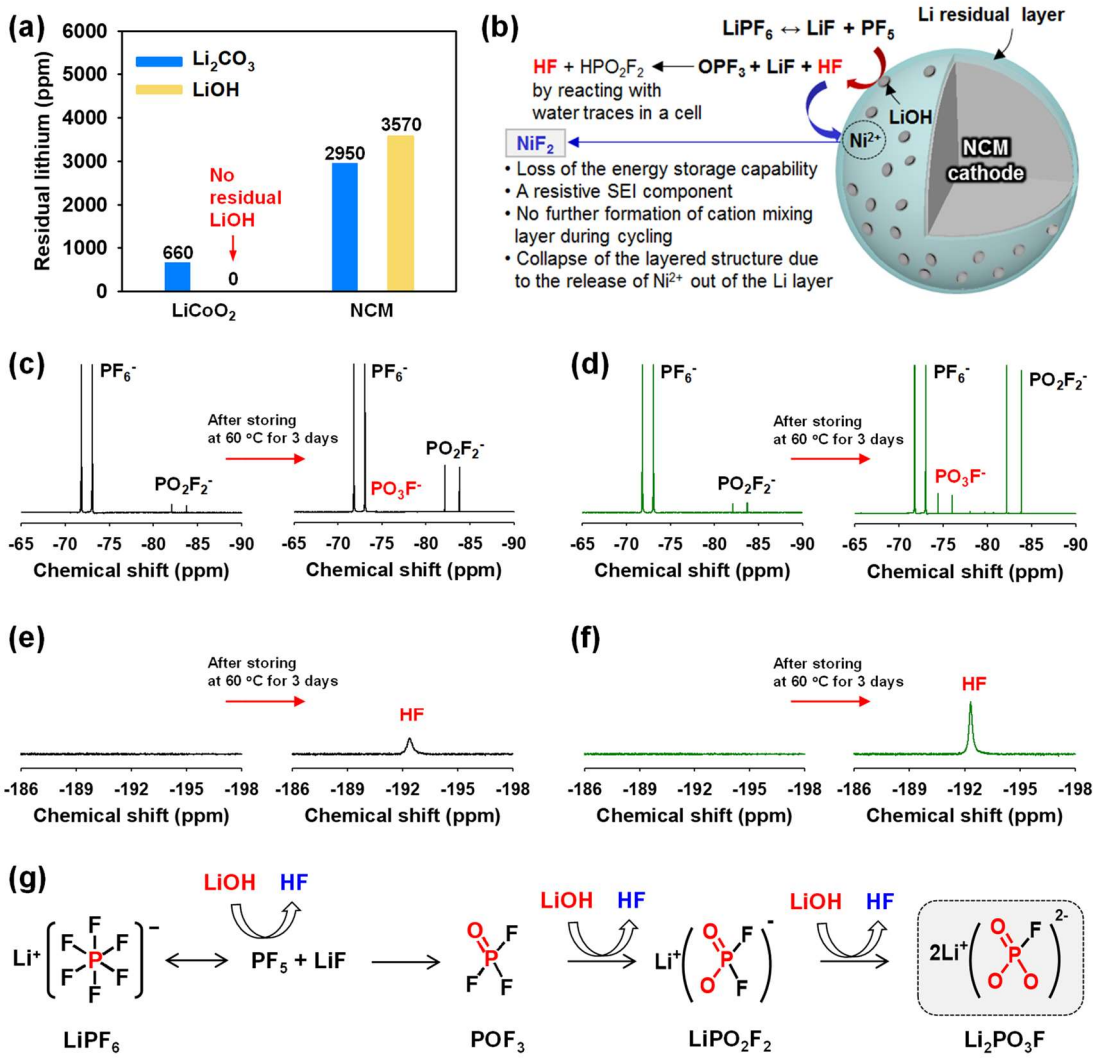

Figure 3.4 (a) Li_2CO_3 and LiOH contents of NCM and $LiCoO_2$ cathode powders. (b) Possible formation mechanisms of HF and NiF_2 triggered by the reaction of LiOH with PF_5 generated by $LiPF_6$ decomposition. ^{19}F NMR spectra (564 MHz, deuterated solvent, THF-D_8) of baseline electrolyte without (c) and (e) and with (d) and (f) 1% LiOH, before and after storage at 60 °C for 3 days. (g) Hydrolysis reactions of $LiPF_6$ promoted by LiOH.

Besides the issues associated with the lithium residues, the poor mechanical integrity of primary NCM particles forming secondary particles upon repeated charge-discharge cycles should also be addressed. The intergranular cracking of Ni-rich layered cathodes, considered as one of the main causes of their poor long-term cycling performance, was investigated by examining the cross-sectional SEM images of cycled NCM cathodes. Severe intergranular cracking occurred within secondary NCM particles retrieved from full cells cycled in the baseline electrolyte during 300 cycles at 25 and 45 °C (marked as yellow arrows in Figure 3.5a and c. This probably occurs because the non-uniform CEI layer formed by decomposition of the baseline electrolyte at the NCM cathode is electrochemically and thermally unstable and undergoes significant changes in composition and structure. This effect may increase the heterogeneity of Li intercalation and deintercalation across the NCM particle surfaces. Microcracking, resulting in a reduced connectivity of primary particle grains within the secondary NCM particles, was clearly observed on the surface of the secondary particles (Figure 3.5g and h). Notably, the intergranular cracking inside secondary NCM particles was more severe at higher temperature (45 °C). This finding demonstrates that the baseline electrolyte-derived CEI is vulnerable not only to the anisotropic strain induced by non-uniform Li intercalation and deintercalation, but also to high temperatures. The damaged CEI does not protect the primary NCM cathode particles inside secondary particles from HF attack, leading to considerable dissolution of metal ions into the electrolyte, as illustrated in Figure 3.5e. In addition, the electrolyte components decompose at the cathode surfaces exposed via intragranular cracking of secondary NCM cathode particles, and the electrolyte decomposition byproducts are accumulated inside the secondary particles. These byproducts, formed by side reactions at grain boundaries, result in poor electrical contact between the primary particles and lead to capacity and power degradation of NCM cathodes.[113] The marked mechanical deterioration of the NCM cathode is associated with the capacity fading of NCM/graphite full cells containing the baseline electrolyte, as shown in Figure 3.2a and b. In contrast, no significant intergranular cracking within the secondary NCM cathode particles was observed when the ETFB additive was used (Figure 3.5b and d), and the surface morphology of densely aggregated secondary NCM particles was preserved even after 300 cycles at 25 °C (Figure 3.5i and j). The superior mechanical integrity of the NCM cathode achieved with the ETFB-added electrolyte can be explained by the uniform coverage of the ETFB-derived CEI on the NCM cathode particles. As schematically illustrated in Figure 3.5f, the ETFB-derived CEI served as an efficient protective film to ensure homogeneous Li intercalation and deintercalation across the NCM cathode surfaces upon repeated cycling. Manthiram et al. reported that the formation of microcracks between primary particles within a Ni-rich cathode ($LiNi_{0.9}Co_{0.05}Mn_{0.05}O_2$) was due to the detrimental lattice contraction and/or expansion arising from the rhombohedral H2→H3 phase transition during cycling; the severe

anisotropic strain induced by high-voltage cycling exacerbates the fragmentation of the primary particles and the generation of microcracks between primary particles.[96]

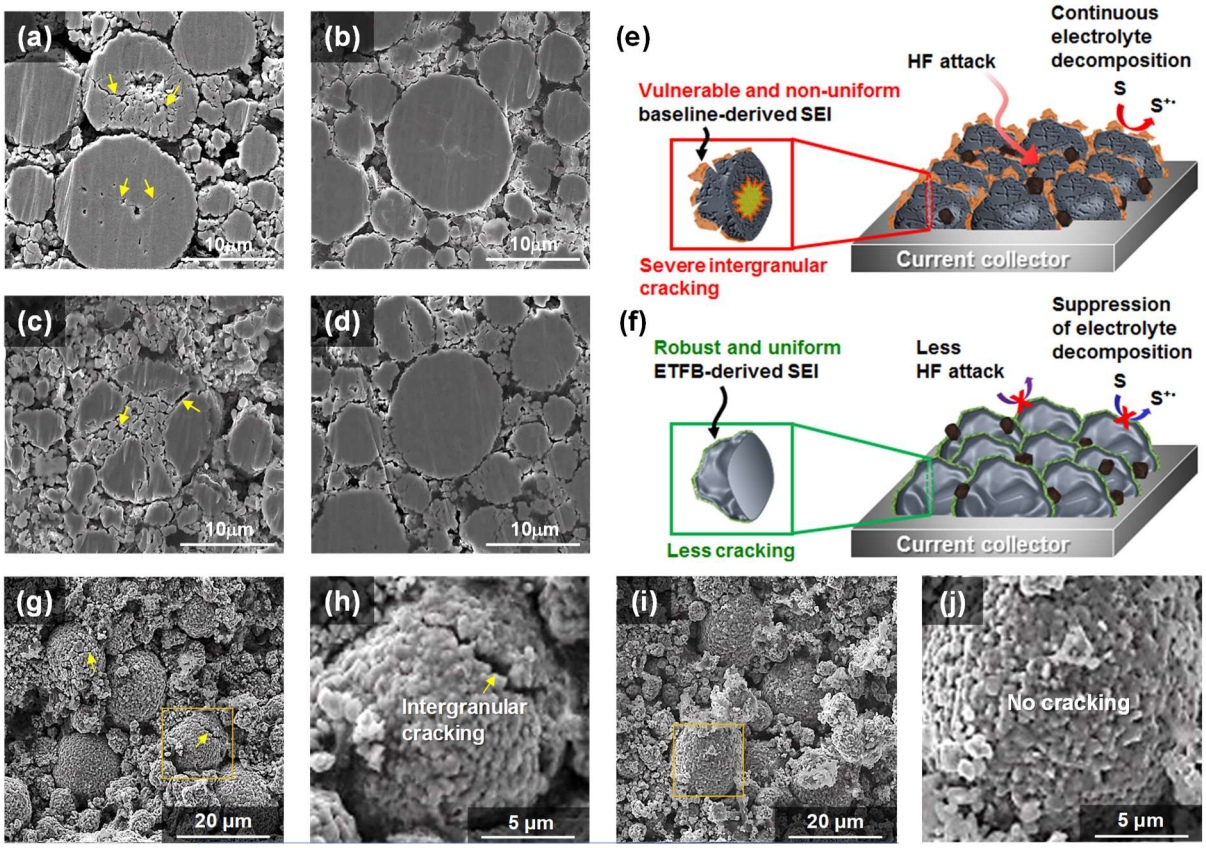

Figure 3.5 Cross-sectional SEM images of NCM cathodes retrieved from NCM/graphite full cells with (a) baseline and (b) 1% ETFB-containing electrolytes after 300 cycles at 25 °C, and (c) baseline and (d) 1% ETFB-containing electrolytes after 300 cycles at 45 °C. Schematic illustration of the functions of (e) baseline electrolyte-derived SEI and (f) ETFB-derived SEI. Top view of NCM cathodes retrieved from NCM/graphite full cells with (g) baseline and (i) 1% ETFB-containing electrolytes after 300 cycles at 25 °C. The yellow arrows highlight intergranular cracking in NCM secondary particles. The (h) and (j) panels show magnified images corresponding to the orange boxes in (g) and (i), respectively.

To further understand the origin of intergranular cracking in the NCM cathode, the potential of the cathode in a full cell configuration was monitored using a three-electrode pouch full cell with a NCM cathode, a graphite anode, and a Li reference electrode. The charge and discharge voltage profiles of the NCM cathode and graphite anode during 300 cycles at 25 °C in a three-electrode pouch full cell containing the baseline electrolyte are shown in Figure 3.6a and b, respectively. The figures clearly highlight continuous changes in the charge and discharge voltages of both electrodes. This indicates that the baseline electrolyte does not form a stable interface between the electrode and the electrolyte during short-term cycling; hence, the voltages of both electrodes show a large capacity fading during charge-discharge cycling. Relatively stable charge and discharge voltage profiles were achieved for both the NCM cathode and graphite anode in the ETFB-added electrolyte (Figure 3.6c and d). This can be mainly ascribed to the stable interface formed by ETFB. Another interesting effect is the significant difference in the end-of-charge voltages of both electrodes, depending on the electrolyte. The end-of-charge voltages of NCM cathodes and graphite anodes determined by a Li metal reference electrode during cycling are important indicators of the actual charged states of both electrodes in a full cell. Significantly higher end-of-charge voltages were observed for a three-electrode pouch full cell containing the baseline electrolyte over 200 cycles, compared to the 1% ETFB electrolyte, as shown in Figure 3.6e and f. Since high voltages cause side reactions of the electrolyte and lead to high delithiation of the NCM cathode, electrochemical degradation of full cells with the NCM cathode and severe microcracking in secondary NCM particles are unavoidable with the baseline electrolyte. Importantly, the ETFB additive attained stable charge-discharge voltages of the graphite anode upon repeated cycling in a full cell, as well as lower end-of-charge voltages, indicating that the desired lithiation state was maintained (Figure 3.6d). This finding reveals that the ETFB additive forms a suitable SEI, capable of stabilizing the interface between graphite and electrolyte, and allowing reversible lithiation and delithiation of the graphite anode without generating large overpotentials.

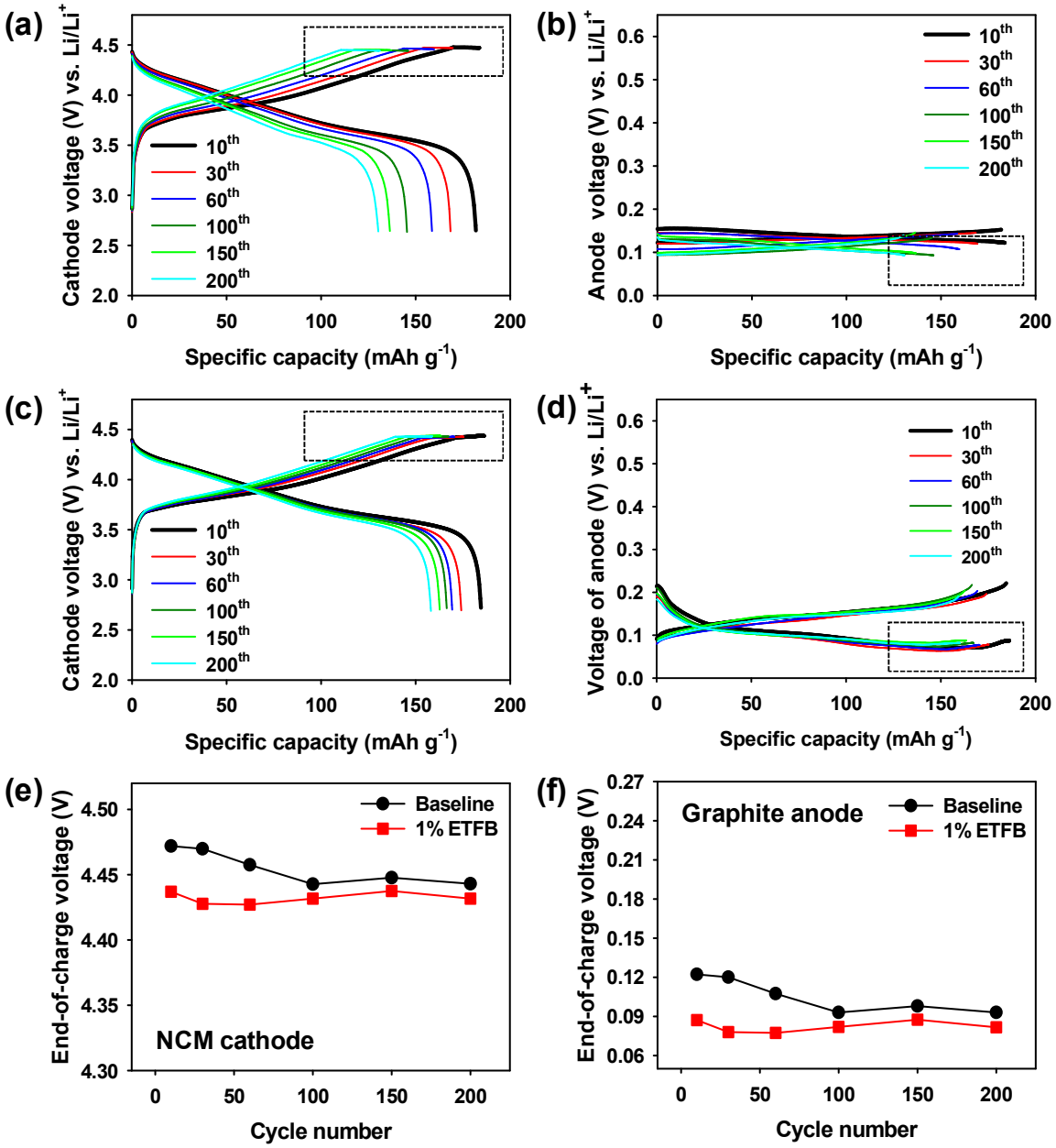

Figure 3.6 Charge and discharge voltage profiles of NCM cathodes vs. Li/Li^+ in three-electrode pouch full cells based on NCM/Li/graphite (a) without and (c) with 1% ETFB-added electrolyte. Charge and discharge voltage profiles of graphite anodes vs. Li/Li^+ with (b) baseline and (d) 1% ETFB-added electrolytes during cycling at 25 °C. The black dashed boxes show the voltages of the NCM cathode and graphite anode in the three-electrode pouch full cells at the end of the charge process. End-of-charge voltages of (e) NCM cathode and (f) graphite anode vs. Li/Li^+.

The cycling properties of three-electrode pouch full cells with and without 1% ETFB were consistent with the performance measured with coin-type full cells (Figure 3.2 and 7).

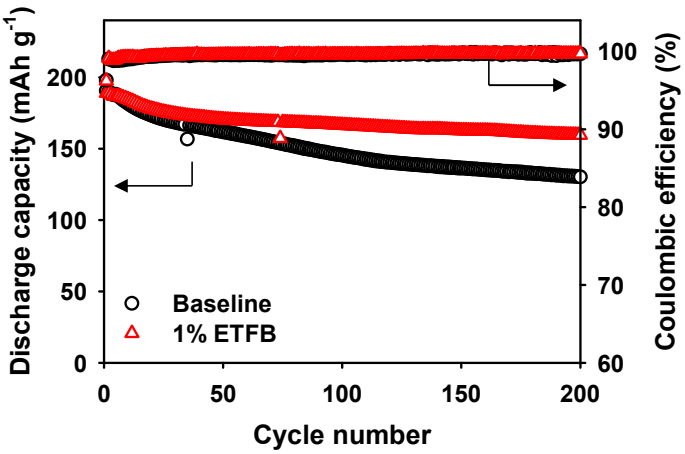

Figure 3.7 Cycling performance of three-electrode pouch full cells based on NCM/Li/graphite with and without 1% ETFB-added electrolyte at C/2 rate and 25 °C.

The effect of ETFB on the interface structure of NCM cathodes and graphite anodes was confirmed by ex situ XPS measurements. The XPS spectra of the NCM cathode surface showed distinct F 1s core level peaks, assigned to the C-F bond of the PVDF binder, the P-F moiety of decomposition byproducts of the $LiPF_6$ salt, and LiF. The intensity of the NiF_2 peak at 685.6 eV after precycling in the baseline electrolyte was significantly higher compared to that measured in the ETFB-containing electrolyte (Figure 3.8a and b). The appearance of a more pronounced NiF_2 peak for the baseline electrolyte is due to the corresponding decrease in the coverage of NCM particles with formation of a non-uniform CEI on the cathode, whose surface becomes more accessible to HF to form NiF_2 according to the $2HF\ (g) + Ni^{2+}\ (l) \rightarrow NiF_2\ (s) + H_2\ (g)$ reaction. HF is unavoidably generated by hydrolysis of $LiPF_6$ in presence of water traces and by PF_5 hydrolysis ($LiOH\ (s) + PF_5\ (g) \rightarrow HF\ (g) + LiF\ (s) + POF_3\ (s)$) promoted by LiOH on the cathode surface. The intensity of the P 2p core level peaks corresponding to Li_xPF_y, $Li_xPO_yF_z$, and phosphate (P-O) was considerably reduced for the NCM cathode containing 1% ETFB compared to the baseline electrolyte, as shown in Figure 3.8c and d. This reflects the protection of the ETFB-derived CEI film on the cathode, which prevents its direct contact with $LiPF_6$, thus suppressing $LiPF_6$ decomposition. The comparison of the C 1s core level peaks of NCM cathodes precycled in the electrolyte with and without ETFB confirms the formation of the ETFB-derived CEI on the cathode (Figure 3.8e and f). A peak attributable to the CF_3 moiety was observed around 292 eV in the C 1s core level spectrum of the NCM cathode precycled with the ETFB-added electrolyte. The appearance of this peak and the increased relative fraction of the $-CO_2-$ peak in the C 1s core level spectrum of Figure 3.8f provide clear evidence that the oxidative decomposition of ETFB contributes to modify the interface structure of the NCM cathode. Figure 3.9 shows the F 1s, P 2p, and C 1s XPS spectra of graphite anodes retrieved from NCM/graphite full cells with and without 1% ETFB after precycling. Although the peak intensity associated with $LiPF_6$ byproducts ($Li_xPO_yF_z$ and phosphate (P-O)) was reduced, the LiF peak intensity on the graphite anode showed a slight increase (Figure 3.9a-d). This suggests that the fluorine atoms of the CF_3 moiety of ETFB contribute to LiF generation under a strongly reducing environment, as indicated by low voltages (near 0 V vs. Li/Li^+). Besides peaks attributed to three types of carbon (CO_2, C-O-C, and C-H), ETFB led to the appearance of a new peak around 290.6 eV in the C 1s XPS spectra, which was not observed in the baseline-derived SEI on the graphite anode (Figure 3.9e and f).

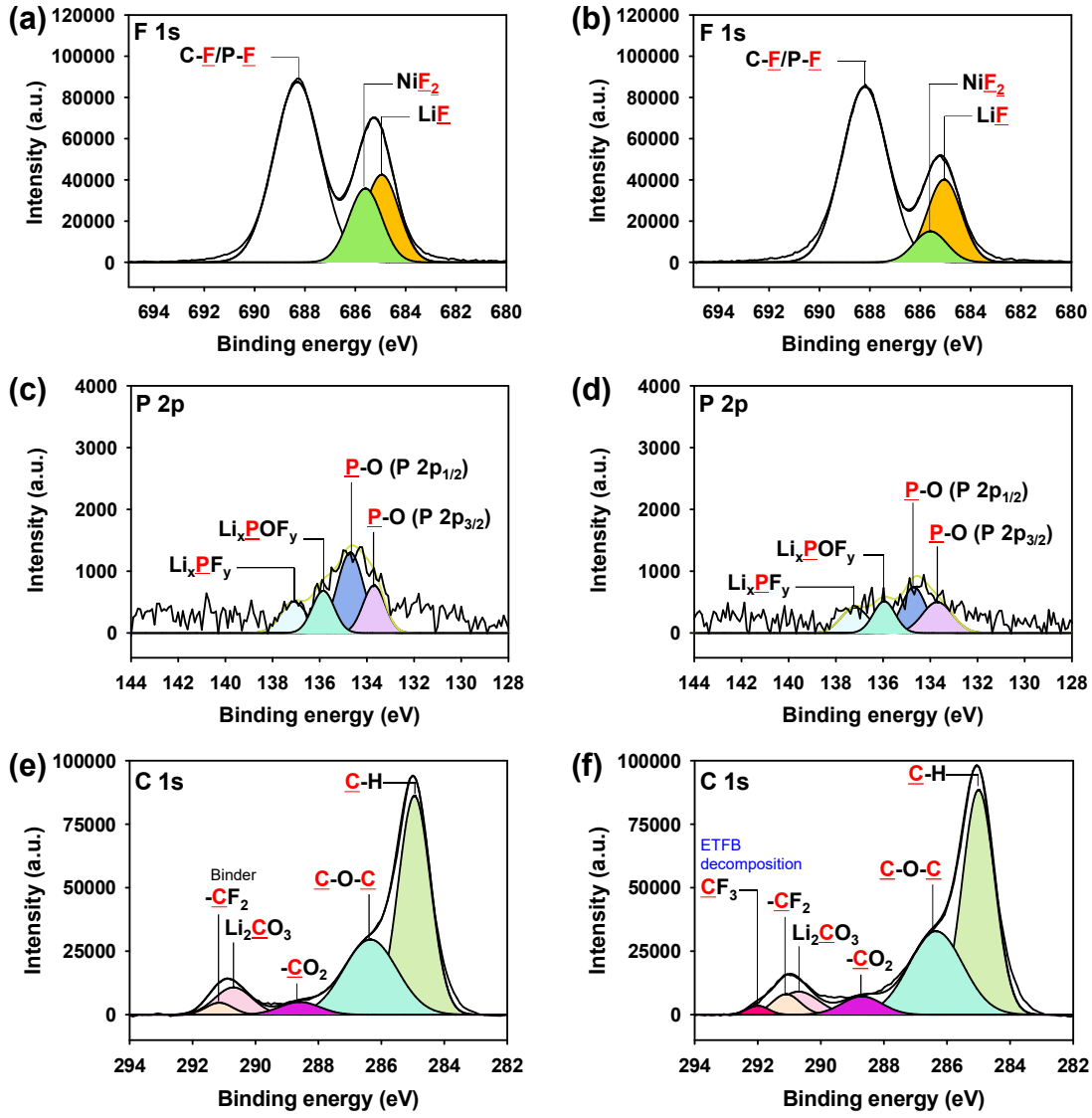

Figure 3.8 F 1s, P 2p, and C 1s XPS spectra of NCM cathodes of NCM/graphite full cells with baseline ((a), (c), and (e)) and 1% ETFB-containing ((b), (d), and (f)) electrolytes after precycling

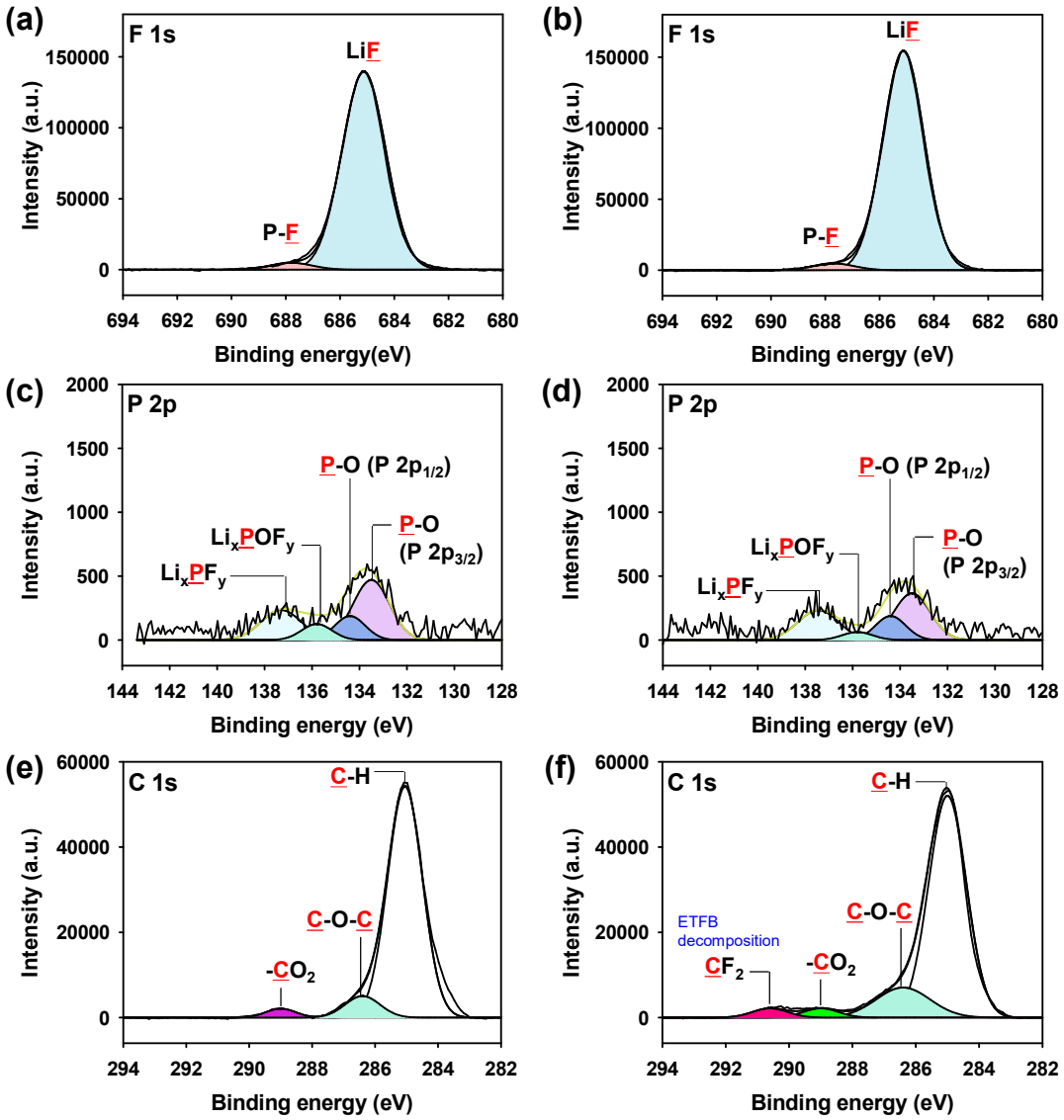

Figure 3.9 F 1s, P 2p, and C 1s XPS spectra of graphite anodes of NCM/graphite full cells with baseline ((a), (c), and (e)) and 1% ETFB-containing ((b), (d), and (f)) electrolytes after precycling.

This new peak can be assigned to carbon bonded to fluorine (-CF_2-) moieties produced by ETFB reduction. Based on the XPS results, the possible mechanisms of ETFB decomposition to form the CEI on the NCM cathode and SEI on the graphite anode are illustrated in Figure 3.10. The reductive decomposition of ETFB at the graphite anode likely proceeds according to two possible reaction routes, including the decomposition of carbon radical (CF_3-CH_2-CH_2-Ċ=O) and carboxylate (CF_3-CH_2-CH_2-COO^-) species that attack the C-1 position of the EC molecule.[114-118] CF_3-CH_2-CH_2-Ċ=O (via cleavage path I in the ETFB reduction scheme of Figure 3.10a) and CF_3-CH_2-CH_2-COO^- (via cleavage path II) may undergo co-decomposition with the EC molecule and further decomposition to form (-CF_2-)-containing polymeric compounds and LiF, as shown in Figure 3.10a. In addition to the reductive decomposition, two possible mechanisms for ETFB oxidation on the NCM cathode surface are proposed in Figure 3.10b.[119-120] The CF_3-CH_2-ĊH_2 radical species produced via cleavage path III in the ETFB oxidation scheme may decompose by interacting with the EC molecule and induce the formation of CF_3-containing compounds on the NCM cathode. Another CF_3-CH_2-CH_2-$C{\equiv}O^+$ intermediate, generated via cleavage path IV, may lose an electron and react with the EC molecule to form CF_3-CH_2-CH_2-CO_2^-, with evolution of C_2H_4 and CO_2. Unlike the ETFB reduction mechanism, it is plausible that the oxidation of ETFB at the NCM cathode does not generate LiF, because no increase in LiF peak intensity was observed in the F 1s core level spectra of the NCM cathode precycled in ETFB-added electrolyte. According to the XPS results, ETFB participates in the CEI formation on the NCM cathode and simultaneously controls the interface structure at the graphite anode surface.

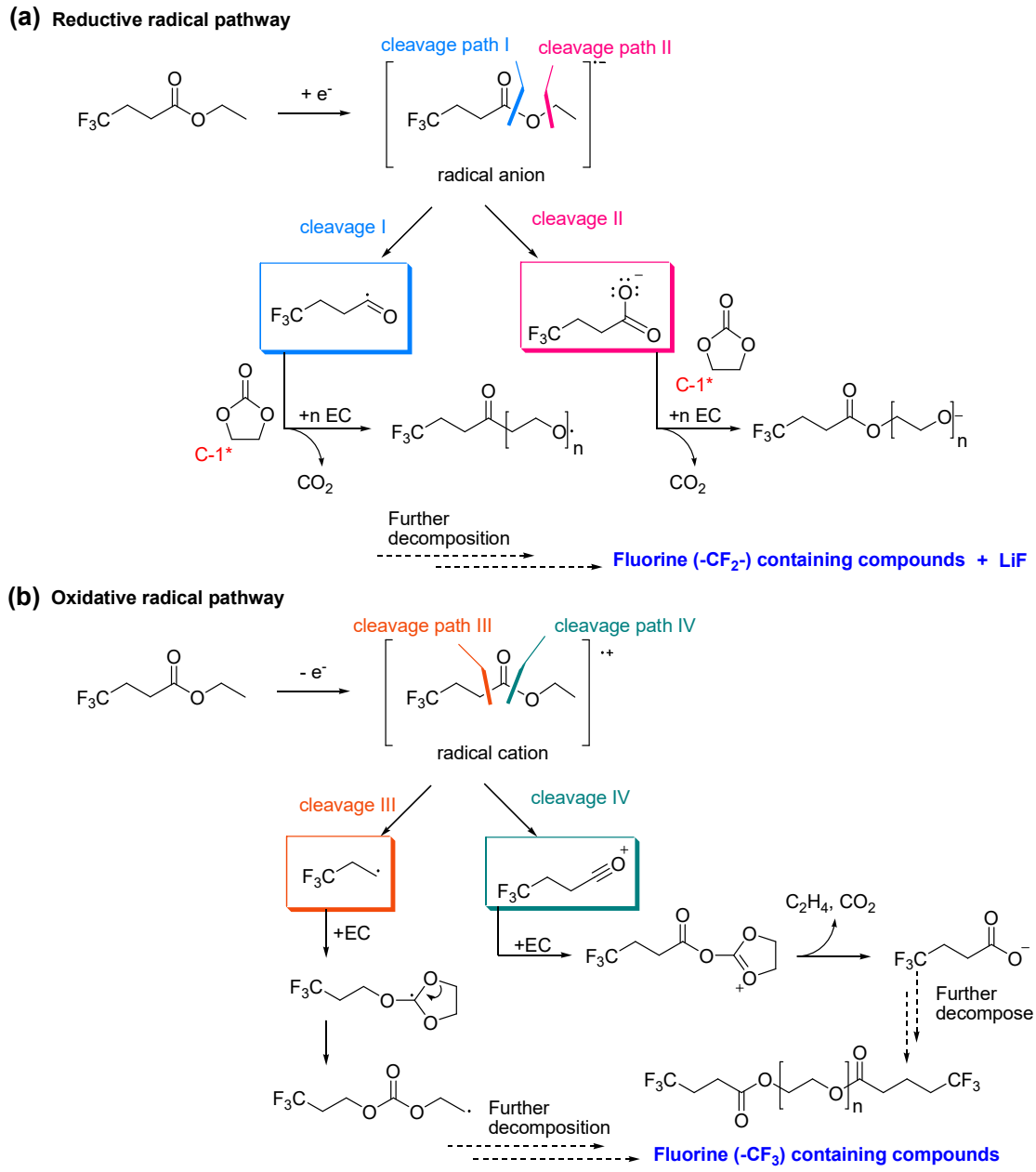

Figure. 3.10 Possible mechanisms for the oxidation and reduction of ETFB, modifying the interface structure of the NCM cathode and graphite anode.

Figure 3.11 shows the high-temperature storage performance of fully charged NCM/graphite full cells with and without 1% ETFB. The thermal stabilities of the baseline- and ETFB-derived interfacial layer protecting the electrodes were compared by monitoring the open circuit voltage (OCV) drop and the capacity retention of full cells during storage at 60 °C. The ability to suppress the OCV drop, indicating self-discharge of fully charged full cells, was found to be higher for the ETFB-containing electrolyte compared with the baseline one. In addition, the full cell with 1% ETFB delivered a discharge capacity of 161 mAh g^{-1}, much higher than that (139 mAh g^{-1}) of cells containing the baseline electrolyte, as well as a greatly improved capacity retention rate of 83.0%, as shown in Figure 3.11b. Along with the thermal instability of the SEI that consumes Li ions at the graphite anode, capacity loss may also be due to the cathodic deposits of dissolved transition metal ions from the NCM cathode during storage at 60 °C. The evaluation of the capacity of full cells after storage for 20 days at 60 °C allows measuring the recovery capability of the battery from high-temperature storage tests. As shown in Figure 3.11c, more than 81% of the lost capacity (33 mAh g^{-1}) was recovered in the NCM/graphite full cell with 1% ETFB. In comparison, the full cell containing the baseline electrolyte recovered only 60% of the lost capacity during storage for 20 days at 60 °C. Li ions, stored in the graphite anode as electrical energy, can be removed by re-lithiation into the cathode and irreversible parasitic reactions at the anode. The lower capacity recovery of full cells containing the baseline electrolyte reveals that the baseline electrolyte-derived SEI does not represent a thermally stable interface layer and results in side reactions severely consuming Li ions at the graphite anode. Figure 3.11d provides direct evidence of the positive impact of ETFB on the conservation of the lithiation degree of the graphite anode in a full cell at 60 °C. The XRD patterns of lithiated graphite anodes exhibited two graphite phases, LiC_6 and LiC_{12}, corresponding to the peaks at 24.1° and 25.3°, respectively. A more significant decrease in the peak intensity corresponding to LiC_6 was observed for the NCM/graphite full cell containing the baseline electrolyte, stored at 60 °C. The increased and decreased intensities of the LiC_{12} and LiC_6 peaks, respectively, indicate delithiation of the charged graphite anode. Most importantly, ETFB effectively maintained the lithiation degree of the charged graphite anode (Figure 3.11d). These results confirm that the ETFB-derived interfacial layer possesses sufficient thermally stability to preserve the lithiation degree of the graphite anode and prevent the dissolution of transition metal ions from the NCM cathode at 60 °C.

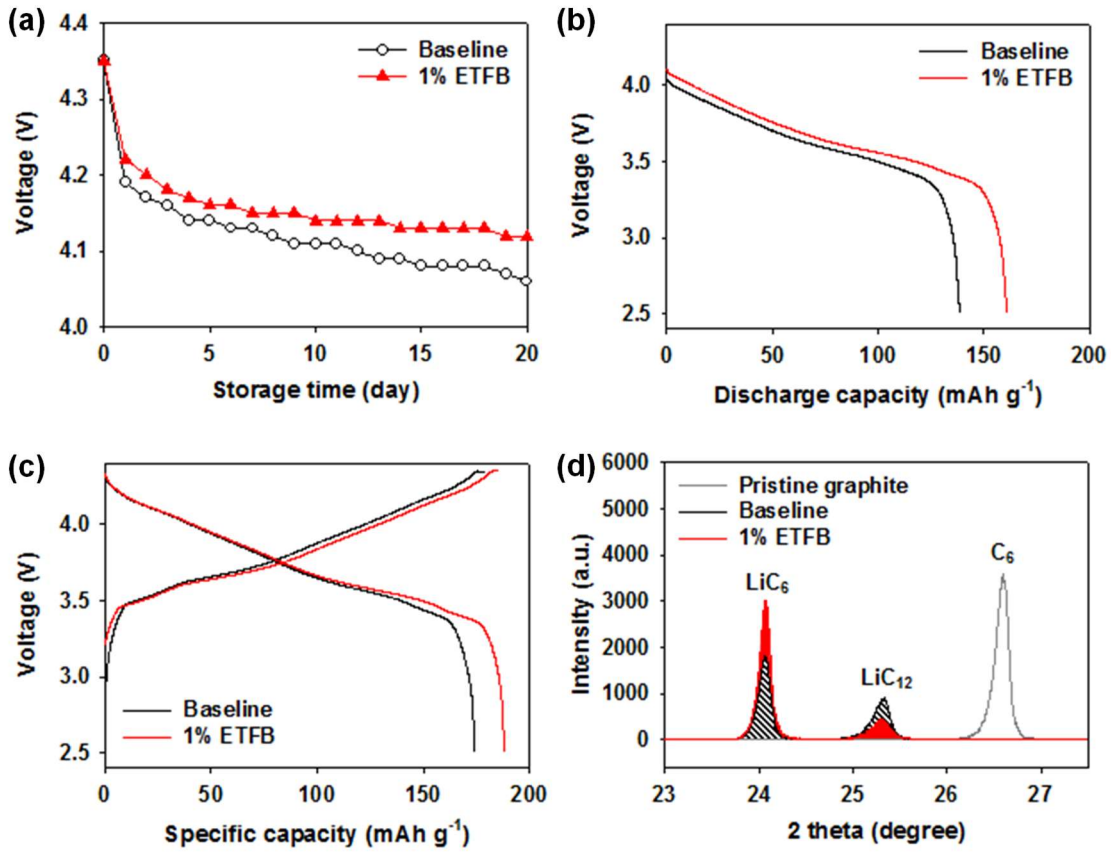

Figure 3.11 High-temperature storage performance of NCM/graphite full cells with and without 1% ETFB during storage for 20 days at 60 °C: (a) OCV variation, (b) capacity retention, and (c) capacity recovery. (d) XRD patterns of lithiated graphite anodes retrieved from NCM/graphite full cells with and without 1% ETFB after storage for 20 days at 60 °C.

3.4 Conclusion

The present work showed that the uniform CEI layer created by the ETFB additive allowed homogeneous lithiation and delithiation of NCM cathodes suppressing intergranular cracking within secondary cathode particles, avoided significant dissolution of transition metal ions from the cathode, and inhibited continuous electrolyte decomposition at the cathode upon repeated charge-discharge cycling. Cycling tests performed on NCM/graphite full cells confirmed that ETFB led to substantially improved discharge capacity retention and high Coulombic efficiency during long-term cycling at high temperature. Furthermore, our investigation revealed that the ETFB additive altered the surface chemistry of the graphite anode coupled with the NCM cathode, and the ETFB-derived SEI formed on the anode effectively reduced the unwanted self-discharge of the charged graphite anode at 60 °C. The results of this study will contribute to further improve the design of electrolyte additives that can develop interface architectures of electrodes for long-lasting batteries without sacrificing energy density by constructing a controlled and stable interfacial layer.

IV. Cyclic Amino-Silane-Based Additive Ensuring Stable Electrode-Electrolyte Interfaces in Li-Ion Batteries

4.1 Introduction

Ni-rich cathodes, $LiNi_xCo_yMn_zO_2$ ($x + y + z = 1$, $x > 0.6$), are considered possible candidates for LIBs owing to their high operating voltages and capacities, low cost, and nontoxicity. However, the successful commercialization of Ni-rich cathodes has been inhibited by their structural degradation under high operating voltages as well as parasitic reactions between electrolytes and highly reactive Ni^{4+}, which induce the oxidative decomposition of the electrolyte.[121] The formation of a protective film on the Ni-rich cathode surface through the direct coating of an artificial layer[122-123] or the *in situ* generation of a cathode–electrolyte interphase (CEI) by electrolyte additives [124-126] has been explored as a solution to the problem of interfacial instability of Ni-rich cathodes. Constructing a stable CEI is considered imperative for enhancing the structural stability and electrochemical performance of Ni-rich cathodes. In addition, the stability of the electrolyte should be considered in detail. Commercial electrolytes for LIBs generally consist of 1 M lithium hexafluorophosphate ($LiPF_6$) in a mixture of cyclic and linear carbonate solvents. $LiPF_6$ has been commonly utilized as a salt, owing to its high ionic conductivity, relatively good oxidation durability, and compatibility with Al current collectors in LIBs.[127-128] However, $LiPF_6$ also has inherent negative characteristics, including a low thermal stability and a high susceptibility toward trace amounts of water, resulting in the generation of reactive acidic compounds such as PF_5 and HF. [129-131] As corrosive substances, PF_5 and HF induce solvent decomposition and degrade the structural stability of the solid–electrolyte interphase (SEI) and CEI;[132-135] these interphases are necessary to alleviate the deterioration of electrodes during repeated cycling and under harsh conditions.[136] Moreover, HF promotes transition-metal dissolution from the cathode, causing an undesirable loss of the Li storage sites responsible for the capacity of LIBs.[137] Therefore, scavenging reactive species such as PF_5 and HF is considered crucial for realizing high-performance LIBs.

It has been reported that compounds bearing a trimethylsilyl (TMS) group can effectively capture the F^- ions from HF.[138-139] Furthermore, N with a filled orbital can form a coordination complex with the strong Lewis acid PF_5, which is an intermediate that promotes the hydrolysis of $LiPF_6$ to produce acidic compounds, and it can scavenge the proton of acidic compounds (HF, HPO_2F_2, and H_2PO_3F).[140-142] In this regard, the combination of TMS and N-containing groups is regarded as a very effective molecular design for improving the stability of $LiPF_6$-based electrolytes in LIBs. Although aminosilanes (N–Si) are suitable for scavenging both HF and H_2O,[143-144] the underlying mechanisms of these processes are not fully understood.

Herein, we present 3-(trimethylsilyl)-2-oxazolidinone (TMS-ON) as an electrolyte additive for high-energy-density LIBs. The effect of TMS-ON addition on three aspects was systematically analyzed: (1)

the stability of the $LiPF_6$-based electrolyte, (2) the interfacial stabilities of the electrodes, and (3) the changes in the microstructures of the Ni-rich $LiNi_{0.7}Co_{0.15}Mn_{0.15}O_2$ (NCM) cathode upon cycling. Computational studies and nuclear magnetic resonance (NMR) measurements revealed that TMS-ON enhances the dissociation of $LiPF_6$ by the coordination of the TMS-ON carbonyl with a Li^+ ion, alleviates the hydrolysis of $LiPF_6$ by stabilizing PF_5, and scavenges HF. In addition, HF scavenging by TMS-ON was shown to produce 2-oxazolidinone (ON), which appropriately modifies the interface structures of both the NCM cathode and the graphite anode. The interfacial structures of both the cathode and anode were confirmed by X-ray photoelectron spectroscopy (XPS) and the distinctive nature of the ON-derived CEI was identified by three-dimensional (3D) visualization using time-of-flight secondary ion mass spectrometry (TOF-SIMS). High-resolution transmission electron microscopy (HR-TEM) and electron energy loss spectroscopy (EELS) clearly demonstrated that the ON-derived CEI mitigates the unwanted electrolyte decomposition at NCM cathodes and alleviates the irreversible phase transformation of NCM cathodes.

4.2 Experimental method

Electrolyte and electrodes

The baseline electrolyte consisted of 1 M $LiPF_6$ dissolved in a solvent mixture of EC, EMC, and DEC (3:4:3, vol%) with 1% VC. All solvents and the salt were purchased Soulbrain Co., Ltd. The TMS-ON- and ON-containing electrolytes were prepared by adding 0.5% TMS-ON (98%, TCI Co., Ltd.) or 0.5% ON (98%, TCI Co., Ltd.) to the baseline electrolyte. All the electrolytes were confirmed to contain less than 10 ppm of water by Karl Fischer titration (C30, Mettler Toledo).

The Ni-rich NCM cathodes were composed of 94 wt.% NCM as the active material, 3 wt.% conducting materials (2 wt.% Super C + 1 wt.% graphite), and 3 wt.% poly(vinylidene fluoride) (PVDF 6020). The thickness, specific capacity, and loading density of the cathode were 80 μm, 4.7 cm^{-2}, and 24.9 mg cm^{-2}, respectively. The graphite anodes were composed of 97.5 wt.% graphite as the active material and 2.5% wt.% binder (1.5 wt.% styrene-butadiene rubber and 1 wt.% sodium carboxymethyl cellulose). The thickness, specific capacity, and loading density of the anode were 83 μm, 5.0 mA h cm^{-2}, and 13.9 mg cm^{-2}, respectively. All the electrodes were provided by Hyundai Motor Co., Ltd.

Electrochemical measurements

The 2032 coin-type full cells consisting of a Ni-rich NCM cathode and a graphite anode were assembled in an argon-filled glove box (O_2 and H_2O < 1 ppm). Each cell contained a polyethylene (PE, SK Innovation Co., Ltd.) separator with a porosity of 38% and a thickness of 20 μm. The amount of electrolyte per coin cell was 0.062 g. Galvanostatic cycling was conducted between 3.0 and 4.35 V at 25 °C and 45 °C using a battery measurement system (WBCS 3000, WonATech Co., Ltd.). The current densities used for precycling and cycling of the full cells were 0.47 mA cm^{-2} (0.1C) and 2.35 mA cm^{-2} (0.5C), respectively. The impedances of the NCM/graphite full cells were measured by AC impedance analysis using an IVIUM frequency response analyzer over the frequency range from 0.01 Hz to 1 MHz. Fitting of the impedance spectra was conducted using ZVIEW software.

Characterization

To analyze the electrolyte decomposition reactions, the electrolytes were monitored by 600 MHz ^1H NMR spectroscopy and 564 MHz ^{19}F NMR spectroscopy (VNMRS 600, Agilent) using a coaxial-type tube. All the electrolytes were stored in PTFE tubes (BK Instrument Inc.) to prevent chemical reactions between HF and glass, and THF-d_8 (99.5%, NMR grade, BK Instruments Inc.) with 1% hexafluorobenzene (C_6F_6, 99.5%, NMR grade, Sigma-Aldrich) as an internal standard for ^{19}F NMR analysis was stored in a glass tube (NES-600, OPTIMA). ICP-OES (700-ES, Varian) was used to determine the amount of transition metal ions (Ni, Co, and Mn) in the electrolytes stored with

delithiated NCM cathodes at 45 °C for 7 days. After each electrochemical measurement, all the electrode samples were prepared in an argon-filled glove box. The retrieved electrodes were rinsed with dimethyl carbonate to remove the residual electrolyte and then dried in the glove box. To avoid contamination of the cycled electrodes with air or moisture contamination, an XPS (SIGMA PROBE, Thermo) equipped with an Al Kα (1486.6 eV) X-ray source and directly connected to the glove box was used to investigate the surface chemistry of the electrodes. All binding energies were calibrated to the C–C bond (285.0 eV). TOF-SIMS (TOF-SIMS 5, ION TOF) was used to analyze the surface chemical structure and for depth profiling. The pressure of the analysis chamber was maintained below 10^{-9} mbar. A Bi^{1+} primary ion beam (25 keV, 1 pA) in high-current mode was used for surface analysis and the typical sputtering area was 500 × 500 μm^2. Furthermore, a Cs^+ sputtering ion beam (500 eV, 22 nA) was used to scan crater areas (typically 200 × 200 μm^2) and for depth profiling (50 × 50 μm^2 measurement area). All mass spectra were acquired in negative polarity with a mass resolution of >5000. HR-TEM (JEM-2100F, JEOL) and STEM images were acquired at 300 kV to investigate the structural degradation of the Ni-rich NCM cathodes at the atomic level. EELS was used to assess the electronic structure of the Ni-rich NCM cathodes containing the valence states of transition metals. Microcracking of the secondary Ni-rich NCM particles was observed by cross-sectional scanning electron microscopy (SEM, Verios 460, FEI). The cross-sectional samples for TEM and SEM measurements were prepared using a dual-beam focused ion beam (Helios Nano Lab 450, FEI) and an ion-milling system (HITACHI IM4000, Hitachi High-Technologies), respectively.

DFT calculation

DFT calculations performed using the $DMol^3$ program were used to elucidate the effect of TMS-ON in electrolytes. The Becke three-parameter hybrid functional combined with the Lee–Yang–Parr correlation functional (B3LYP) was used for the exchange correlation energy. To describe the van der Waals interactions accurately, the long-range dispersion correction was taken into account with the semi-empirical DFT-D2 method suggested by Grimme. The spin-polarized calculation was used with version 4.4 of the double numerical plus polarization (DNP) basis set. All electron relativistic core treatments were conducted with a global orbital cutoff radius of 4.5 Å. The convergence criteria for the geometry optimization were 1.0×10^{-5} Ha for energy, 0.002 Ha $Å^{-1}$ for force, and 0.005 Å for displacement.

4.3 Results and discussion

$LiPF_6$, utilized commonly as a salt in electrolytes for LIBs, exists in several forms, including ion-paired $LiPF_6$, which is not completely dissociated by solvent molecules, and solvated Li^+ and PF_6^-. Ion-paired $LiPF_6$ is prone to autocatalytic decomposition to form LiF and PF_5, and this process is accelerated at high temperatures. As a strong Lewis acid, PF_5 is a highly reactive species that can induce the decomposition of cyclic carbonates such as ethylene carbonate (EC) and structurally damage both the CEI and SEI formed on the cathode and anode surfaces, respectively.[132-135] In addition, PF_5 reacts with water to produce highly reactive POF_3, HF, and phosphoric acid compounds (HPO_2F_2, H_2PO_3F, and H_3PO_4). Furthermore, PF_6^- formed by dissociation of $LiPF_6$ in the electrolyte reacts directly with water to produce HPO_2F_2 and HF.[145-146] HF in the electrolyte not only leaches the transition metal ions from the cathode but also causes severe damage to the CEI and SEI.[136] In this regard, inhibiting the generation of reactive species (HF and PF_5) in $LiPF_6$-based electrolytes is essential for achieving high-performance batteries (Figure 4.1).

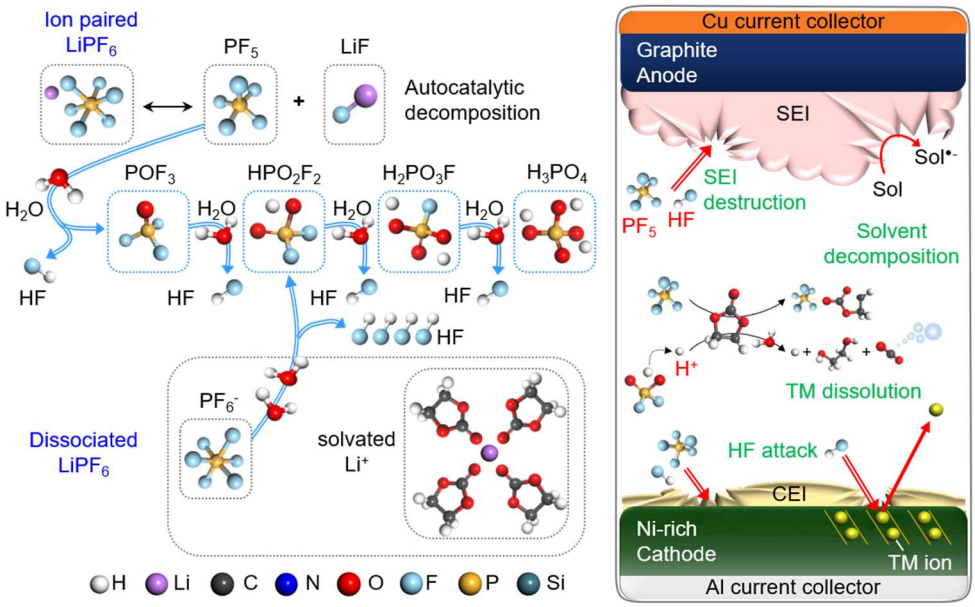

Figure 4.1 Schematic illustration of the hydrolysis of $LiPF_6$ to generate acidic compounds in the electrolyte.

TMS-ON contains an aminosilane moiety, which has a high affinity forward HF, and a polar cyclic structure that can effectively interact with a Li^+ ion, thus improving the extent of $LiPF_6$ dissociation and reducing the formation of ion-paired $LiPF_6$, which readily undergoes hydrolysis by reacting with trace water to produce acidic compounds such as HF and phosphoric acid compounds.[129-131] The Si atom in the N–Si moiety of TMS-ON can effectively take up a fluoride anion to form a pentavalent silane intermediate that subsequently produces trimethylsilyl fluoride (TMSF).[143-144] Thus, it is likely that HF in $LiPF_6$-based electrolytes can be eliminated by decomposition of TMS-ON into TMSF and ON (Figure 4.2a). To analyze the action mechanism of TMS-ON toward $LiPF_6$ in the bulk electrolyte, density functional theory (DFT) calculations were conducted. We first investigated the formation energy of the electrolyte components interacting with a Li^+ ion and found the most thermodynamically stable configurations to describe the state of the electrolyte components more accurately (Figure 4.2b). A comparison of the most stable formation energies for Li^+ ion complexation with EC, ethyl methyl carbonate (EMC), diethyl carbonate (DEC), vinylene carbonate (VC), ON, and TMS-ON revealed that the TMS-ON-Li^+ complex has the lowest energy of -0.81 eV, indicating that this is the most favorable structure. Further evidence was provided by electrospray ionization mass spectrometry (ESI-MS), which revealed various clusters including Li^+ and TMS-ON, such as Li^+(TMS-ON), Li^+(TMS-ON)(EC), and Li^+(TMS-ON)$_2$. This result clearly demonstrates that the dissociation of $LiPF_6$ is improved by the introduction of TMS-ON (Figure 4.3).

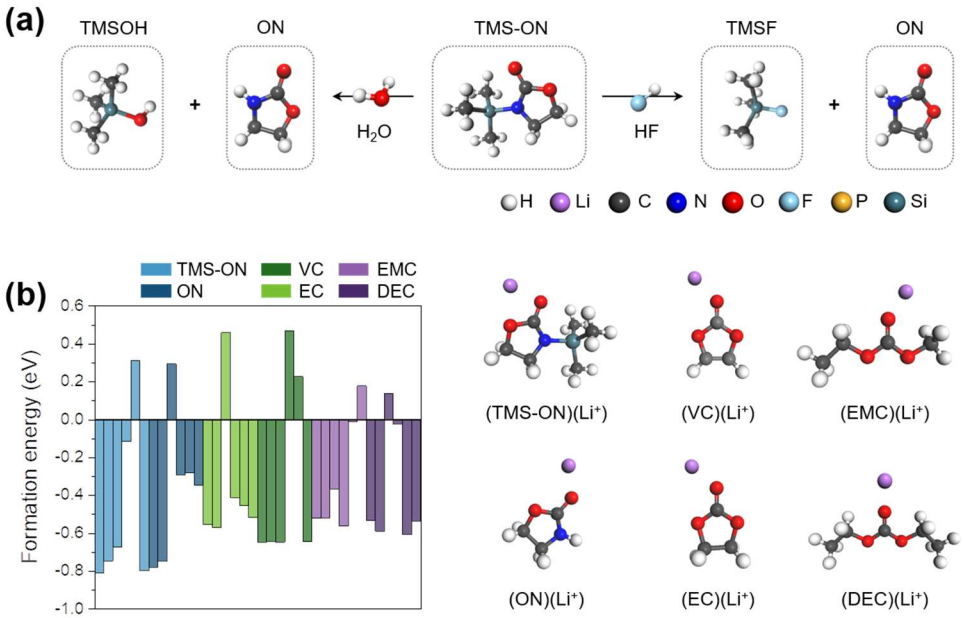

Figure 4.2 (a) HF and H_2O scavenging mechanism of TMS-ON. (b) Determination of the most stable states of TMS-ON, ON, VC, EC, EMC, and DEC coordinated with Li^+ based on the formation energies.

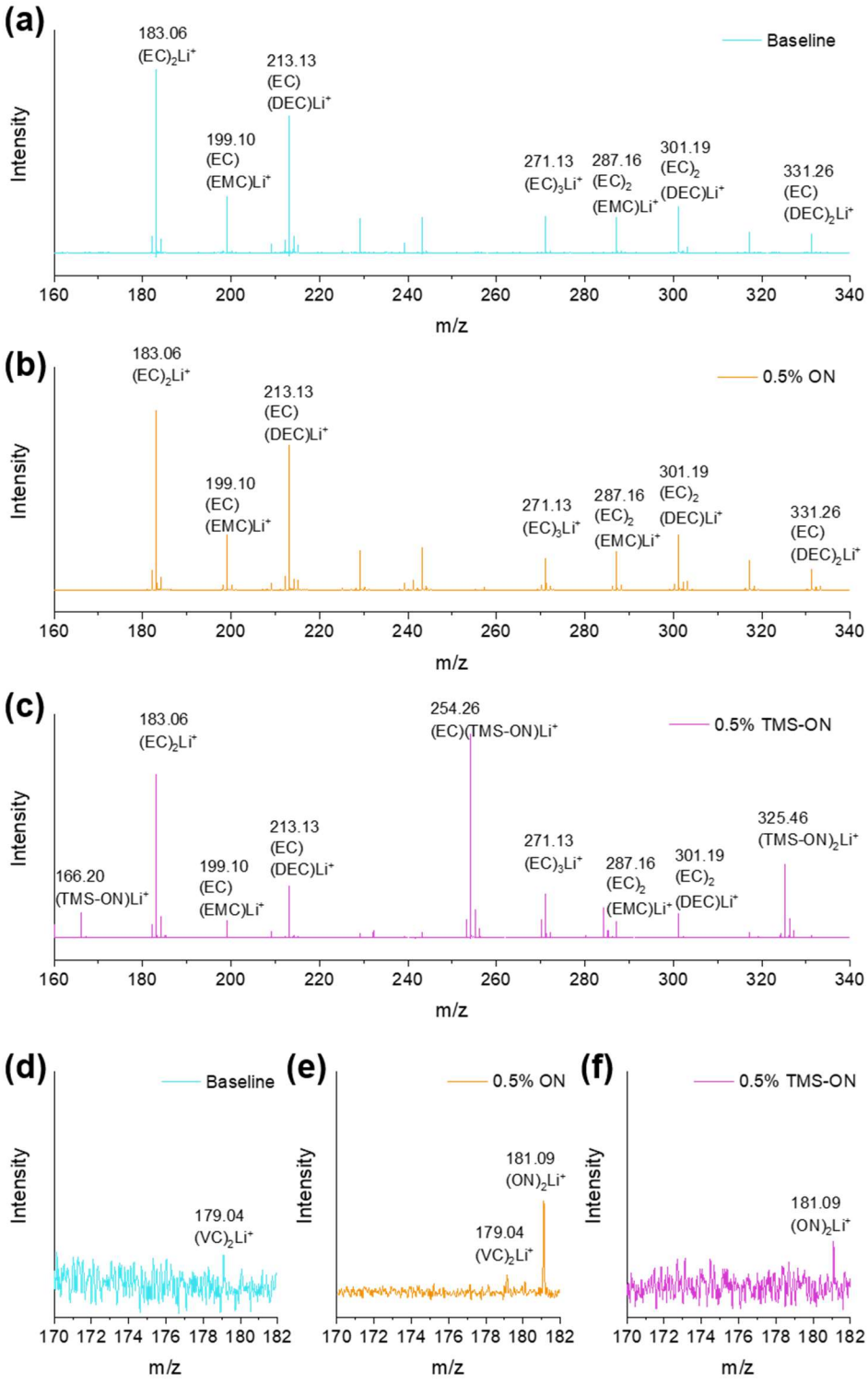

Figure 4.3 ESI-MS spectra of (a) baseline, (b) 0.5% ON, and (c) 0.5% TMS-ON electrolytes. Magnified spectra between m/z 170 and 182 for (d) baseline, (e) 0.5% ON, and (f) 0.5% T MS-ON electrolytes.

Based on the stable configurations of the complexes between Li^+ and solvents or additives in the electrolyte, the PF_5 stabilizing effects of the carbonate solvents (EC, EMC, DEC, and VC), ON, and TMS-ON were confirmed by DFT calculations (Figure 4.4a). The PF_5 binding energies of TMS-ON and ON (-1.28 and -0.73 eV, respectively) indicated that PF_5 binds more strongly to these compounds than to the carbonate solvents. This phenomenon occurs because the N atoms in TMS-ON and ON are Lewis base sites that can effectively interact with the Lewis acid PF_5. In addition, the binding distance between the N site and PF_5 for TMS-ON (1.95 Å) is shorter than that for ON (2.31 Å), which implies that TMS-ON stabilizes PF_5 more effectively owing to the electron-donating nature of the TMS functional group. To confirm the effect of PF_5 stabilization on the hydrolysis of $LiPF_6$, the reaction between PF_5 and H_2O was calculated with and without the TMS-ON-Li^+ complex (Figure 4.4b). The hydrolysis reaction of PF_5 without the TMS-ON-Li^+ complex is energetically favorable, as shown by the negative heat of reaction, whereas the hydrolysis reaction of PF_5 with the TMS-ON-Li^+ complex has a positive heat of reaction and a relatively high energy barrier. In particular, owing to the strong interaction between PF_5 and the TMS-ON-Li^+ complex, there is a higher energy barrier for adsorption of a H_2O molecule on PF_5 when TMS-ON is present (i.e., 0.54 eV with the TMS-ON-Li^+ complex and 0.10 eV without the TMS-ON-Li^+ complex). In contrast, when TMS-ON is not present, the adsorption of H_2O molecule stabilizes PF_5, resulting in a low energy barrier and a high heat of reaction.

Additionally, as shown by the reaction energy diagrams calculated for TMS-ON with HF and H_2O (Figure 4.5), both TMS-ON decomposition reactions are exothermic and energetically favorable. However, the reaction between HF and TMS-ON is dominant because it has a lower energy barrier and a higher heat of reaction than the reaction between H_2O and TMS-ON do. Therefore, TMS-ON in the electrolyte has versatile functions: (i) promoting the dissociation of $LiPF_6$ and reducing PF_5 formation, (ii) deactivating the undesirable reaction between PF_5 and H_2O that produces HF and HPO_2F_2, and (iii) scavenging H_2O and HF.

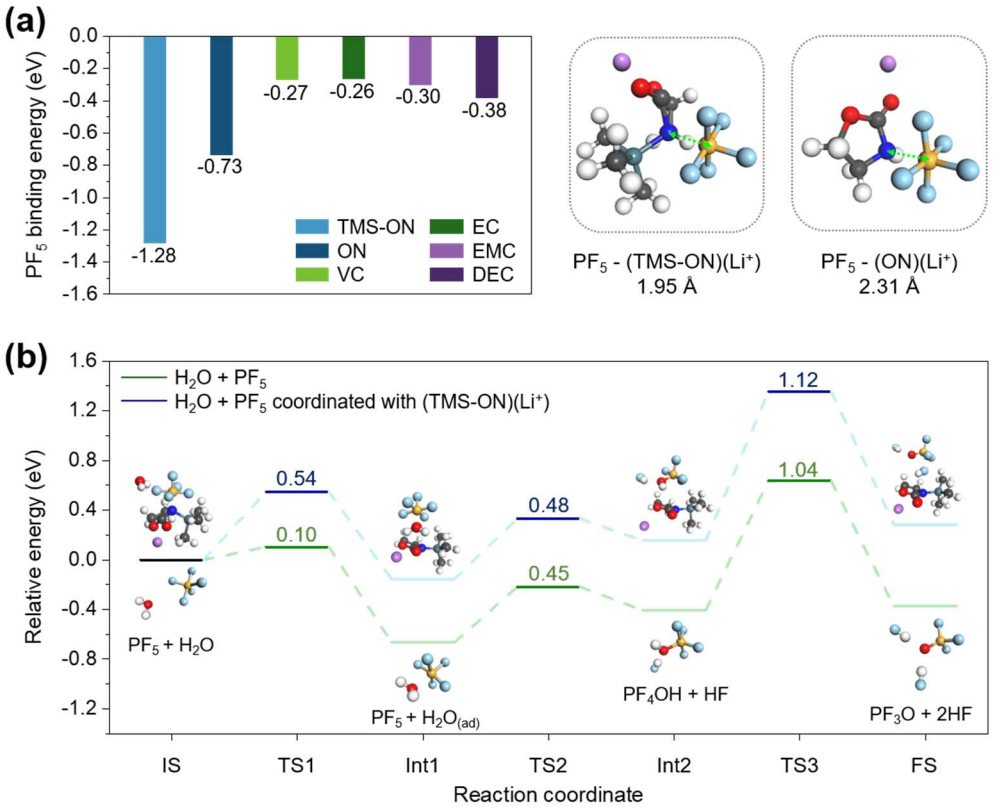

Figure 4.4 (a) Binding energies of the most thermodynamically stable configurations of PF_5 with TMS-ON, ON, VC, EC, EMC, and DEC coordinated with Li^+. (b) Reaction energy diagram for the hydrolysis of PF_5 with and without TMS-ON-Li^+.

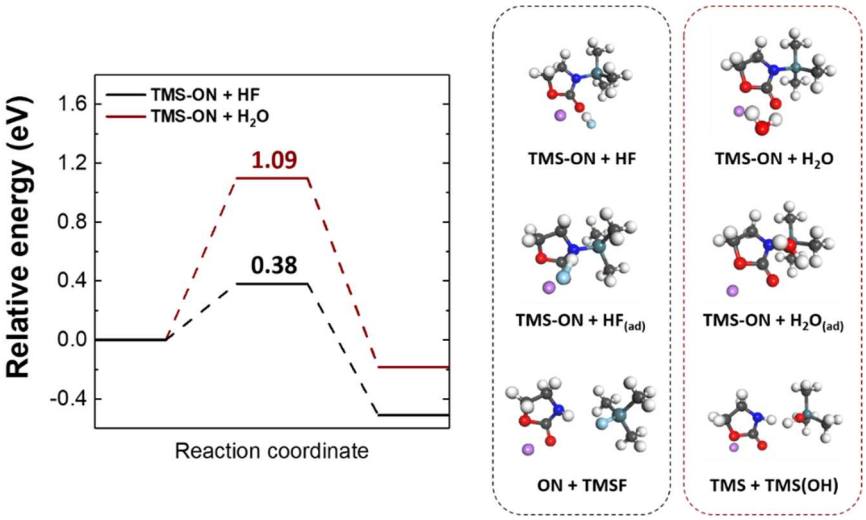

Figure 4.5 Reaction energy diagrams of TMS-ON with H_2O and HF.

To elucidate the working mechanism of TMS-ON in the electrolyte experimentally, ^{19}F NMR measurements were performed following storage of the baseline ($LiPF_6$ dissolved in a mixture of EC, EMC, and DEC without additives), 0.5% ON, and 0.5% TMS-ON electrolytes at 45 °C for 40 h. Interestingly, although POF_3 was detected in the baseline and 0.5% ON-containing electrolytes, it was not detected in the 0.5% TMS-ON-containing electrolyte (Figure 4.6).). It is likely that the transformation of PF_5 into POF_3 via the reaction with trace water in the electrolyte did not occur in the TMS-ON-containing electrolyte. From the amounts of HPO_2F_2 and HF produced, it could be inferred that the degree of $LiPF_6$ hydrolysis decreases in the order of baseline, 0.5% ON, and 0.5% TMS-ON electrolytes (Figure 4.6b and c). The concentration of HF continuously increased in the baseline electrolyte, whereas HF completely disappeared in the 0.5% TMS-ON-containing electrolyte because of the formation of TMSF by the reaction of TMS-ON with HF over time, as shown in Figure 4.6d. These results imply that TMS-ON helps resolve the problems induced by HF and PF_5.

The concentration of the acidic compounds HF and HPO_2F_2 in the electrolytes greatly affects the interfacial structure of the graphite anode. To explore the effect of TMS-ON on the SEI structure on the graphite anode, *ex situ* XPS measurements were conducted. The F 1s spectra of graphite anodes cycled with baseline and 0.5% TMS-ON electrolytes showed clear differences (Figure 4.6e and f). The baseline electrolyte with a relatively high HF concentration formed an SEI with a large fraction of LiF and NiF_2 on the graphite surface (Figure 4.6e) because LiF and NiF_2 can be formed by the reaction between HF and Li^+ (or Ni^{2+}). In particular, NiF_2 is formed because the high reactivity of the electrolyte causes severe transition-metal dissolution from the NCM cathode. For electrolytes retrieved from NCM/graphite full cells before precycling, the Ni^{2+} content of the electrolyte without TMS-ON was 6 times higher than that of the 0.5% TMS-ON-containing electrolyte (Figure 4.7). LiF, PO_xF_y, and P–F species, which were detected for the graphite anodes cycled with the baseline electrolyte, may be produced by the decomposition of $LiPF_6$ (Figure 4.6e).[147-149] $LiPF_6$ and its decomposition products, such as POF_3 and HPO_2F_2, can be reduced by accepting electrons, as shown in the following reactions (Equation 4.1-4).

$$LiPF_6 + 4Li^+ + 4e^- \rightarrow 4LiF\downarrow + Li_xPF_y\downarrow \quad (4.1)$$

$$POF_3 + 2xLi^+ + 2xe^- \rightarrow Li_xPOF_{3-x}\downarrow + xLiF\downarrow \quad (4.2)$$

$$HPO_2F_2 + 2e^- + HF \rightarrow PF_{3-n}(OH)_n + (2-n)OH^- + nF^- \ (n=1, 2) \quad (4.3)$$

$$HPO_2F_2 + 2e^- + H_2O \rightarrow PF_{3-n}(OH)_n + (3-n)OH^- + (n-1)F^- \ (n=1-3) \quad (4.4)$$

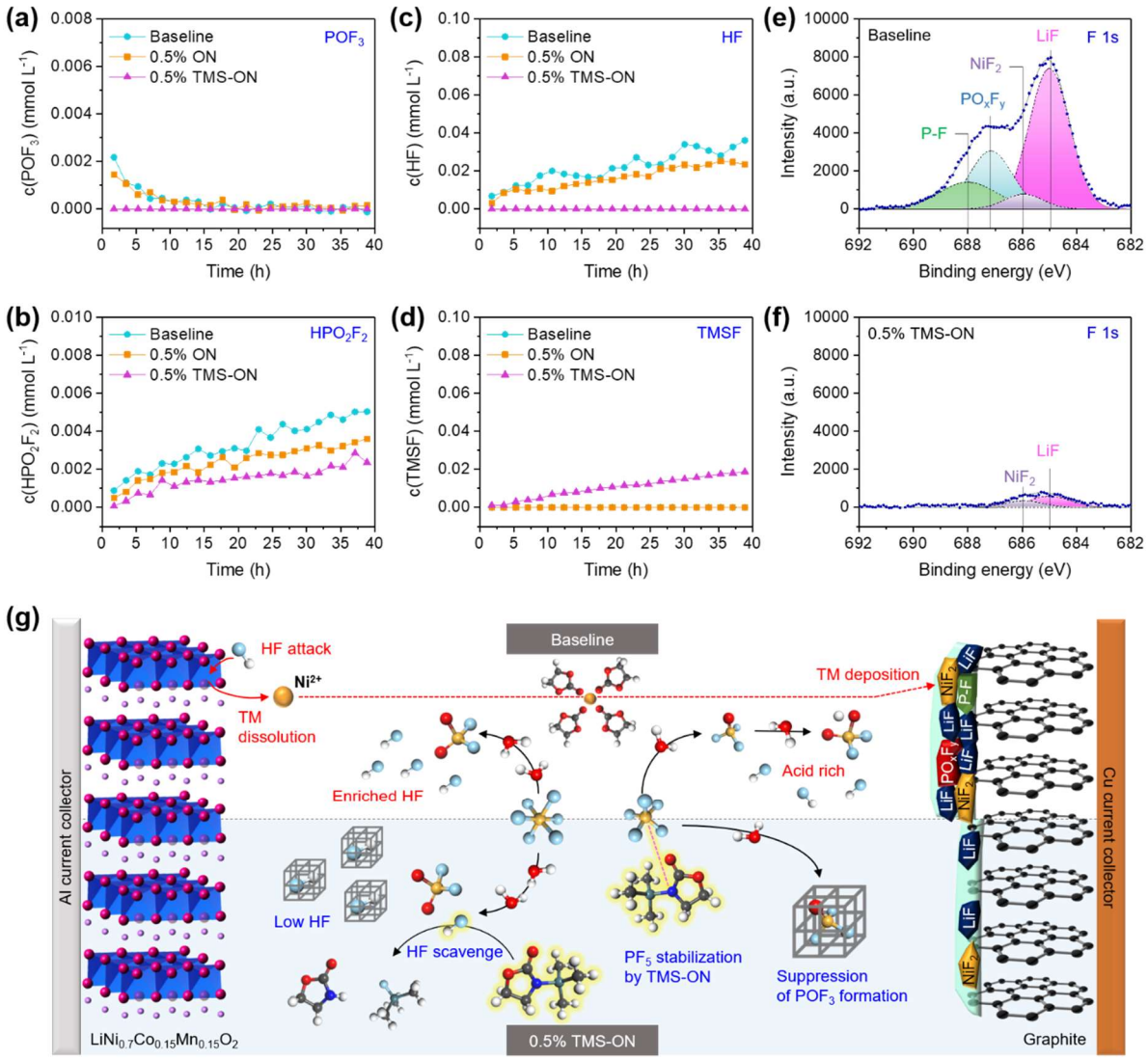

Figure 4.6 Concentrations of decomposition products in $LiPF_6$-based electrolytes obtained from kinetic ^{19}F NMR measurements of baseline, 0.5% ON, and 0.5% TMS-ON electrolytes after 40 h at 45 °C: (a) POF_3, (b) $PO_2F_2^-$, (c) HF and (d) TMSF. F 1s XPS spectra of graphite anodes retrieved from NCM/graphite full cells with (e) baseline and (f) 0.5% TMS-ON electrolytes after 3 cycles at 25°C (charge and discharge rate: 0.2C). (g) Schematic illustration of the reaction mechanism of TMS-ON in the bulk electrolyte and the modified SEI structure induced at the graphite anode by TMS-ON.

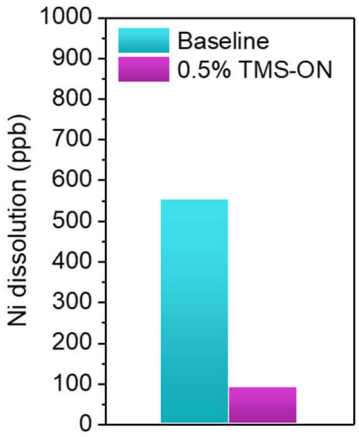

Figure 4.7 ICP-OES results for electrolytes retrieved from NCM/graphite full cells after aging (at 45 °C for 1 h and at 25 °C for 20 h).

The molecular energy levels of the electrolyte solvents (EC, EMC, and DEC), additives (VC and TMS-ON), and intermediates (ON and TMSF) interacting with Li^+ are shown in Figure 4.8a, taking into consideration that TMS-ON easily reacts with HF and decomposes into ON and TMSF. Comparing the lowest unoccupied molecular orbital (LUMO) energies, VC has the lowest energy of -1.14 eV, which might be most favorable for reductive decomposition at the graphite anode. As TMS-ON, ON, and TMSF show higher LUMO energies than the carbonate solvents (EC, DEC, and EMC), it is inferred that these compounds are unlikely to undergo reductive decomposition at the graphite anode. However, TMS-ON, ON, TMSF, and VC are likely to decompose oxidatively at the NCM cathode because of their highest occupied molecular orbital (HOMO) energies are higher than those of the carbonate solvents.

Figure 4.8b-e shows the cycle performance (rate of 0.5C) of NCM/graphite full cells with baseline and 0.5% TMS-ON-containing electrolytes at 25 and 45 °C. The NCM/graphite full cells with the 0.5% TMS-ON-containing electrolyte achieved superior cycling stability. In particular, the discharge capacity retention of the full cell with 0.5% TMS-ON was drastically improved from 52.4% to 80.4% after 400 cycles at 45 °C, delivering a high discharge capacity of 154.7 mA h g^{-1} and a high Coulombic efficiency of 99.8%. Furthermore, the ohmic polarization of the full cell with 0.5% TMS-ON was significantly reduced compared with that of the full cell with the baseline electrolyte (Figure 4.8d and e). This difference can be explained by the action mechanism of TMS-ON for stabilizing the interfacial layers of both electrodes. A lower interfacial resistance, composed of the resistance of the CEI and SEI films (R_f) and the charge-transfer resistance (R_{ct}), was observed for the NCM/graphite full cell with the 0.5% TMS-ON electrolyte after 400 cycles at 45 °C (Figure 4.8f). Notably, the use of 0.5% TMS-ON largely reduced R_f in the NCM/graphite full cell from 6.0 to 2.9 Ω (Table 4.1). This change is attributable to the enhanced stability of the electrode–electrolyte interface derived from the presence of TMS-ON. It is evident that a vulnerable interfacial layer builds up in the baseline electrolyte, which does not suppress continued electrolyte decomposition at the electrodes, resulting in an increase of R_f. In contrast, the TMS-ON-derived interfacial layer effectively prevents the electrolyte side reactions, resulting in protection of the electrolyte–electrode interface at 45 °C.

^{1}H NMR measurements revealed that 0.5% TMS-ON is entirely converted into ON and TMSF in the NCM/graphite full cell (Figure 4.9a). TMSF remains unreacted in the NCM/graphite full cell after 400 cycles at 45 °C (Figure 4.9b). By contrast, it is thought that ON generated from the reaction of TMS-ON with HF contributes to the formation of the CEI on the NCM cathode.

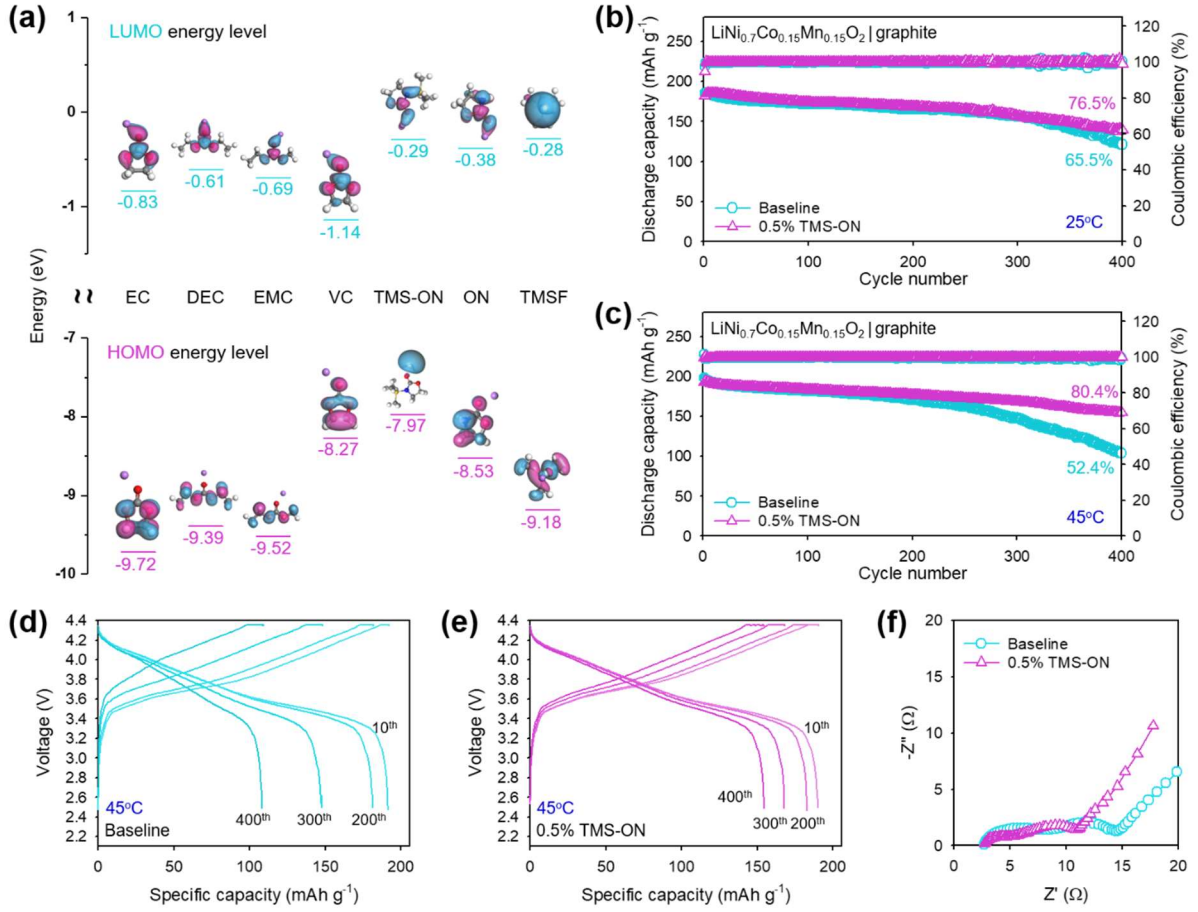

Figure 4.8 (a) HOMO and LUMO energy levels of EC, DEC, EMC, VC, TMS-ON, ON, and TMSF interacting with a Li^+ ion. Electrochemical performance of NCM/graphite full cells: Cycle performance of NCM/graphite full cells with baseline and 0.5% TMS-ON electrolytes at (b) 25°C and (c) 45°C (charge and discharge rate: 0.5C) and voltage profiles of NCM/graphite full cells with (d) baseline and (e) 0.5% TMS-ON electrolyte at 45 °C for the 10th, 100th, 200th, 300th, and 400th cycles. (f) Nyquist plots of NCM/graphite full cells after 400 cycles at 45°C.

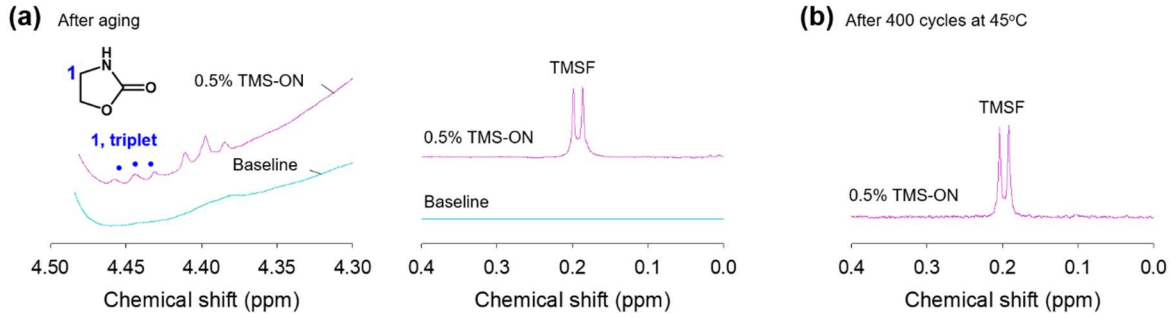

Figure 4.9 ^{1}H NMR spectra of baseline and 0.5% TMS-ON electrolytes retrieved from NCM/graphite full cells (a) before precycling (after aging at 45 °C for 1 h and 25 °C for 20 h) and (b) after 400 cycles at 45°C.

Table 4.1 Equivalent circuit and impedance parameters obtained from the simulation of NCM/graphite full cells after 400 cycles at 45°C; (a) Electrolyte resistance, (b) SEI and CEI film resistance, (c) Charge transfer resistance, (d) Sum of R_f and R_{ct} and (e) Ohmic resistance.

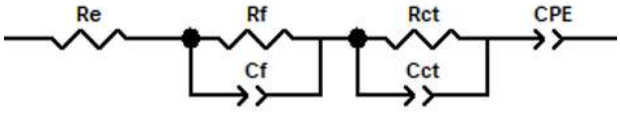

	R_e[a)] [Ω]	R_f[b)] [Ω]	R_{ct}[c)] [Ω]	Interfacial resistance[d)] [Ω]	R_{total}[e)] [Ω]
Baseline	2.6	6.0	5.9	11.9	14.5
0.5% TMS-ON	2.5	2.9	5.9	8.8	11.3

The effect of the 0.5% TMS-ON-containing electrolyte on the interface structure of NCM cathodes was investigated using *ex situ* XPS. The C 1s spectrum in Figure 4. shows that the surface of the NCM cathode cycled with the baseline electrolyte was covered with poly(VC) species, which were generated by the polymerization of VC. As VC has the highest HOMO energy level, it is prone to oxidation at the NCM cathode.[150] In contrast, the poly(VC) peak at 290.5 eV was not observed for the NCM cathode cycled with the 0.5% TMS-ON-containing electrolyte, whereas peaks corresponding to N–C and O=C–N moieties formed by oxidative decomposition of ON appeared at 286 and 287.4 eV, respectively (Figure 4.10b). Further, the N 1s core level spectra support that the CEI contains N–C and O=C–N moieties (Figure 4.10e). The HF scavenging effect of the TMS-ON additive slightly reduced the relative fraction of LiF and NiF_2 in the CEI (Figure 4.10c and d). The interfacial structure of the NCM cathode in the baseline electrolyte mainly consists of the VC-derived CEI, whereas the presence of TMS-ON greatly modifies the interface structure of the NCM cathode. The beneficial effect of the ON-derived CEI on the interfacial stability of the NCM cathode is shown in Figure 4.10f. The extent of transition-metal dissolution from the delithiated NCM cathode with a VC-derived or ON-derived CEI stored in the baseline electrolyte at 45 °C for 7 days was characterized by inductively coupled plasma optical emission spectrometry (ICP-OES). Transition-metal dissolution was alleviated for the NCM cathode with the ON-derived CEI, which suggests that the interfacial stability of the NCM cathode at 45 °C is enhanced by the ON-derived CEI. We propose possible oxidative radical polymerization mechanisms for VC and ON initiated by the radical cation ($\cdot O–CH=CH^+$) produced by $1e^-$ oxidation of VC (Figure 4.10g). The Gasteiger group reported an oxidative decomposition mechanism for VC to produce poly(VC), which is the main component of the VC-derived CEI at the NCM cathode.[16] Formation of the ON-derived CEI may be promoted by $\cdot O–CH=CH^+$ attack because the HOMO energy level of ON is lower than that of VC. Reactive $\cdot O\text{-}CH=CH^+$ can attack the carbon between the nitrogen and oxygens of ON to form a polymer species with an amide group.

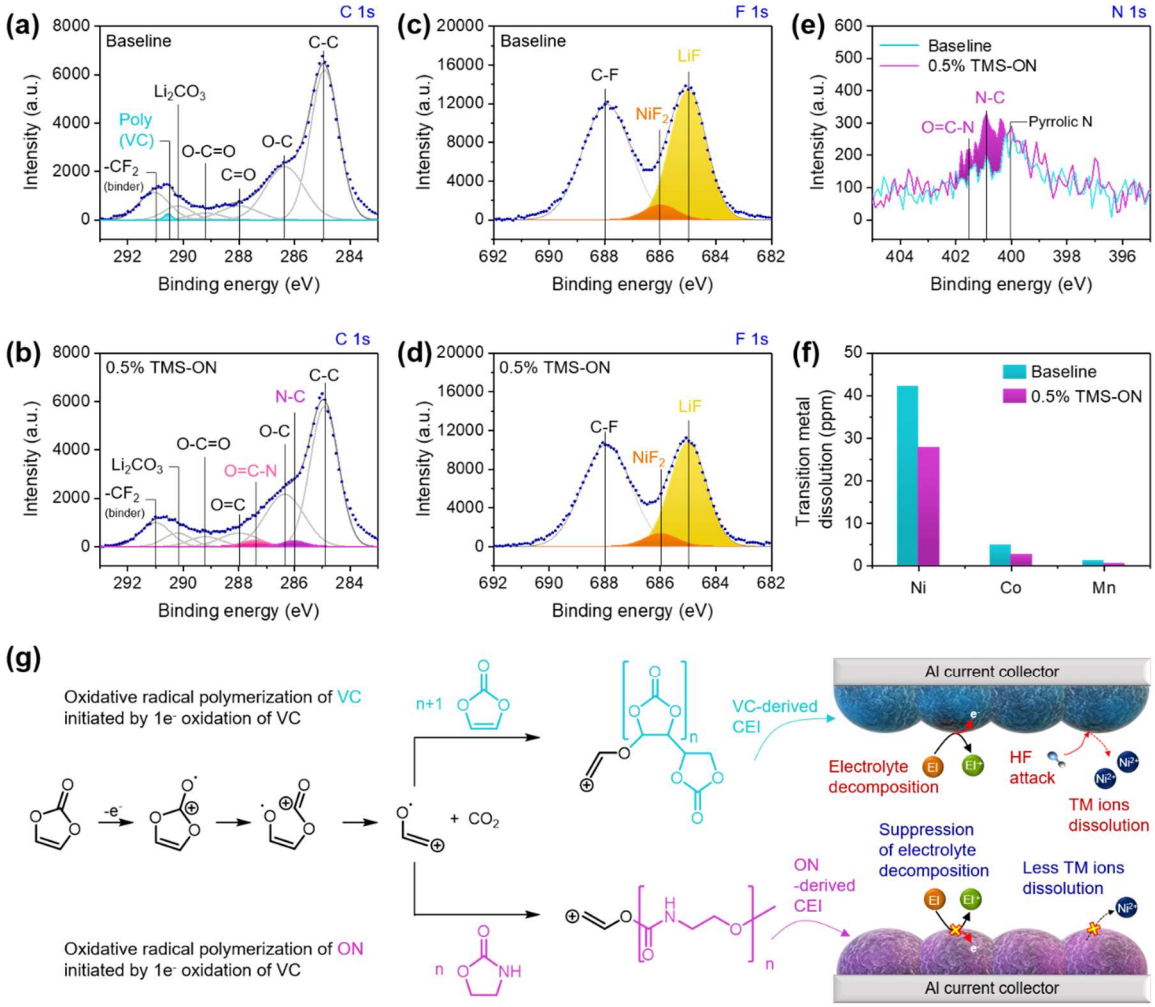

Figure 4.10 XPS spectra of NCM cathodes retrieved from NCM/graphite full cells with baseline and 0.5% TMS-ON electrolytes after 3 cycles at 25 °C (charge and discharge rates: 0.2C): C 1s spectra of NCM cathodes with (a) baseline and (b) 0.5% TMS-ON electrolytes; F 1s spectra of NCM cathodes with (c) baseline and (d) 0.5% TMS-ON electrolyte; and (e) N 1s spectra of NCM cathodes with baseline and 0.5% TMS-ON electrolytes. (f) Transition-metal dissolution from a delithiated NCM cathode with a VC- or ON-derived CEI following storage in the baseline electrolyte at 45 °C for 7 days. (g) Possible oxidative radical polymerization mechanisms of VC and ON initiated by the radical cation produced by oxidation of VC.

The effect of ON on the interfacial structure of NCM cathodes was analyzed using the surface-sensitive technique, TOF-SIMS.[152-154] A strong CN^- signal appeared in the TOF-SIMS spectrum of the NCM cathode with the 0.5% TMS-ON electrolyte after 400 cycles at 45 °C (Figure 4.11a). For the NCM cathode with the baseline electrolyte, which builds up a VC-derived CEI on the cathode, the TOF-SIMS spectrum showed strong signals corresponding to $^7LiF_2^-$, PO_2^-, and PO_3^-. This result implies that the VC-derived CEI is not robust enough to mitigate the continued oxidative decomposition of the electrolyte at the NCM cathode. In contrast, the ON-derived CEI containing CN^- species exhibited relatively weak $^7LiF_2^-$, PO_2^-, and PO_3^- signals, indicating that electrolyte decomposition at the cathode was suppressed. The 3D visualization was in agreement with the abovementioned spectral results (Figure 4.11b and c). Clearly, CN^- species were detected in the outer layer of the ON-derived CEI, and PO_2^- and PO_3^- were clearly observed in the outer layer of the VC-derived CEI. The normalized depth profiles show that the decomposition byproduct of the baseline electrolyte, $^7LiF_2^-$, was detected in the inner layer of both CEIs, with a higher $^7LiF_2$ signal intensity observed for the VC-derived CEI (Figure 4.11d). The middle layer of the ON-derived CEI was mainly composed of C_2HO^-, CHO_2^-, and $^7LiF_2^-$ species, and a strong $^7LiF_2^-$ signal was measured in the inner layer of the ON-derived CEI (Figure 4.11e). These results suggest that the outer layer of the ON-derived CEI consists of polar groups, facilitating Li-ion migration, whereas the middle layer contains mechanically stable $^7LiF_2^-$ species. The ON-derived CEI mitigated the dissolution of transition metals, especially Ni, from the delithiated cathode and contributed to suppressing the deposition of transition metals on the graphite anode, as evidenced by the reduction in the relative fraction of NiF_2 on the anode (Figure 4.10f and Figure 4.12).

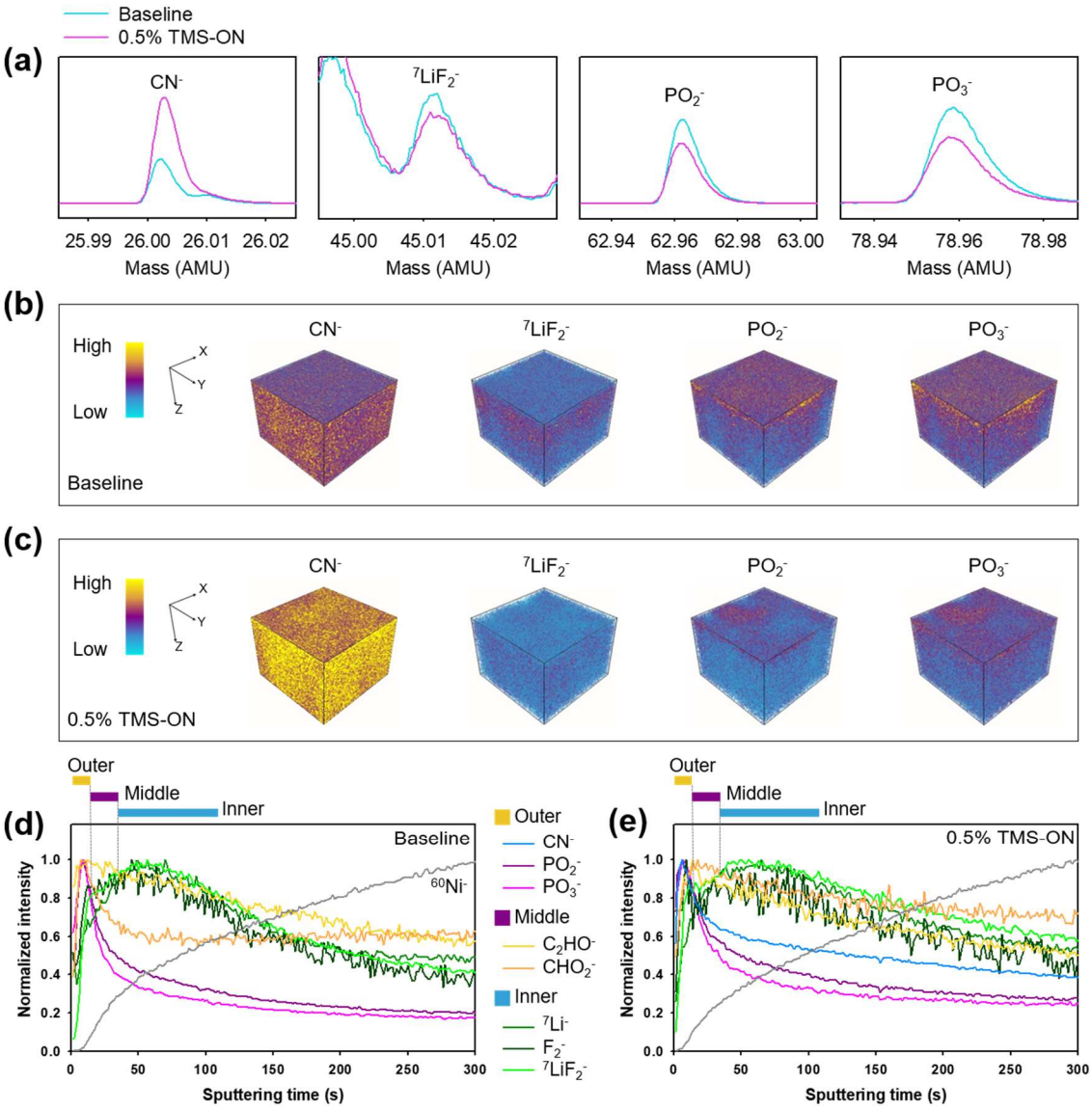

Figure 4.11 TOF-SIMS analysis of NCM cathodes retrieved from NCM/graphite full cells with baseline and 0.5% TMS-ON electrolytes after 400 cycles at 45 °C (charge and discharge rates: 0.5C). (a) TOF-SIMS spectra for CN^-, $^7LiF_2^-$, PO_2^-, and PO_3^- integrated over 300 s. 3D visualization and depth profiles of the CEIs on the NCM cathodes cycled with (b) and (d) the baseline electrolyte and (c) and (e) the 0.5% TMS-ON electrolyte with Cs^+ sputtering.

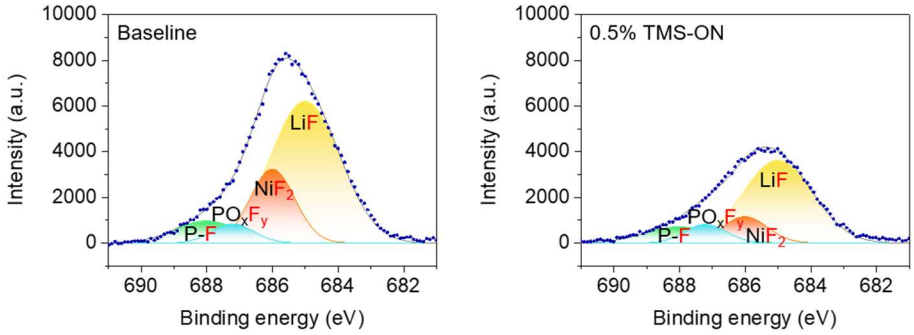

Figure 4.12 F 1s XPS spectra of graphite anodes retrieved from NCM/graphite full cells with baseline and 0.5% TMS-ON-containing electrolytes after 400 cycles at 45 °C (charge and discharge rates: 0.5C).

The microstructures of the NCM cathodes after 400 cycles at 45 °C were confirmed through HR-TEM imaging and fast Fourier transform (FFT) analysis. The original NCM structure is a layered structure in the $R\bar{3}m$ space group that facilitates the insertion and extraction of Li^+; however, as degradation progresses, the NCM structure changes to the electrochemically inert rock-salt phase in the $Fm\bar{3}m$ space group (Figure 4.13a-d). It is shown that the phase transformation occurs from the surface to the bulk of the NCM cathode. After 400 cycles at 45 °C, the NCM cathode cycled with the baseline electrolyte had the rock-salt phase and a mixed phase that combined the rock-salt and layered structures (Figure 4.13a). The FFT patterns reveal the surface rock-salt phase at site A, the mixed phase at site B, and the original layered structure at site C, with a phase transformation thickness of approximately 24.6 nm. With the 0.5% TMS-ON-containing electrolyte, the phase transformation thickness of the NCM cathode was significantly reduced to ~7.5 nm and the FFT patterns confirmed a rock-salt phase at site D, a mixed phase site E, and the layered structure at site F (Figure 4.13b). It is clear that the stable ON-derived CEI on the NCM cathode inhibits the exposure of the NCM active surface to the electrolyte and thereby the reduction of highly reactive Ni^{4+} to lower oxidation states (Ni^{3+}, Ni^{2+}) in the delithiated state is effectively mitigated. Ni^{2+}, which is similar in size to Li^+, tends to aggravate Li/Ni cation mixing in the NCM cathode. Scanning transmission electron microscopy (STEM) provided further evidence on the atomic scale for the formation of the rock-salt phase. The baseline electrolyte led to the formation of a thick rock-salt phase (>11 nm) in the NCM cathode owing to transition metals replacing Li^+ in the Li slab, whereas 0.5% TMS-ON-containing electrolyte resulted in a relatively thin rock-salt phase (~4 nm) (Figure 4.13c and d). The phase transformations of the NCM cathodes were directly supported by EELS, which distinguishes electronic structure of NCM particle about oxidation state of transition metal.[155-158] A series of O K-edge EELS spectra were obtained at 1 nm intervals from the surface to the bulk of the NCM particle (Figure 4.13e and f). The pre-edge peak of the O K-edge at approximately 528–530 eV is attributable to the transition of electrons from the O 1s state to the O 2p state hybridized with the 3d state of a transition metal; a shift of this peak to higher energy losses indicates the reduction of the transition metals. The phase transformation from the layered structure to the rock-salt structure occurred to a depth of 4 nm for the NCM cathode cycled with the 0.5% TMS-ON-containing electrolyte, whereas the phase transformation was detected to a depth of 14 nm for the NCM cathode cycled with the baseline electrolyte. The Ni L-edge spectra showed that there is more Ni^{2+} than Ni^{3+} on the surface, with the proportion of Ni^{3+} increasing toward the bulk (Figure 4.14). The mechanical integrity of the NCM secondary particles was explored in the baseline and 0.5% TMS-ON-containing electrolytes. Notably, severe intergranular cracking was observed for the NCM cathode cycled with the baseline electrolyte. This result implies that the VC-based CEI formed by the baseline electrolyte is not uniform, and

thereby, inhomogeneous lithiation/delithiation of the cathode occurs. Different levels of lithiation/delithiation in the NCM primary particles trigger mechanical disintegration to NCM secondary particles (Figure 4.13g and h). Further, the vulnerable VC-derived CEI does not effectively protect the NCM cathode particles upon prolonged cycling, which causes thickening of the CEI by continued oxidative decomposition of the electrolyte at the NCM cathode (Figure 4.15a). The detection of a strong F signal for the NCM cathode particle cycled with the baseline electrolyte indicates that byproducts from $LiPF_6$ decomposition are accumulated inside the cathode particles. The NCM particles cycled with the 0.5% TMS-ON-containing electrolyte did not experience intergranular cracking (Figure 4.13i and j) because the ON-derived CEI generated by the TMS-ON-containing electrolyte was stably maintained during cycling, which prevented continuous electrolyte decomposition at the cathode (Figure 4.15b).

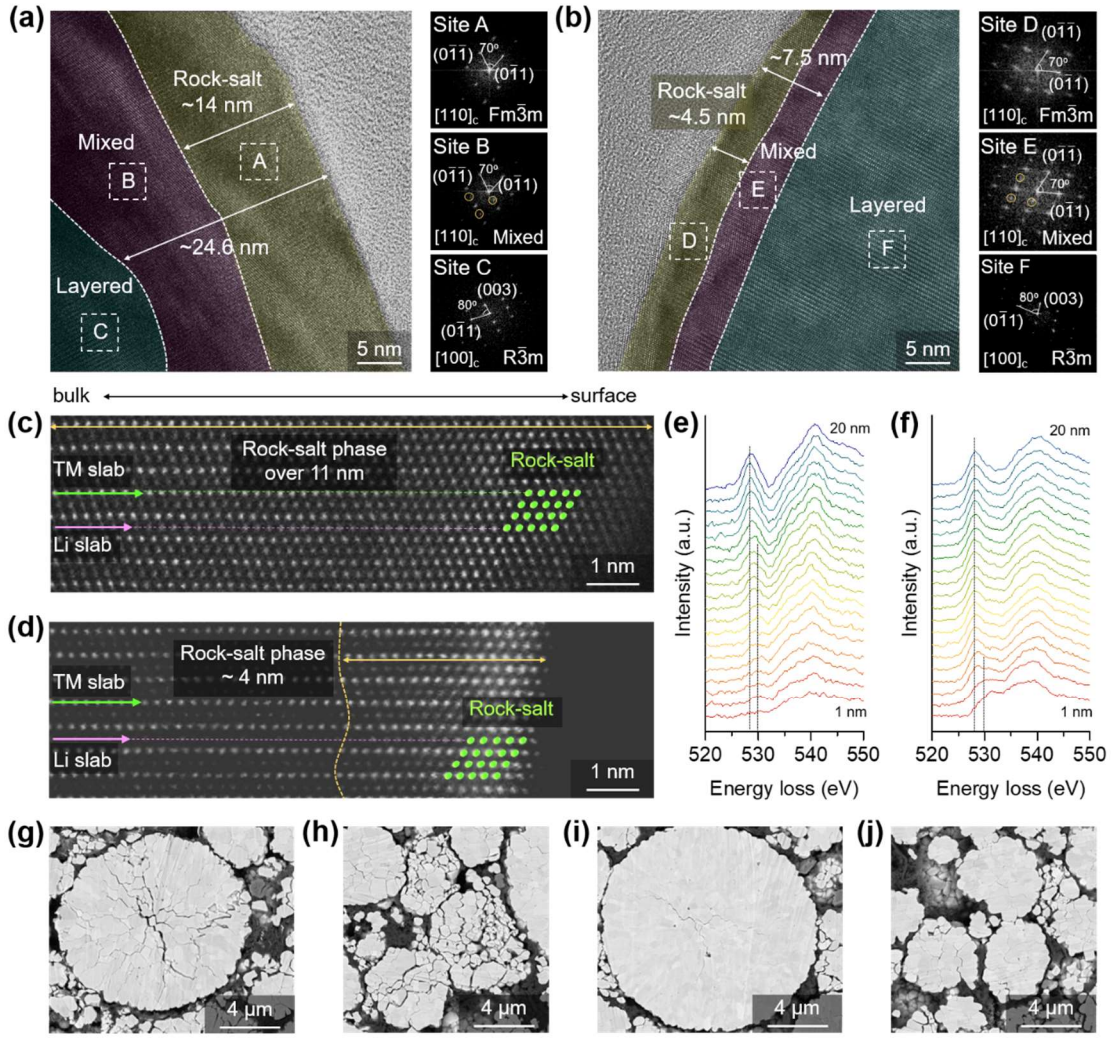

Figure 4.13. Microstructure and nanostructure of the NCM cathodes retrieved from NCM/graphite full cells after 400 cycles at 45 °C (charge and discharge rates: 0.5C). TEM and FFT images of NCM cathodes cycled with (a) baseline and (b) 0.5% TMS-ON electrolytes. Magnified STEM images of the surfaces of NCM cathodes cycled with (c) baseline and (d) 0.5% TMS-ON electrolytes. Series of EELS spectra for the O K-edge from the surface to the inner bulk of NCM particles cycled with (e) baseline and (f) 0.5% TMS-ON electrolytes (every 1 nm). Cross-sectional SEM images of NCM cathodes cycled with (g) and (h) baseline and (i) and (j) 0.5% TMS-ON electrolytes.

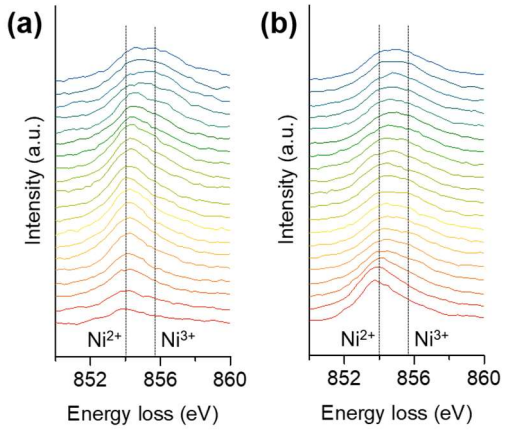

Figure 4.14 Series of EELS spectra for the NCM cathodes retrieved from NCM/graphite full cells after 400 cycles at 45 °C (charge and discharge rates: 0.5C). Ni L-edge spectra from the surface to the inner bulk of NCM particles cycled with (a) baseline and (b) 0.5% TMS-ON-containing electrolytes (every 1 nm).

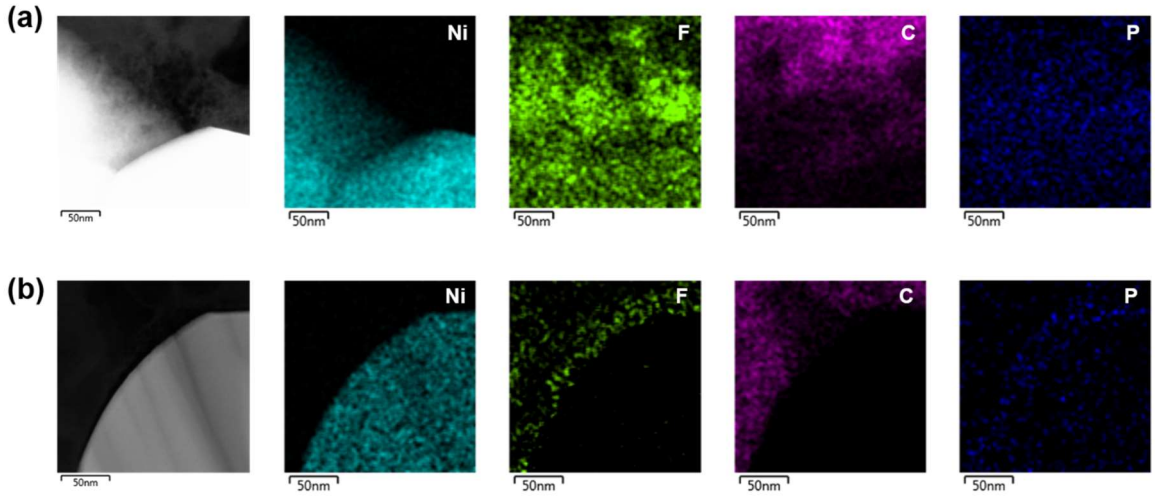

Figure 4.15 EDS mapping of an NCM cathode retrieved from an NCM/graphite full cell cycled with the (a) baseline electrolyte and (b) 0.5% TMS-ON electrolyte for 400 cycles at 45 °C (charge and discharge rates: 0.5C).

4.4 Conclusion

We have demonstrated that TMS-ON as an electrolyte additive improves the electrochemical performance of LIBs composed of Ni-rich NCM cathodes and graphite anodes with a practical mass loading. TMS-ON stabilized the $LiPF_6$-based electrolyte by mitigating the hydrolysis of ion-paired $LiPF_6$, stabilizing PF_5, and capturing HF from the electrolyte. Deactivation of reactive species such as HF enhanced the structural and compositional stability of the SEI on the graphite anode in a Ni-rich NCM/graphite full cell. Moreover, the ON-derived interfacial layer on the Ni-rich NCM cathode was stably maintained over 400 cycles at 45 °C, which reduced transition-metal dissolution from the NCM cathode, suppressed the irreversible phase transition and microcracking of the Ni-rich NCM cathode, and prevented continual electrolyte decomposition at the cathode. The results of this study will contribute to further advancing the design of electrolyte additives that can remove undesirable reactive species and contribute to the construction of a controlled and stable electrolyte–electrode interface

References

(1) Goodenough, J. B.; Kim, Y. Challenges for Rechargeable Li Batteries, *Chem. Mater*. **2010**, *22,* 587-603.

(2) Armand, M.; Tarascon, J.-M. Building Better Batteries, *Nature,* **2008**, *451,* 652-657.

(3) Li, M.; Lu, J.; Chen, Z.; Amine, K. 30 Years of Lithium-Ion Batteries, *Adv. Mater.* **2018**, *30,* 1800561

(4) Etacheri, V.; Marom, R.; Elazari, R.; Salitra, G.; Aurbach, D. Challenges in the Development of Advanced Li-Ion Batteries: a Review, *Energy Environ. Sci*. **2011**, *4,* 3243-3262.

(5) Choi, N.-S.; Chen, Z.; Freunberger, S. A.; Ji, X.; Sun, Y.-K.; Amine, K.; Yushin, G.; Nazar, L. F.; Cho, J.; Bruce, P. G. Challenges Facing Lithium Batteries and Electrical Double-Layer Capacitors, *Angew. Chem. Int. Ed.* **2012**, *51,* 9994-10024.

(6) Li, W.; Song, B.; Manthiram, A. High-Voltage Positive Electrode Materials for Lithium-Ion Batteries, *Chem. Soc. Rev.* **2017**, *46*, 3006-3059.

(7) Liu, W.; Oh, P.; Liu, X.; Lee, M.-J.; Cho, W.; Chae, S.; Kim, Y.; Cho, J. Nickel-Rich Layered Lithium Transition-Metal Oxide for High-Energy Lithium-Ion Batteries, *Angew. Chem. Int. Ed.* **2015**, *54*, 4440-4457.

(8) Manthiram, A.; Knight, J. C.; Myung, S.-T.; Oh, S.-M.; Sun, Y.-K. Nickel-Rich and Lithium-Rich Layered Oxide Cathodes: Progress and Perspectives, *Adv. Energy Mater.* **2016**, *6,* 1501010.

(9) Sun, Y.-K.; Myung, S.-T.; Park, B.-C.; Prakash, J.; Belharouak, I.; Amine, K. High-Energy Cathode Material for Long-Life and Safe Lithium Batteries, *Nat. Mater.* **2009**, *8*, 320-324.

(10) Scrosati, B.; Garche, J. Lithium Batteries: Status, Prospects and Future, *J. Power Sources* **2010**, *195*, 2419-2430.

(11) Koyama, Y.; Arai, H.; Tanaka, I.; Uchimoto, Y.; Ogumi, Z. Defect Chemistry in Layered $LiMO_2$ (M = Co, Ni, Mn, and $Li_{1/3}Mn_{2/3}$) by First-Principles Calculations, *Chem. Mater.* **2012**, *24*, 3886-3894.

(12) Yu, H. J.; Qian, Y. M.; Otani, M. R.; Tang, D. M.; Guo, S. H.; Zhu, Y. B.; Zhou, H. S. Study of the Lithium/Nickel Ions Exchange in the Layered $LiNi_{0.42}Mn_{0.42}Co_{0.16}O_2$ Cathode Material for Lithium Ion Batteries: Experimental and First-Principles Calculations, *Energy Environ. Sci.* **2014**, *7*, 1068-1078.

(13) Liu, H. S.; Yang, Y.; Zhang, J. J. Reaction Mechanism and Kinetics of Lithium Ion Battery Cathode Material $LiNiO_2$ with CO_2, *J. Power Sources* **2007**, *173*, 556-561.

(14) Cho, D.-H.; Jo, C.-H.; Cho, W.; Kim, Y.-J.; Yashiro, H.; Sun, Y.-K.; Myung, S.-T. Effect of Residual Lithium Compounds on Layer Ni-Rich $Li[Ni_{0.7}Mn_{0.3}]O_2$, *J. Electrochem. Soc.* **2014**, *161*, A920-A926.

(15) Yan, P.; Zheng, J.; Gu, M.; Xiao, J.; Zhang, J.-G.; Wang, C.-M. Intragranular Cracking as a Critical Barrier for High-Voltage Usage of Layer-Structured Cathode for Lithium-Ion Batteries, *Nat. Commun.* **2017**, *8*, 14101-14109.

(16) Kim, N. Y.; Yim, T.; Song, J. H.; Yu, J.-S.; Lee, Z. Microstructural Study on Degradation Mechanism of Layered $LiNi_{0.6}Co_{0.2}Mn_{0.2}O_2$ Cathode Materials by Analytical Transmission Electron Microscopy, *J. Power Sources* **2016**, *307*, 641-648.

(17) Jung, R.; Metzger, M.; Maglia, F.; Stinner, C.; Gasteiger, H. A. Oxygen Release and Its Effect on the Cycling Stability of $LiNi_xMn_yCo_zO_2$ (NMC) Cathode Materials for Li-Ion Batteries, *J. Electrochem. Soc.* **2017**, *164*, A1361-A1377.

(18) Streich, D.; Erk, C.; Gueguen, A.; Muller, P.; Chesneau, F. F.; Berg, E. J. Operando Monitoring of Early Ni-mediated Surface Reconstruction in Layered Lithiated Ni–Co–Mn Oxides, *J. Phys. Chem. C* **2017**, *121*, 13481-13486.

(19) Armstrong, A. R.; Holzapfel, M.; Novak, P.; Johnson, C. S.; Kang, S. H.; Thackeray, M. M.; Bruce, P. G. Demonstrating Oxygen Loss and Associated Structural Reorganization in the Lithium Battery Cathode $Li[Ni_{0.2}Li_{0.2}Mn_{0.6}]O_2$, *J. Am. Chem. Soc.* **2006**, *128*, 8694-8698.

(20) Freunberger, S. A.; Chen,Y. H.; Peng, Z. Q.; Griffin, J. M.; Hardwick, L. J.; Barde, F.; Novak, P.; Bruce, P. G. Reactions in the Rechargeable Lithium–O_2 Battery with Alkyl Carbonate Electrolytes, *J. Am. Chem. Soc.* **2011**, *133*, 8040-8047.

(21) Park, C.-M.; Kim, J.-H.; Kim, H.; Sohn, H.-J. Li-Alloy Based Anode Materials for Li Secondary Batteries, *Chem. Soc. Rev.* **2010**, *39*, 3115-3141.

(22) Szczech, J. R.; Jin, S. Nanostructured Silicon for High Capacity Lithium Battery Anodes, *Energy Environ. Sci.* **2011**, *4*, 56-72.

(23) Wu, H.; Chan, G.; Choi, J. W.; Ryu, I.; Yao, Y.; McDowell, M. T.; Lee, S. W.; Jackson, A.; Yang, Y.; Hu, L.; Cui, Y. Stable Cycling of Double-Walled Silicon Nanotube Battery Anodes through Solid–Electrolyte Interphase control, *Nat. Nanotechnol.* **2012**, *7*, 310-315.

(24) Li, J.-Y.; Xu, Q.; Li, G.; Yin, Y.-X.; Wan, L.-J.; Guo, Y.-G. Research Progress Regarding Si-Based Anode Materials Towards Practical Application in High Energy Density Li-Ion Batteries, *Mater. Chem. Front.* **2017**, *1*, 1691-1708.

(25) Xu, K. Electrolytes and Interphases in Li-Ion Batteries and Beyond, *Chem. Rev.* **2014**, *114,* 11503-11618.

(26) Krause, L.; Lamanna, J. W.; Summerfield, J.; Engle, M.; Korba, G.; Loch, R.; Atanasoski, R. Corrosion of Aluminum at High Voltages in Non-aqueous Electrolytes Containing Perfluoroalkylsulfonyl Imides; New Lithium Salts for Lithium-Ion Cells, *J. Power Sources*, **1997**, *68*, 320-325.

(27) Dahbi, M.; Ghamouss, F.; Tran-Van, F.; Lemordant, D.; Anouti, M. Comparative Study of EC/DMC LiTFSI and $LiPF_6$ Electrolytes for Electrochemical Storage, *J. Power Sources*, **2011**, *196*, 9743-9750.

(28) Seo, D. M.; Borodin, O.; Han, S.-D.; Ly, Q.; Boyle, P. D.; Henderson, W. A. Electrolyte Solvation and Ionic Association, *J. Electrochem. Soc.* **2012**, *159*, A553-A565.

(29) Seo, D. M.; Borodin, O.; Han, S.-D.; Boyle, P. D.; Henderson, W. A. Electrolyte Solvation and Ionic Association II. Acetonitrile-Lithium Salt Mixtures: Highly Dissociated Salts, *J. Electrochem. Soc*. **2012**, *159*, A1489-A1500.

(30)Seo, D. M.; Borodin, O.; Balogh, D.; O'Connell, M.; Ly, Q.; Han, S.-D.; Passerini, S.; Henderson, W. A. Electrolyte Solvation and Ionic Association III. Acetonitrile-Lithium Salt Mixtures–Transport Properties, *J. Electrochem. Soc*. **2013**, *160*, A1061-A1070.

(31) Aravindan, V.; Gnanaraj, J.; Madhavi, S.; Liu, H. K. Lithium-Ion Conducting Electrolyte Salts for Lithium Batteries, *Chem.-Eur. J.* **2011**, *17*, 14326-14346.

(32)Kawamura, T.; Kimura, A.; Egashira, M.; Okada, S.; Yamaki, J.-I. Thermal Stability of Alkyl Carbonate Mixed-Solvent Electrolytes for Lithium Ion Cells, *J. Power Sources*, **2002**, *104*, 260-264.

(33) Sloop, S. E.; Pugh, J. K.; Wang, S.; Kerr, J. B.; Kinoshita, K.; Chemical Reactivity of PF_5 and $LiPF_6$ in Ethylene Carbonate/Dimethyl Carbonate Solutions, *Electrochem. Solid-State Lett.* **2001**, *4*, A42-A44.

(34) Xuan, X. P.; Wang, J. J.; Wang, H. Q. Theoretical Insights into PF_6^- and its Alkali Metal Ion Pairs: Geometries and Vibrational Frequencies, *Electrochim. Acta* **2005**, *50*, 4196-4201.

(35) Kanamura, K.; Shiraishi, S.; Takehara, Z. Electrochemical Deposition of Very Smooth Lithium Using Nonaqueous Electrolytes Containing HF, *J. Electrochem. Soc.* **1996**, *143*, 2187-2197.

(36) Andersson, A. M.; Herstedt, M.; Bishop, A. G.; Edström, K. The influence of lithium salt on the interfacial reactions controlling the thermal stability of graphite anodes, *Electrochim. Acta* **2002**, *47*, 1885-1898.

(37) Gilbert, J. A.; Shkrob, I. A.; Abraham, D. P. Transition Metal Dissolution, Ion Migration, Electrocatalytic Reduction and Capacity Loss in Lithium-Ion Full Cells, *J. Electrochem. Soc.* **2017**, *164*, A389-A399.

(38) Wilken, S.; Treskow, M.; Scheers, J.; Johansson, P.; Jacobsson, P. Initial Stages of Thermal Decomposition of $LiPF_6$-based Lithium Ion Battery Electrolytes by Detailed Raman and NMR Spectroscopy, *RSC Advances*, **2013** *3*, 16359-16364.

(39) Zhan, C.; Wu, T.; Lu, J.; Amine, K. Dissolution, Migration, and Deposition of Transition Metal Ions in Li-Ion Batteries Exemplified by Mn-Based Cathodes – a Critical Review, *Energy Environ. Sci.* **2018**, *11*, 243-257.

(40) Wang, Z. X.; Huang, X. J.; Chen, L. Q. Characterization of Spontaneous Reactions of $LiCoO_2$ with Electrolyte Solvent for Lithium-Ion Batteries, *J. Electrochem. Soc.* **2004**, *151*, A1641-A1652.

(41) Andersson, A. M.; Edström, K. Chemical Composition and Morphology of the Elevated Temperature SEI on Graphite, *J. Electrochem. Soc.* **2001**, *148*, A1100-A1109.

(42) Pieczonka, N. P. W.; Liu, Z. Y.; Lu, P.; Olson, K. L.; Moote, J.; Powell, B. R.; Kim, J. H. Understanding Transition-Metal Dissolution Behavior in $LiNi_{0.5}Mn_{1.5}O_4$ High-Voltage Spinel for Lithium Ion Batteries, *J. Phys. Chem. C* **2013**, *117*, 15947-15957.

(43) Bhandari, A.; Bhattacharya, J. Review—Manganese Dissolution from Spinel Cathode: Few Unanswered Questions, *J. Electrochem. Soc.* **2017**, *164*, A106-A127.

(44) Yu, X.; Manthiram, A. Electrode–Electrolyte Interfaces in Lithium-Based Batteries, *Energy Environ. Sci.* **2018**, *11*, 527-543.

(45) Cheng, X.-B.; Zhang, R.; Zhao, C.-Z.; Wei, F.; Zhang, J.-G.; Zhang, Q. A Review of Solid Electrolyte Interphases on Lithium Metal Anode, *Adv. Sci*. **2016**, *3*, 1500213.

(46) Zhao, H.; Yu, X.; Li, J.; Li,B.; Shao, H.; Li, L.; Deng, Y. Film-Forming Electrolyte Additives for Rechargeable Lithium-Ion Batteries: Progress and Outlook, *J. Mater. Chem. A*, **2019**, *7*, 8700-8722.

(47) Banerjee, A.; Shilina, Y.; Ziv, B.; Ziegelbauer, J. M.; Luski, S.; Aurbach, D.; Halalay, I. C. Review—Multifunctional Materials for Enhanced Li-Ion Batteries Durability: A Brief Review of Practical Options, *J. Electrochem. Soc*. **2017**, *164*, A6315-A6323.

(48) Han, J.-G.; Kim, K.; Lee, Y.; Choi, N.-S. Scavenging Materials to Stabilize $LiPF_6$-Containing Carbonate-Based Electrolytes for Li-Ion Batteries, *Adv. Mater.* **2018**, *31*, 1804822.

(49) Sun, X.; Lee, H. S.; Yang, X.-Q.; McBreen, J. Using a Boron-Based Anion Receptor Additive to Improve the Thermal Stability of $LiPF_6$-Based Electrolyte for Lithium Batteries, *Electrochem. Solid-State Lett.* **2002**, *5*, A248-A251.

(50) Cai, Z.; Liu, Y.; Zhao, J.; Li, L.; Zhang, Y.; Zhang, J. Tris(trimethylsilyl) borate as electrolyte additive to improve performance of lithium-ion batteries, *J. Power Sources*, **2012**, *202*, 341– 346.

(51) Wang, X.; Xing, L.; Liao, X.; Chen, X.; Huang, W.; Yu, Q.; Xu, M.; Huang, Q.; Li, W. Improving Cyclic Stability of Lithium Cobalt Oxide Based Lithium Ion Battery at High Voltage by Using Trimethylboroxine as an Electrolyte Additive, *Electrochim. Acta*, **2015**, *173*, 804–811.

(52) Kim, J.; Kim, H.-s.; Lee, J. G.; Jeong, H.; Ryu, J. H.; Oh, S. M. Communication—A Phosphorus Pentafluoride Scavenger to Suppress Solid Electrolyte Interphase Damage at Moderately Elevated Temperature, *Electrochem. Soc.* **2017**, *164*, A3699-A3701.

(53) Choo, M.-H.; Nguyen, C. C.; Hong, S.; Kwon, Y. H.; Woo, S.-W.; Kim, J. Y.; Song, S.-W. Combination of Acid-Resistor and -Scavenger Improves the SEI Stability and Cycling Ability of Tin–Nickel Battery Anodes in $LiPF_6$-Containing Electrolyte, *Electrochim. Acta*, **2013**, *112*, 252– 257.

(54) Li, W.; Lucht, B. L. Inhibition of Solid Electrolyte Interface Formation on Cathode Particles for Lithium-Ion Batteries, *J. Power Sources*, **2007**, *168*, 258–264.

(55) Song, Y.-M.; Kim, C.-K.; Kim, K.-E.; Hong, S. Y.; Choi, N.-S. Exploiting Chemically and Electrochemically Reactive Phosphite Derivatives for High-Voltage Spinel $LiNi_{0.5}Mn_{1.5}O_4$ Cathodes, *J. Power Sources*, **2016**, *302*, 22-30.

(56) Wang, J.; Zhao, X.; Luo, H.; Yang, J.; Makoto, Y.; Zhang, L. A Novel Aminoalkyldisiloxane Compound as a Film-Forming Electrolyte Additive for Graphite Anode, *Electrochemistry* **2015**, *83*, 537-540.

(57) Li, Y. K.; Zhang, R. X.; Liu, J. S.; Yang, C. W. Effect of Heptamethyldisilazane as an Additive on the Stability Performance of $LiMn_2O_4$ Cathode for Lithium-Ion Battery *J. Power Sources* **2009**, *189*, 685-688.

(58) Heui, J. S.; Taeeun, Y. Effect of Silyl Ether-functinoalized Dimethoxydimethylsilane on Electrochemical Performance of a Ni-rich NCM Cathode, *ChemPhysChem* **2017**, *18*, 3402-3406.

(59) Wotango, A. S.; Su, W.-N.; Leggesse, E. G.; Haregewoin, A. M.; Lin, M.-H.; Zegeye, T. A.; Cheng, J.-H.; Hwang, B.-J. Improved Interfacial Properties of MCMB Electrode by 1-(Trimethylsilyl) imidazole as New Electrolyte Additive To Suppress $LiPF_6$ Decomposition, *ACS Appl. Mater. Interfaces*, **2017**, *9*, 2410-2420.

(60) Chen, J.; Liang, F.; Zhang, H.; Liu, J.; Li, C. N,N-diethyl-trimethylsilylamine as an Electrolyte Additive for Enhancing Electrochemical Performance of High Voltage Spinel Cathode, *Int. J. Electrochem. Sci.* **2017**, *12*, 7249-7261.

(61) Verma, P.; Maire, P.; Novak, P. A Review of the Features and Analyses of the Solid Electrolyte Interphase in Li-Ion Batteries, *Electrochim. Acta* **2010**, *55,* 6332-6341.

(62) Boukamp, B.A.; Lesh, G.C.; Huggins, R.A. All-Solid Lithium Electrodes with Mixed-Conductor Matrix, *J. Electrochem. Soc.* **1981**, *128*, 725-729.

(63) Zhao, X.; Zhuang, Q.C.; Xu, S.D.; Xu, Y.X.; Shi, Y.L.; Zhang, X.X. A New Insight into the Content Effect of Fluoroethylene Carbonate as a Film Forming Additive for Lithium-Ion Batteries*, Int. J. Electrochem. Sci*. **2015**, *10*, 2515-2534.

(64) McMillan, R.; Slegr, H.; Shu, Z.X.; Wang, W.D. Fluoroethylene Carbonate Electrolyte and Its Use in Lithium Ion Batteries with Graphite Anodes, *J. Power Sources* **1999**, *81*, 20-26.

(65) Profatilova, I.A.; Kim, S.S.; Choi, N.-S. Enhanced Thermal Properties of the Solid Electrolyte Interphase Formed on Graphite in an Electrolyte with Fluoroethylene Carbonate, *Electrochim. Acta* **2009**, *54*, 4445-4450.

(66) Nguyen, C.C.; Lucht, B.L. Comparative Study of Fluoroethylene Carbonate and Vinylene Carbonate for Silicon Anodes in Lithium Ion Batteries, *J. Electrochem. Soc.* **2014**, *161* A1933-A1938.

(67) Xu, C.; Lindgren, F.; Philippe, B.; Gorgoi, M.; Björefors, F.; Edström, K.; Gustafsson, T. Improved Performance of the Silicon Anode for Li-Ion Batteries: Understanding the Surface Modification Mechanism of Fluoroethylene Carbonate as an Effective Electrolyte Additive, *Chem. Mater.* **2015**, *27*, 2591-2599.

(68) Choi, N.-S.; Yew, K.H.; Lee, K.Y.; Sung, M.; Kim, H.; Kim, S.S. Effect of Fluoroethylene Carbonate Additive on Interfacial Properties of Silicon Thin-Film Electrode, *J. Power Sources* **2006**, *161*, 1254-1259.

(69) Kim, J.S.; Byun, D.; Lee, J.K. Electrochemical Characteristics of Amorphous Silicon Thin Film Electrode with Fluoroethylene Carbonate Additive, *Curr. Appl. Phys.* **2014**, *14,* 596-602.

(70) Nakai, H.; Kubota, T.; Kita, A.; Kawashima, A. Investigation of the Solid Electrolyte Interphase Formed by Fluoroethylene Carbonate on Si Electrodes, *J. Electrochem. Soc.* **2011**, *158*, A798-A801.

(71) Dalavi, S.; Guduru, P.; Lucht, B.L. Performance Enhancing Electrolyte Additives for Lithium Ion Batteries with Silicon Anodes, *J. Electrochem. Soc.* **2012**, *159*, A642-A646.

(72) Chen, X.L.; Li, X.L.; Mei, D.H.; Feng, J.; Hu, M.Y.; Hu, J.Z.; Engelhard, M.; Zheng, J.M.; Xu, W.; Xiao, J.; Liu, J.; Zhang, J.-G. Reduction Mechanism of Fluoroethylene Carbonate for Stable Solid-Electrolyte Interphase Film on Silicon Anode, *ChemSusChem* **2014**, *7*, 549-554.

(73) Lin, Y.M.; Klavetter, K.C., Abel, P.R.; Davy, N.C.; Snider, J.L.; Heller, A.; Mullins, C.B. High Performance Silicon Nanoparticle Anode in Fluoroethylene Carbonate-Based Electrolyte for Li-Ion Batteries, *Chem. Commun.* **2012**, *48*, 7268-7270.

(74) Etacheri, V.; Haik, O.; Goffer, Y.; Roberts, G.A.; Stefan, I.C.; Fasching, R.; Aurbach, D. Effect of Fluoroethylene Carbonate (FEC) on the Performance and Surface Chemistry of Si-Nanowire Li-Ion Battery Anodes, *Langmuir* **2012**, *28*, 965-976.

(75) Sinha, N.N.; Burns, J.C.; Dahn, J.R. Storage Studies on Li/Graphite Cells and the Impact of So-Called SEI-Forming Electrolyte Additives, *J. Electrochem. Soc.* **2013**, *160*, A709-A714.

(76) Cho, I.H.; Kim, S.S.; Shin, S.C.; Choi, N.-S. Effect of SEI on Capacity Losses of Spinel Lithium Manganese Oxide/Graphite Batteries Stored at 60 °C, *Electrochem. Solid-State Lett.* **2010**, *13*, A168-A172.

(77) Shin, H.; Park, J.; Sastry, A.M.; Lu, W. Effects of Fluoroethylene Carbonate (FEC) on Anode and Cathode Interfaces at Elevated Temperatures, *J. Electrochem. Soc.* **2015**, *162*, A1683-A1692.

(78) Kim, K.; Park, I.; Ha, S.-Y.; Kim, Y.; Woo, M.-H.; Jeong M.-H.; Shin, W. C.; Ue, M.; Hong, S. Y.; Choi, N.-S. Understanding the Thermal Instability of Fluoroethylene Carbonate in $LiPF_6$-Based Electrolytes for Lithium Ion Batteries, *Electrochim. Acta* **2017**, *225*, 358-368.

(79) Park, M.H.; Lee, Y. S.; Lee, H.; Han, Y.-K. Low Li^+ Binding Affinity: An Important Characteristic for Additives to Form Solid Electrolyte Interphases in Li-ion Batteries, *J. Power Sources* **2011**, *196*, 5109-5114.

(80) Wang, Z.; Xu, J.; Yao, W.-H.; Yao, Y.-W.; Yang, Y. Fluoroethylene Carbonate as an Electrolyte Additive for Improving the Performance of Mesocarbon Microbead Electrode, *ECS Trans.* **2012**, *41*, 29-40.

(81) Yan, G.; Li, X.; Wang, Z.; Guo, H.; Wang, J. Compatibility of Graphite with 1,3-(1,1,2,2-Tetrafluoroethoxy)propane and Fluoroethylene Carbonate as Cosolvents for Nonaqueous Electrolyte in Lithium-Ion Batteries, *J. Phys. Chem. C* **2014**, *118*, 6586-6593.

(82)Zhang, S.S. A Review on Electrolyte Additives for Lithium-Ion Batteries, *J. Power Sources* **2006**, *162*, 1379-1394.

(83) Shiraishi, S.; Kanamura, K.; Takehara, Z. Study of the Surface Composition of Highly Smooth Lithium Deposited in Various Carbonate Electrolytes Containing HF, *Langmuir* **1997**, *13*, 3542-3549.

(84) Dedryvere, R.; Gireaud, L.; Grugeon, S.; Laruelle, S.; Tarascon, J.M. Gonbeau, D. Characterization of Lithium Alkyl Carbonates by X-ray Photoelectron Spectroscopy: Experimental and Theoretical Study, *J. Phys. Chem. B* **2005**, *109*, 15868-15875.

(85) Gireaud, L.; Grugeon, S.; Laruelle, S.; Pilard, S.; Tarascon, J.M. Identification of Li Battery Electrolyte Degradation Products Through Direct Synthesis and Characterization of Alkyl Carbonate Salts, *J. Electrochem. Soc.* **2005**, *152*, A850-A857.

(86) Tasaki, K.; Goldberg, A.; Lian, J.J.; Walker, M.; Timmons, A.; Harris, S.J. Solubility of Lithium Salts Formed on the Lithium-Ion Battery Negative Electrode Surface in Organic Solvents, *J. Electrochem. Soc.* **2009**, *156*, A1019-A1027.

(87) Janes, A.; Thomberg, T.; Eskusson, J.; Lust, E. Fluoroethylene Carbonate and Propylene Carbonate Mixtures Based Electrolytes for Supercapacitors, *ECS Trans.* **2014**, *58*, 71-79.

(88) Chernyak, Y. Dielectric Constant, Dipole Moment, and Solubility Parameters of Some Cyclic Acid Esters, *J. Chem. Eng. Data* **2006**, *51*, 416-418.

(89) Rahman, A.-u.; Laali, K. K. Advances in Organic Synthesis: Modern Organofluorine Chemistry-Synthetic Aspects, 2nd ed.; Bentham Science, 2006.

(90) Amii, H.; Uneyama, K. C-F Bond Activation in Organic Synthesis, *Chem. Rev.* **2009**, *109*, 2119-2183.

(91) Stahl, T.; Klare, H. F. T.; Oestreich, M. Main-Group Lewis Acids for C−F Bond Activation, *ACS Catal.* **2013**, *3*, 1578-1587.

(92) Choi, N.-S.; Han, J.-G.; Ha, S.-Y.; Park, I.; Back, C.-K. Recent Advances of the Electrolytes for Interfacial Stability of High-Voltage Cathodes in Lithium-Ion Batteries, *RSC Adv.* **2015**, *5*, 2732-2748.

(93) Campion, C.L.; Li, W.; Lucht, B.L. Thermal Decomposition of $LiPF_6$-Based Electrolytes for Lithium-Ion Batteries, *J. Electrochem. Soc.* **2005**, *152*, A2327-A2334.

(94) Schipper, F.; Erickson, E. M.; Erk, C.; Shin, J.-Y.; Chesneau, F. F.; Aurbach, D. Review—Recent Advances and Remaining Challenges for Lithium Ion Battery Cathodes I. Nickel-Rich, $LiNi_xCo_yMn_zO_2$, *J. Electrochem. Soc.* **2017**, *164*, A6220-A6228.

(95) Myung, S.-T.; Maglia, F.; Park, K.-J.; Yoon, C. S.; Lamp, P.; Kim, S.-J.; Sun, Y.-K. Nickel-Rich Layered Cathode Materials for Automotive Lithium-Ion Batteries: Achievements and Perspectives, *ACS Energy Lett.* **2017**, *2*, 196-223.

(96) Sun, H.-H.; Manthiram, A. Impact of Microcrack Generation and Surface Degradation on a Nickel-Rich Layered $Li[Ni_{0.9}Co_{0.05}Mn_{0.05}]O_2$ Cathode for Lithium-Ion Batteries, *Chem. Mater.* **2017**, *29*, 8486-8493.

(97) Hwang, S.; Kim, S. M.; Bak, S.-M.; Chung, K.; Chang, Y. W. Investigating the Reversibility of Structural Modifications of $Li_xNi_yMn_zCo_{1-y-z}O_2$ Cathode Materials during Initial Charge/Discharge, at Multiple Length Scales, *Chem. Mater.* **2015**, *27*, 6044-6052.

(98) Jo, C.-H.; Cho, D.-H.; Noh, H.-J.; Yashiro, H.; Sun, Y.-K.; Myung, S. T. An Effective Method to Reduce Residual Lithium Compounds on Ni-rich $Li[Ni_{0.6}Co_{0.2}Mn_{0.2}]O_2$ Active Material Using a Phosphoric Acid Derived Li_3PO_4 Nanolayer, *Nano Res.* **2015**, *8*, 1464-1479.

(99) Fu, C.; Li, G.; Luo, D.; Li, Q.; Fan, J.; Li, L. Nickel-Rich Layered Microspheres Cathodes: Lithium/Nickel Disordering and Electrochemical Performance, *ACS Appl. Mater. Interfaces* **2014**, *6*, 15822-15831.

(100) Noh, H.-J.; Youn, S.; Yoon, C. S.; Sun, Y.-K. Comparison of the Structural and Electrochemical Properties of Layered $Li[Ni_xCo_yMn_z]O_2$ (x = 1/3, 0.5, 0.6, 0.7, 0.8 and 0.85) Cathode Material for Lithium-Ion Batteries, *J. Power Sources* **2013**, *233*, 121-130.

(101) Sun, H.-H.; Choi, W.; Lee, J. K.; Oh, I.-H.; Jung, H.-G. Control of Electrochemical Properties of Nickel-Rich Layered Cathode Materials for Lithium Ion Batteries by Variation of the Manganese to Cobalt Ratio, *J. Power Sources* **2015**, *275*, 877-883.

(102) Bak, S.-M.; Hu, E.; Zhou, Y.; Yu, X.; Senanayake, S. D.; Cho, S.-J.; Kim, K.-B.; Chung, K. Y.; Yang, X.-Q.; Nam, K.-W. Structural Changes and Thermal Stability of Charged $LiNi_xMn_yCo_zO_2$ Cathode Materials Studied by Combined in Situ Time-Resolved XRD and Mass Spectroscopy, *ACS Appl. Mater. Interfaces* **2014**, *6*, 22594-22601.

(103) Lee, S. J.; Han, J.-G.; Lee, Y.; Jeong, M.-H.; Shin, W. C.; Ue, M.; Choi, N.-S. A Bi-Functional Lithium Difluoro(oxalato)borate Additive for Lithium Cobalt Oxide/Lithium Nickel Manganese Cobalt Oxide Cathodes and Silicon/Graphite Anodes in Lithium-Ion Batteries at Elevated Temperatures, *Electrochim. Acta* **2014**, *137*, 1-8.

(104) Khasanov, M.; Pazhetnov, E.; Shin, W. C. Dicarboxylate-Substituted Ethylene Carbonate as an SEI-Forming Additive for Lithium-Ion Batteries, *J. Electrochem. Soc.* **2015**, *162*, A1892-A1898.

(105) Yim, T.; Kang, K. S.; Mun, J.; Lim, S. H.; Woo, S.-G.; Kim, K. J.; Park, M.-S.; Song, J. H.; Han, Y.-K.; Yu, J.-S.; Kim, Y.-J. Understanding the Effects of a Multi-Functionalized Additive on the Cathode–Electrolyte Interfacial Stability of Ni-Rich Materials, *J. Power Sources* **2016**, *302*, 431-438.

(106) Nurpeissova, A.; Park, D.-I.; Kim, S.-S.; Sun, Y.-K. Epicyanohydrin as an Interface Stabilizer Agent for Cathodes of Li-Ion Batteries, *J. Electrochem. Soc.* **2016**, *163*, A171-A177.

(107) Dong, P.; Wang, D.; Yao, Y.; Li, X.; Zhang, Y.; Ru, J.; Ren, T. Stabilizing Interface Layer of $LiNi_{0.5}Co_{0.2}Mn_{0.3}O_2$ Cathode Materials Under High Voltage Using p-Toluenesulfonyl Isocyanate as Film Forming Additive, *J. Power Sources* **2017**, *344*, 111-118.

(108) Yan, G.; Li, X.; Wang, Z.; Guo, H.; Wang, J.; Peng, W.; Hu, Q. Effects of 1-Propylphosphonic Acid Cyclic Anhydride as an Electrolyte Additive on the High Voltage Cycling Performance of Graphite/$LiNi_{0.5}Co_{0.2}Mn_{0.3}O_2$ Battery, *Electrochim. Acta* **2015**, *166*, 190-196.

(109) Im, J.; Lee, J.; Ryou, M.-H.; Lee, Y. M.; Cho, K. Y. Fluorinated Carbonate-Based Electrolyte for High-Voltage $Li(Ni_{0.5}Mn_{0.3}Co_{0.2})O_2$/Graphite Lithium-Ion Battery, *J. Electrochem. Soc.* **2017**, *164*, A6381-A6385.

(110) Xiong, X.; Wang, Z.; Yue, P.; Guo, H.; Wu, F.; Wang, J.; Li, X. Washing Effects on Electrochemical Performance and Storage Characteristics of $LiNi_{0.8}Co_{0.1}Mn_{0.1}O_2$ as Cathode Material for Lithium-Ion Batteries, *J. Power Sources* **2013**, *222*, 318-325.

(111) Park, K.; Park, J.-H.; Hong, S.-G.; Choi, B.; Heo, S.; Seo, S.-W.; Min, K.; Park, J.-H. Re-Construction Layer Effect of $LiNi_{0.8}Co_{0.15}Mn_{0.05}O_2$ with Solvent Evaporation Process, *Sci. Rep.* **2017**, *7,* 44557-44566.

(112) Kim, K.; Kim, Y.; Park, S.; Yang, H. J.; Park, S. J.; Shin, K.; Woo, J.-J.; Kim, S.; Hong, S. Y.; Choi, N.-S. Dual-Function Ethyl 4,4,4-Trifluorobutyrate Additive for High-Performance Ni-Rich Cathodes and Stable Graphite Anodes, *J. Power Sources*, **2018**, *396*, 276-287.

(113) Watanabe, S.; Kinoshita, M.; Hosokawa, T.; Morigaki, K.; Nakura, K. Capacity Fade of $LiAl_yNi_{1-x-y}Co_xO_2$ Cathode for Lithium-Ion Batteries During Accelerated Calendar and Cycle Life Tests (Surface Analysis of $LiAl_yNi_{1-x-y}Co_xO_2$ Cathode After Cycle Tests in Restricted Depth of Discharge Ranges), *J. Power Sources* **2014**, *258*, 210-217.

(114) Storey, R. F.; Hoffman, D. C. Formation of Poly(Ethy1ene Ether Carbonate) Diols: Proposed Mechanism and Kinetic Analysis, *Macromolecules* **1992**, *25*, 5369-5382.

(115) Sarel, S.; Levin, I.; Pohoryles, L. A. 614. Organic carbonates. Part V. The Mechanism of Hydrolysis of Cyclic Carbonates: Tracer Studies, *J. Chem. Soc*. **1960**, 3079-3082.

(116) Jones, L. B.; Sloane, T. B. Nucleophilic Reactivity at Unsaturated Centers: I. Methanolysis of Substituted Methyl Benzoates, *Tetrahedron Lett.* **1966**, *8*, 831-837.

(117) Hofman, A.; Stomkowski, S.; Penczek, S. Structure of Active Centers and Mechanism of the Anionic Polymerization of Lactones, *Makromol. Chem.* **1984**, *185*, 91-101.

(118) Webster, R. D.; Bond, A. M.; Electrochemical Reduction of Pyridine- and Benzene-Substituted n-Alkyl Esters and Thioic S-Esters in Acetonitrile, *J. Org. Chem.* **1997**, *62*, 1779-1787.

(119) Kiminkinen, L. K. M.; Zeller, L. C.; Kenttämaa, H. I. The Structure of the Long-Lived Radical Cation of Ethyl Acetate, *J. Chem. Soc. Chem. Commun.* **1992**, *6*, 466-468.

(120) Leeck, D. T.; Stirk, K. M.; Zeller, L. C.; Kiminkinen, L. K. M.; Castro, L. M.; Vainiotalo, P.; Kenttämaa, H. I. The Long-Lived Radical Cations of Simple Carbon Esters Isomerize to the Lowest-Energy Structure, *J. Am. Chem. Soc.* **1994**, *116*, 3028-3038.

(121) Kim, J.; Lee, H.; Cha, H.; Yoon, M.; Park, M.; Cho, J. Prospect and Reality of Ni-Rich Cathode for Commercialization, *Adv. Energy Mater.* **2018**, *8,* 1702028.

(122) Aykol, M.; Kim, S.; Hegde, V. I.; Snydacker, D.; Lu, Z.; Hao, S.; Kirklin, S.; Morgan, D.; Wolverton, C. High-throughput computational design of cathode coatings for Li-ion batteries, *Nat. Commun.* **2016**, *7,* 13779.

(123) Kim, J.; Lee, J.; Ma, H.; Jeong, H. Y.; Cha, H.; Lee, H.; Yoo, Y.; Park, M.; Cho, J. Controllable Solid Electrolyte Interphase in Nickel-Rich Cathodes by an Electrochemical Rearrangement for Stable Lithium-Ion Batteries, *Adv. Mater*. **2018**, *30*, 1704309.

(124) Edström, K.; Gustafsson, T.; Thomas, J. O. The Cathode-Electrolyte Interface in the Li-Ion Battery, *Electrochim. Acta*, **2004**, *50*, 397-403.

(125) Beltrop, K.; Klein, S.; Nölle, R.; Wilken, A.; Lee, J. J.; Köster, T. K.-J.; Reiter, J.; Tao, L.; Liang, C.; Winter, M.; Qi, X.; Placke, T. Triphenylphosphine Oxide as Highly Effective Electrolyte Additive for Graphite/NMC811 Lithium Ion Cells, *Chem. Mater*. **2018**, *30*, 2726-2741.

(126) Yim, T.; Kang, K. S.; Mun, J. S.; Lim, H.; Woo, S.-G.; Kim, K. J.; Park, M.-S.; Cho, W.; Song, J. H.; Han, Y.-K.; Yu, J.-S.; Kim, Y.-J. Understanding the Effects of a Multi-Functionalized Additive on the Cathode–Electrolyte Interfacial Stability of Ni-Rich Materials, *J. Power Sources*, **2016**, *302*, 431-438.

(127) Xu, K. Nonaqueous Liquid Electrolytes for Lithium-Based Rechargeable Batteries, *Chem. Rev*. **2004**, *104*, 4303-4418.

(128) Berhaut, C. L.; Lemordant, D.; Porion, P.; Timperman, L.; Schmidt, G.; Anouti, M. Ionic Association Analysis of LiTDI, LiFSI and $LiPF_6$ in EC/DMC for Better Li-Ion Battery performances, *RSC Adv*. **2019**, *9*, 4599-4608.

(129) Yang, H.; Zhuang, G. V.; Ross Jr. P.N. Thermal Stability of $LiPF_6$ Salt and Li-Ion Battery Electrolytes Containing $LiPF_6$, *J. Power Sources*, **2006**, *161*, 573-579.

(130) Campion, C. L.; Li, W.; Lucht, B. L. Thermal Decomposition of $LiPF_6$-Based Electrolytes for Lithium-Ion Batteries, *J. Electrochem. Soc*. **2005**, *152*, A2327-A2334.

(131) Plakhotnyk, A. V.; Ernst, L.; Schmutzler, R. Hydrolysis in the System $LiPF_6$-Propylene Carbonate-Dimethyl Carbonate-H_2O, *J. Fluorine Chem*. **2005**, *126*, 27-31.

(132) Kanamura, K.; Taruma, H.; Takehara, Z.-i. XPS Analysis of a Lithium Surface Immersed in Propylene Carbonate Solution Containing Various Salts, *J. Electroanal. Chem*. **1992**, *333*, 127-142.

(133) Kim, J.; Lee, J. G.; Kim, H.-S.; Lee, T. J.; Park, H.; Ryu, J. H.; Oh, S. M. Thermal Degradation of Solid Electrolyte Interphase (SEI) Layers by Phosphorus Pentafluoride (PF_5) Attack, *J. Electrochem. Soc*. **2017**, *164*, A2418-A2425.

(134) Lee, H. H.; Wan, C. C.; Wang, Y. Y. Thermal Stability of the Solid Electrolyte Interface on Carbon Electrodes of Lithium Batteries, *J. Electrochem. Soc*. **2004**, *151*, A542-A547.

(135) Sloop, S. E.; Kerr, J. B.; Kinoshita, K. The Role of Li-Ion Battery Electrolyte Reactivity in Performance Decline and Self-Discharge, *J. Power Sources*, **2003**, *119-121*, 330-337.

(136) Zhao, H.; Yu, X.; Li, J.; Li, B.; Shao, H.; Li, L.; Deng, Y. Film-Forming Electrolyte Additives for Rechargeable Lithium-Ion Batteries: Progress and Outlook, *J. Mater. Chem. A*, **2019**, *7*, 8700-8722.

(137) Vetter, J.; Novák, P.; Wagner, M. R.; Veit, C.; Möller, K.-C.; Besenhard, J. O.; Winter, M.; Wohlfahrt-Mehrens, M.; Vogler, C.; Hammouche, A. Ageing Mechanisms in Lithium-Ion Batteries, *J. Power Sources*, **2005**, *147*, 269-281.

(138) Lee, T. J.; Soon, J.; Chae, S.; Ryu, J. H.; Oh, S. M. A Bifunctional Electrolyte Additive for High-Voltage $LiNi_{0.5}Mn_{1.5}O_4$ Positive Electrodes, *ACS Appl. Mater. Interfaces*, **2019**, *11*, 11306-11316.

(139) Lyu, H.; Li, Y.; Jafta, C. J.; Bridges, C. A.; Meyer III, H. M.; Borisevich, A.; Parathaman, M. P.; Dai, S.; Sun, X.-G. Bis(trimethylsilyl) 2-Fluoromalonate Derivatives as Electrolyte Additives for High Voltage Lithium Ion Batteries, *J. Power Sources*, **2019**, *412*, 527-535.

(140) Kim, C.-K.; Shin, D.-S.; Kim, K.-E.; Shin, K.; Woo, J.-J.; Kim, S.; Hong, S. Y.; Choi, N.-S. Fluorinated Hyperbranched Cyclotriphosphazene Simultaneously Enhances the Safety and Electrochemical Performance of High-Voltage Lithium-Ion Batteries, *ChemElectroChem*, **2016**, *3*, 913-921.

(141) Liao, B.; Li, H.; Wang, X.; Xu, M.; Xing, L.; Liao, Y.; Liu, X.; Li, W. Significantly Improved Cyclability of Lithium Manganese Oxide, Simultaneously Inhibiting Electrochemical and Thermal Decomposition of the Electrolyte by the Use of an Additive, *RSC Adv*. **2017**, *7,* 46594-46603.

(142) Liao, B.; Hu, X.; Xu, M.; Li, H.; Yu, L.; Fan, W.; Xing, L.; Liao, Y.; Li, W. Constructing Unique Cathode Interface by Manipulating Functional Groups of Electrolyte Additive for Graphite/$LiNi_{0.6}Co_{0.2}Mn_{0.2}O_2$ Cells at High Voltage, *J.Phys. Chem. Lett.* **2018**, *9*, 3434-3445.

(143) Zhang, S.S. A Review on Electrolyte Additives for Lithium-Ion Batteries, *J. Power Sources*, **2006**, *162*, 1379-1394.

(144) Zhou, R.; Huang, J.; Lai, S.; Li, J.; Wang, F.; Chen, Z.; Lin, W.; Li, C.; Wang, J.; Zhao, A Bifunctional Electrolyte Additive for H_2O/HF Scavenging and Enhanced

Graphite/$LiNi_{0.5}Co_{0.2}Mn_{0.3}O_2$ Cell Performance at a High Voltage, J. *Sustainable Energy Fuels*, **2018**, *2*, 1481-1490.

(145) Barlow, C. G. Reaction of Water with Hexafluorophosphates and with Li Bis(perfluoroethylsulfonyl) imide Salt, *Electrochem. Solid-State Lett*. **1999**, *2*, 362-364.

(146) Wiemers-Meyer, S.; Winter, M.; Nowak, S. Mechanistic Insights into Lithium Ion Battery Electrolyte Degradation - a Quantitative NMR Study, *Phys. Chem. Chem. Phys.* **2016**, *18*, 26595-26601.

(147) Domi, Y.; Doi, T.; Tsubouchi, S.; Yamanaka, T.; Abe, T.; Ogumi, Z. Irreversible Morphological Changes of a Graphite Negative-Electrode at High Potentials in $LiPF_6$-Based Electrolyte Solution, *Phys. Chem. Chem. Phys.* **2016**, *18*, 22426-22433.

(148) Aurbach, D.; Markovsky, B.; Shechter, A.; Ein-Eli, Y. A Comparative Study of Synthetic Graphite and Li Electrodes in Electrolyte Solutions Based on Ethylene Carbonate-Dimethyl Carbonate Mixtures, *J. Electrochem. Soc.* **1996**, *143*, 3809-3820.

(149) Parimalam, B. S.; Lucht, B. L. Reduction Reactions of Electrolyte Salts for Lithium Ion Batteries: $LiPF_6$, $LiBF_4$, LiDFOB, LiBOB, and LiTFSI, *J. Electrochem. Soc.* **2018**, *165*, A251-A255.

(150) Ouatani, L. E.; Dedryvère, R.; Siret, C.; Biensan, P.; Gonbeau, D. Effect of Vinylene Carbonate Additive in Li-Ion Batteries: Comparison of $LiCoO_2$/C, $LiFePO_4$/C, and $LiCoO_2$/$Li_4Ti_5O_{12}$ Systems, *J. Electrochem. Soc.* **2009**, *156,* A468-A477.

(151) Pritzl, D.; Solchenbach, S.; Wetjen, M.; Gasteiger, H. A. Analysis of Vinylene Carbonate (VC) as Additive in Graphite/$LiNi_{0.5}Mn_{1.5}O_4$ Cells, *J. Electrochem. Soc.* **2017**, *164*, A2625-A2635.

(152) Li, W.; Dolocan, A.; Oh, P.; Celio, H.; Park, S.; Cho, J.; Manthiram, A. Dynamic Behaviour of Interphases and Its Implication on High-Energy-Density Cathode Materials in Lithium-Ion Batteries, *Nat. Commun.* **2017**, *8,* 14589.

(153) Li, W.; Kim, U.-H.; Dolocan, A.; Sun, Y.-K.; Manthiram, A. Formation and Inhibition of Metallic Lithium Microstructures in Lithium Batteries Driven by Chemical Crossover, *ACS Nano*, **2017**, *11*, 5853-5863.

(154) Li, J.; Li, W.; You, Y.; Manthiram, A. Extending the Service Life of High-Ni Layered Oxides by Tuning the Electrode–Electrolyte Interphase, *Adv. Energy Mater*. **2018**, *8*, 1801957.

(155) Abraham, D. P.; Twesten, R. D.; Balasubramanian, M.; Kropf, J.; Fischer, D.; McBreen, J.; Petrov, I.; Amine, K. Microscopy and Spectroscopy of Lithium Nickel Oxide-Based Particles Used in High Power Lithium-Ion Cells, *J. Electrochem. Soc.* **2003,** *150,* A1450-A1456.

(156) Koyama, Y.; Mizoguchi, T.; Ikeno, H.; Tanaka, I. Electronic Structure of Lithium Nickel Oxides by Electron Energy Loss Spectroscopy, *J. Phys. Chem. B,* **2005**, *109,* 10749-10755.

(157) Lin, F.; Markus, I. M.; Nordlund, D.; Weng, T.-C.; Asta, M. D.; Xin, H. L.; Doeff, M. M. Surface Reconstruction and Chemical Evolution of Stoichiometric Layered Cathode Materials for Lithium-Ion Batteries, *Nat. Commun.* **2014**, *5,* 3529.

(158) Hwang, S.; Chang, W.; Kim, S. M.; Su, D.; Kim, D. H.; Lee, J. Y.; Chung, K. Y.; Stach, E. A. Investigation of Changes in the Surface Structure of $Li_xNi_{0.8}Co_{0.15}Al_{0.05}O_2$ Cathode Materials Induced by the Initial Charge, *Chem. Mater.* **2014**, *26,* 1084-1092.

Acknowledgements

저의 석박통합과정이 잘 마무리될 수 있었던 것은 많은 분들의 도움이 있었기 때문이며, 이 글을 통해 감사의 인사를 드리고자 합니다.

먼저 지도교수님이신 최남순 교수님께 크게 감사드립니다. 학부생 시절 교수님의 탁월하고 꼼꼼하신 강의에 감동하게 되어 연구실에 지원을 하게 된 것이 엊그제 같은데 박사학위를 받고 졸업을 하게 되었습니다. 누구보다도 열정적이신 교수님 덕택에 연구실에서 보낸 지난 6 년은 많이 배우고 성장할 수 있는 시간이었습니다. 바쁘신 와중에도 항성 아낌없는 조언과 지도를 해주시는 교수님의 헌신적인 마음에 깊이 감사드립니다. 또한, 학위 논문 심사 과정 중 아낌없는 조언을 주신 정경민 교수님, 송현곤 교수님, 홍성유 교수님, 강석주 교수님께 감사의 말씀을 드립니다.

그리고 모든 CNS 연구실 동료 분들께 큰 감사의 말씀을 전합니다. 제가 처음 연구실에 들어왔을 때, 기본적인 실험 노하우를 전수해주었던 송영민, 김준기 및 이성준 선배님들께 감사드리며, 더 좋은 연구 결과가 도출될 수 있도록 함께 고민해 준 최초의 연구실 박사 졸업생인 이용원, 한정구 박사님들께도 감사의 말씀을 전합니다. 또한 저와 함께 다양한 연구를 진행했던 연경, 성지, 주연, 명선, 세훈, 원준, 가영, 현규에게도 고마움을 전합니다.

마지막으로, 언제나 앞으로도 항상 저에게 아낌없는 용기를 북돋아 주신 부모님 과 동생에게도 깊은 감사의 말씀을 드리며 더 좋은 딸과 누나가 될 것을 약속드립니다. 미처 언급하지 못했지만, 제 연구에 도움을 주신 연구원 선생님들께도 진심으로 감사하다는 말씀을 드리며 이만 줄이도록 하겠습니다.